Appendix A.

Radar Background: Resolution, Target Reflectivity, Attenuation and Multipath

A.1. Resolution

A.1.1. Angular Resolution

A radar antenna is a device that transforms the distribution of electromagnetic energy across its aperture into a spatial distribution of energy to points far removed (the far field). This spatial distribution of energy when plotted on a relative basis is called the antenna radiation pattern and is a measure of the power per unit area (power pattern) in a given direction [174]. It is this pattern that determines the angular resolution of an imaging radar.

As most antennas are either rotationally or bilaterally symmetrical, 2-D plots are generally sufficient and more convenient to measure and plot [176]. For example, cuts can be taken through the 3-D antenna pattern shown in Figure.2.1 to produce elevation and azimuth patterns. If the cuts pass through the peak of the beam they are referred to as principal-plane patterns, and examples of these are shown in Figure A.1.

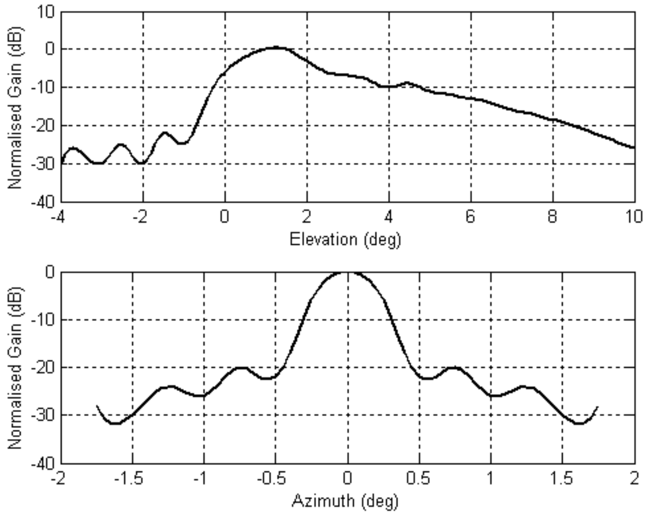

Figure A.1: Principal plane (a) elevation and (b) azimuth patterns of a cosec^2 fan-beam antenna

The most common method of plotting a 2-D pattern is to use rectangular coordinates with the vertical axis in decibels. This provides a wide dynamic range of pattern levels with good visibility of the details. However, other forms of plotting pattern data are also used.

- Polar plot of relative voltage intensity
- Rectangular plot of voltage
- Rectangular plot of relative power
- Rectangular plot of relative power (in decibels)

One of the main features of an antenna pattern is the beamwidth of the main lobe. As it is a continuous function that varies from the peak to the minima, the width is generally measured at the half-power, 3dB points. Though other beamwidths are sometimes specified, for example, the 10dB, one-tenth power width or the width between nulls, in general the 3dB beamwidth is used because it is the standard used to define the angular resolution of the antenna.

The resolution of an antenna is defined as the angular separation between two point targets of equal cross-section at the same range that can be resolved as separate targets.

The angular resolution of a circular aperture is determined from its size (aperture), in wavelengths and the illumination function. Because of the limited aperture, the image of a point target appears not as a single point, but as a diffraction pattern consisting of a central bright spot which corresponds to the main lobe surrounded by concentric rings of bright and dark lines that make up the sidelobes. An example of the effect of changing the antenna aperture on the resolution is illustrated in Figure A.2.

Figure A.2: Effects of the size of the aperture on the resolution of an antenna showing (a) the aperture unable to resolve the targets, (b) just large enough to satisfy the resolution criteria and (c) increased resolution obtained by increasing the aperture still further [172]

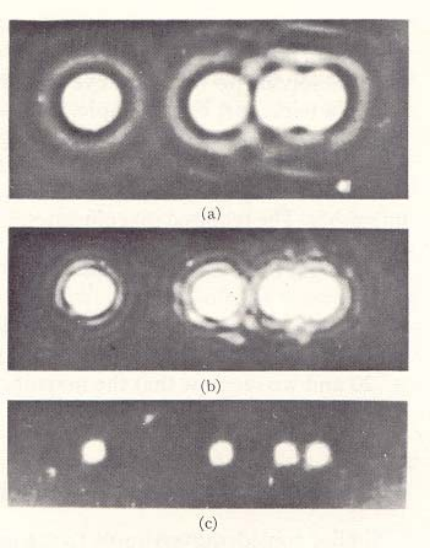

In radar parlance, the dark and light rings that surround each of the lights are referred to as sidelobes. Sidelobe levels are generally defined in terms of their amplitude with respect to the main lobe.

In general it is not possible to produce sidelobe levels that are 50dB down to eliminate all ghosting, but with careful design it is possible to obtain levels that are 35dB down at X-band and at least 20dB down at W-band. These are sufficiently low to eliminate all but the brightest specular reflections produced by man-made targets.

To produce an antenna pattern with low sidelobes it is necessary to taper the aperture illumination function and in so doing, to under-illuminate the aperture. The price paid for lower sidelobe levels is an increased main-lobe width with the associated degradation in angular resolution and a slightly lower efficiency.

Figure A.3 shows the effect of tapering the aperture illumination on the beam pattern produced by a line source.

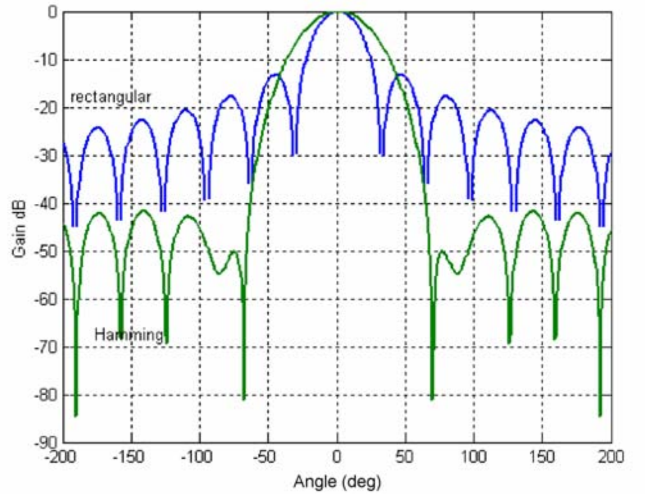

Figure A.3: Effect of the aperture distribution function on both angular resolution and sidelobe levels for a line source

Uniform amplitude distribution of a rectangular or linear aperture results in -13.2dB sidelobes. However, if the uniform distribution is replaced by the Hamming illumination (0.54+0.46cos(θ)), the result is a theoretical reduction of the sidelobe levels to -42dB and an increase in the main-lobe width by a factor of 1.33 [105].

One further important characteristic of an antenna is the gain. In an ideal case the gain is just the ratio of the maximum power density to the power density of an isotropic radiator with the same input power. This is related to the antenna aperture, and the aperture efficiency by

$$G = \frac{4\pi\eta_a A}{\lambda^2}, \tag{A.1}$$

where G is the antenna gain, η_a the aperture efficiency, A the antenna aperture (m^2) and λ the wavelength (m).

An approximate relationship can be derived that links the gain and the antenna beam widths of an antenna

$$G = \frac{4\pi}{\theta_{az}\theta_{el}}, \tag{A.2}$$

where θ_{az} and θ_{el} are the azimuth and elevation 3dB beamwidths (rad) respectively.

For the robotics applications undertaken at the ACFR, one of the more common antennas in use is a 150mm diameter horn-lens manufactured by Flann Microwave shown in Figure A.4 along with a similar antenna made by Philips Microwave. If the standard assumptions are made regarding the illumination function and the efficiency, of the Flann unit, then the calculated beamwidth at 94GHz will be 1.5° and the gain will be 42dB both of which are within a few percent of the measured values. Because of internal reflection effects, the sidelobe levels of horn-lens is seldom below -20dB, but these are not quoted by the manufacturer and have not been measured. More information on the mechanism that determines the sidelobe levels for horn-lens antennas can be found in Section C.4.

Figure A.4: Horn-lens antennas that are commonly used in radar applications at the ACFR because they exhibit good electrical characteristics as well as being extremely robust

A.1.2. Relation between Range Resolution and Spectral Content

It can be shown using Fourier theory that a single burst of microwave energy at a frequency contained within a rectangular envelope, with a duration τ, produces a spectrum with a main lobe that extends from f_o-1/τ to f_o+1/τ and harmonics which extend further as shown in Figure A.5.

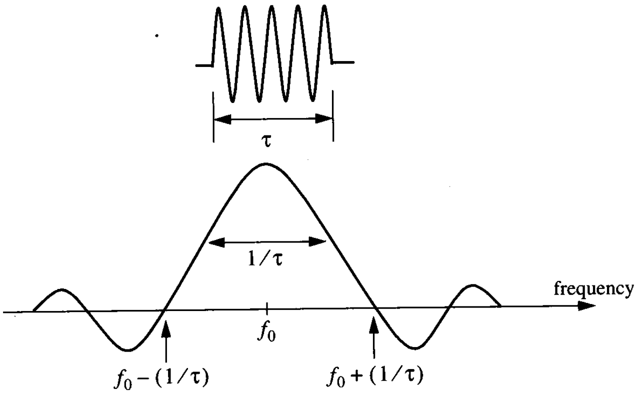

Figure A.5: Relationship between the spectral characteristics of a radar pulse and its duration

In an ideal noise free system, the receiver bandwidth could be wide enough to include the main lobe and many of the harmonics without losing any information, but in a real system that includes thermal noise, a bandwidth β exists that maximises the received signal to noise ratio (SNR). As a rule of thumb, the optimum "matched" bandwidth is equal to $1/\tau$.

It can be seen from the spectrum in Figure A.5 that if the bandwidth is increased beyond the optimum, the amount of additional energy received diminishes rapidly, but because the received noise-power spectrum (not illustrated) is flat, the proportion of noise received increases with a resulting decrease in the SNR. If, on the other hand, the bandwidth is decreased below the optimum, then the response time of the filter is too slow to accommodate the pulse rise and fall time, and the filter "rings".

A.1.3. Range Gating

The concept of range gating was developed initially for a tracking radar in which only the point target echo return was required, and so techniques were developed to sample the received analogue signal at the correct time using a fast electronic switch to gate out this signal. An extension of this concept to encompass imaging applications is to develop a series of switches or gates staggered in time by the range resolution of the radar to capture a sequence of echoes with every transmitted pulse. In a digital system, this sampled data are then digitised by an ADC and stored prior to further processing as is shown in Figure A.6.

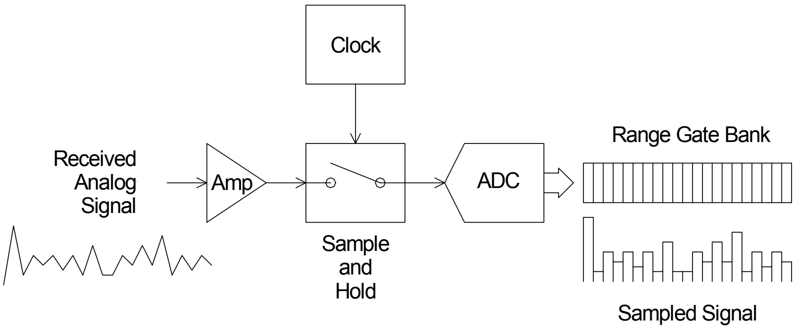

Figure A.6: Schematic diagram illustrating the range gating concept as a sequence of digitised samples stored in computer memory

In this example, the amplitude of the echo signal is recorded as a function of time/range so that a more realistic image that includes the magnitude of the target reflectivity can be produced.

Other radar modulations, FMCW for example, do not generate their range gates directly from the time-sampled analog echo signal but via a transform from the frequency domain. However, this notwithstanding, the content of each gate remains the vector sum of the magnitudes of all the reflections within a specific area defined by the antenna angular resolution and the range gate extent.

A.2. Reflectivity

A.2.1. Target Cross-Section and Reflectivity

When a radar pulse is radiated into space it will propagate at the speed of light with most of the power constrained within a cone defined by the antenna beam pattern. If the beam intersects with an object with a relative dielectric constant, $\varepsilon_r > 1$, then some of the power will be scattered back towards the radar where it can be detected.

This section considers the interactions between the radar signal and such objects in an attempt to determine the factors that affect the probability that the object will be detected and the probability that noise alone will be mistaken for a target.

The "cross section" qualitatively relates the amount of power that strikes the target, S_i (w/m^2), to the amount of power that is reflected into the receiver, S_r (W/m^2),

$$\sigma = \lim_{R\to\infty} 4\pi R^2 \left|\frac{S_r}{S_i}\right|. \tag{A.3}$$

For imaging applications, this analysis must be extended to include targets whose area is larger than the beam footprint which makes an alternative description necessary. This alternative description defines the radar cross-section per unit area as the target reflectivity σ^o. The RCS is then calculated by scaling the reflectivity by the appropriate illuminated area, A.

The average magnitude of the signal reflected from the surface of the earth is a function of the material, surface roughness and angle. The most convenient method of modelling this reflectivity is the constant γ model in which the surface reflectivity is modelled as a function of the grazing angle

$$\sigma^o = \gamma \sin\psi . \tag{A.4}$$

At low grazing angles the measurements fall below the model because of propagation-factor effects, and at high grazing angles the measurements rise above it because of quasi-specular reflections from surface facets. Values for γ between –10 and –15dB are widely applicable to land covered by crops, bushes and trees, while desert, grassland and marsh are more likely to have γ near –20dB, and finally, urban or mountainous regions will have γ near –5dB as shown in Figure A.7. These values are almost independent of wavelength and polarisation, but they only apply to modelling of the mean clutter reflectivity.

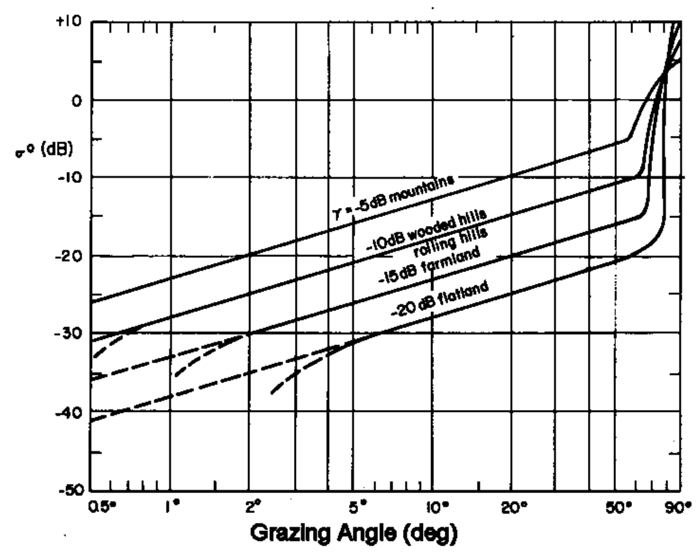

Figure A.7: Effect of grazing angle on clutter reflectivity for different types of terrain

Measurements made at 94GHz [66] shown in Figure A.8 confirm the basic trend is shown, but predict a higher reflectivity for both grass and crops as well as forest.

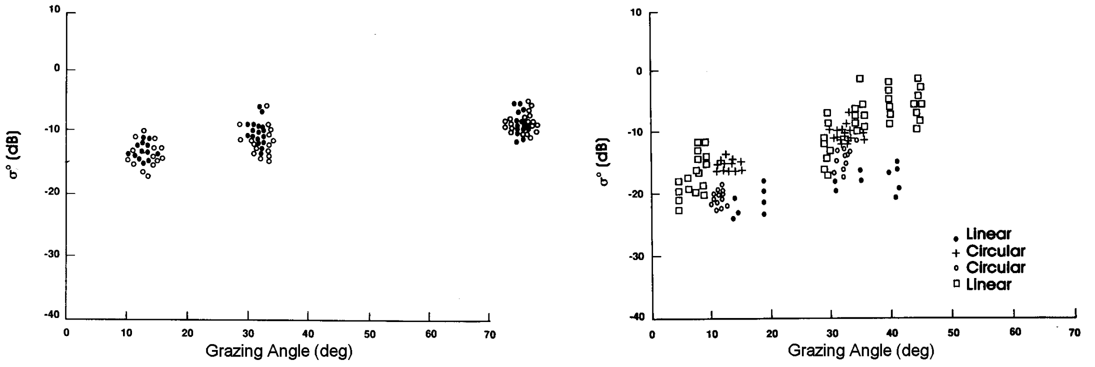

(a) (b)

Figure A.8: Measured ground reflectivity at 95GHz of (a) grass and crops and (b) deciduous trees

In many robotic applications, the radar is mounted on an AGV, and so most of the environment is being observed broadside on, or even from below in some cases. In addition, man-made structures such as buildings, poles and other vehicles are often present which further complicate the issue. Under these circumstances only the grass or road surfaces in the immediate vicinity of the radar fall within the model assumptions defined above. A typical example of a set of observations made by a radar system that cannot be interpreted using the standard model is shown in Figure A.9 and Figure A.10.

(a) (b)

Figure A.9: Comparison of an (a) aerial photograph and (b) beamwidth-limited millimetre-wave radar image of the region surrounding the ACFR. Note that some of the trees present in the aerial photograph had been removed by the time that the radar image was made

In this example, a 3-D scanning radar developed at the ACFR [169] was placed in the centre of a grass quadrangle surrounded by buildings, grass and trees. The image was produced by scanning the radar through 360° in azimuth and then stepping the beam up by a few tenths of a degree in elevation, and repeating the process. With each measurement, only the largest target that exceeded the detection threshold was logged in an incredibly inefficient method of image production.

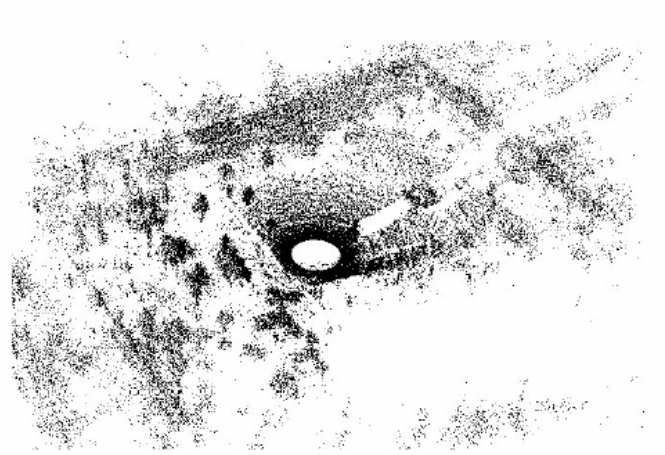

Figure A.10: A 3-D perspective view of the region surrounding the ACFR made using a high-resolution beamwidth-limited millimetre-wave radar

As the radar only stands some 1.5m above the ground, and the unit was producing images of nearby trees that stand 5m tall and of buildings even higher than this, it is clear that the standard methods of characterising target reflectivity in terms of grazing angle are inadequate and will have to be addressed by either extending the existing models, by developing a new model or by measurement of a broad range of natural and man-made structures from the appropriate perspective.

A.2.2. Measuring Reflectivity

The accurate measurement of surface reflectivity is fraught with difficulty. To begin with, two possible geometries must be considered when calculating the measurement area, depending on whether the whole ground echo falls within one range cell or not as determined by the inequality expressed in Figure A.11 [66].

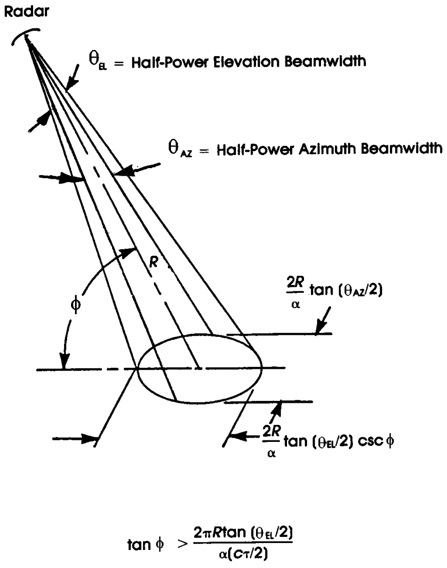

Figure A.11: Definition of a beamwidth-limited resolution cell

In the beamwidth-limited example, it can be seen that the illuminated area is defined by the intersection of the conical beam with the surface of the target. Due to the geometry and the length of the transmitted pulse, it is assumed that all of the power reflected from this surface contributes to the RCS of the target and so the area can be approximated by an elliptical footprint

$$A = \pi r_1 r_2, \tag{A.5a}$$

$$A = \left(\frac{\pi R^2}{\alpha^2}\right)\left(\tan\frac{\theta_{AZ}}{2}\right)\left(\tan\frac{\theta_{EL}}{2}\right)\csc\phi, \tag{A.5b}$$

where A – Area illuminated on the surface (m^2)
R – Slant range to the surface (m)
α – Beam shape factor = 1.33 for a Gaussian shaped beam
θ_{AZ} – Azimuth 3dB two-way beamwidth (rad)
θ_{EL} – Elevation 3dB two-way beamwidth (rad)
ϕ – Grazing angle (rad)

This operational mode can be extended to encompass the measurement of the returns from walls and trees if the appropriate geometry is applied, and the tree surface is assumed to be impenetrable by the radar signal.

One alternative is to gate the radar signal in range, but once again, this is not satisfactory unless a well-defined surface is being measured as shown in Figure A.12.

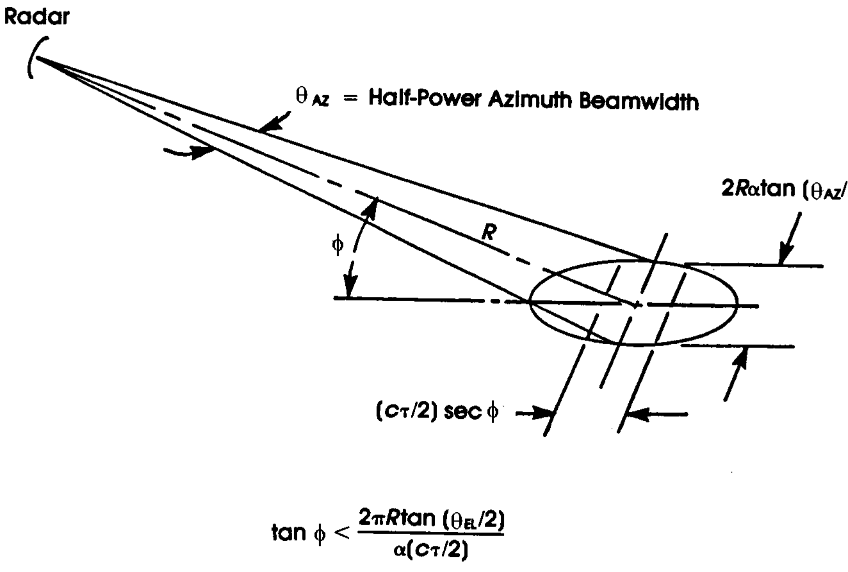

Figure A.12: Definition of a pulse-width (range-gate) limited resolution cell

If the projected pulse width is sufficiently short compared to the length of the elliptical footprint defined by the elevation beam width, then the area can be approximated by a rectangle, and the formula for the area

$$A = \frac{Rc\tau}{\alpha}\left(\tan\frac{\theta_{AZ}}{2}\right)\sec\phi\,, \tag{A.6}$$

where c is the speed of light (3×10^8 m/s) and τ the transmitted pulsewidth (sec).

For the measurement of foliage where some penetration occurs, then the volume clutter formulation is appropriate. In this formulation an analogous normalisation parameter to σ^0 called η exists for volume scatterers. This volume reflectivity is defined as the RCS per unit illuminated volume (m^2/m^3).

As with the surface cases, the illuminated volume can be calculated from the geometry shown in Figure A.13 which is just the volume of an elliptical cylinder with diameters $R\theta_{AZ}$ and $R\theta_{EL}$ and with length $c\tau/2$.

$$V = \frac{\pi R^2\theta_{AZ}\theta_{EL}c\tau}{8\alpha^2}\,. \tag{A.7}$$

The radar cross section is then the product of the volume reflectivity η and the volume V

$$\sigma = \eta V\,. \tag{A.8}$$

This model assumes that there is minimal attenuation of the radar signal over the length of the cell. This may be a valid assumption at lower frequencies where foliage penetration is good, but it is not in the millimetre-wave band where the measured two-way attenuation in dry foliage exceeds 4dB/m and is even higher in dense green foliage. In this case a more complex formulation to take this attenuation into account is required

$$\sigma = \eta V \exp(-c\tau\alpha). \tag{A.9}$$

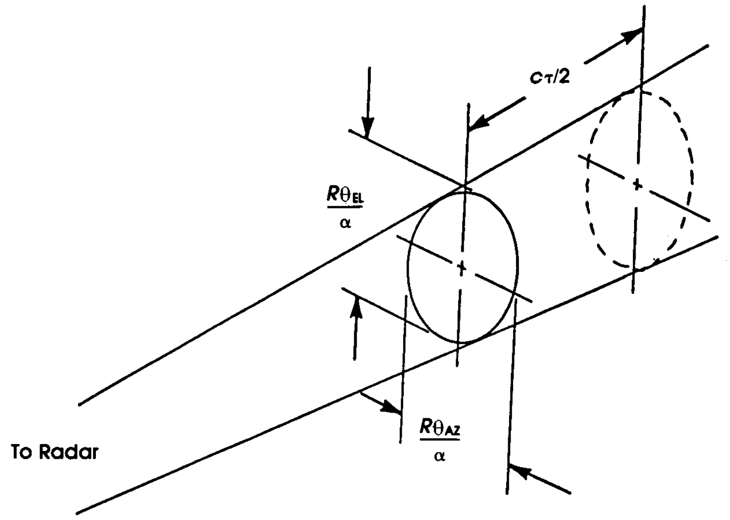

Figure A.13: Definition of a volume-clutter resolution cell

This can be rewritten using the more common dB notation to take advantage of the fact that attenuation is most often given as

$$\sigma_{dB} = 10\log_{10}(\eta V) - c\tau\alpha_{dB}. \tag{A.10}$$

A.2.3. Backscatter

Backscatter generally refers to the scattering of electromagnetic radiation from particles suspended in the atmosphere, which in conjunction with the simultaneous attenuation of the signal, is a major problem in the millimetre-wave band. For autonomous guidance and navigation applications, the most likely source of backscatter is returns from hydrometeors (rain, hail and snow). Figure A.14, summarises the measured data at a number of different frequencies and rainfall rates.

One of the problems with the prediction of backscatter levels is that the Rayleigh model, often used for low-frequency prediction, does not extrapolate well up to the millimetre-wave band where Mie scattering is more applicable [117]. In general, backscatter is not a problem for pencil-beam radar systems operating at short range because the gate volume (defined earlier) is small. It can become a problem for long-range imaging radars with fan-beam antennas because the gate volume becomes much larger, and the ensuing RCS, due to backscatter, that much higher.

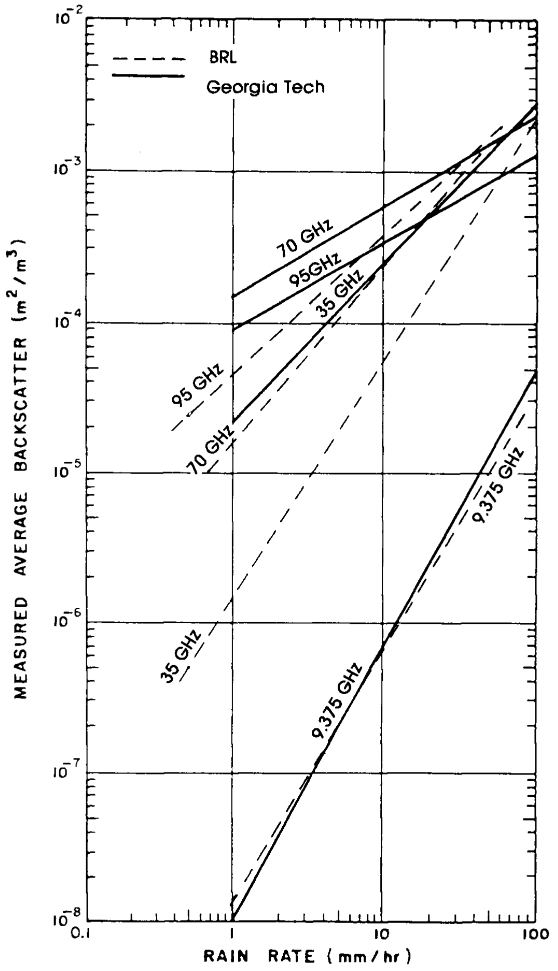

Figure A.14: Measured average backscatter (m^2/m^3) at various frequencies based on BRL and Georgia Tech data as a function of the rainfall rate [67]

A.3. Attenuation

A.3.1. Effect of Rain

The effect of light rain that has a uniform spatial distribution between the radar and the target can be predicted with relative ease. However, heavier rain normally comes in squalls with unpredictable intensity and drop size distribution which makes analysis more difficult and generally rather inaccurate.

Mie (resonance) scattering theory is generally applied for frequencies up to the sub-millimetre-wave band [20]. This results in an empirical relationship between the attenuation, α_r (dB/km), and the rain rate, R (mm/hr),

$$\alpha_r = AR^B, \tag{A.11}$$

with a and b being the empirical coefficients listed in Table A.1 which are functions of the operational frequency and temperature [67] p151.

Table A.1: Rainfall attenuation coefficients at 35 and 94GHz

Coefficient	35GHz	94GHz
A	0.27	1.6
B	0.985	0.64

Assuming typical rainfall conditions with spherical raindrops that obey the Laws-Parsons size distribution [67] p160, then the attenuation with frequency up to 300GHz can be calculated.

At low frequencies where the average drop diameter, a, is much smaller than the wavelength of the radiation, known as the Rayleigh region, the attenuation is proportional to λ^{-4}. As the frequency increases into the Mie region where $2\pi a/\lambda \approx 1$ the attenuation becomes oscillatory until the optical region is reached where the drop diameter is much larger than the wavelength and the attenuation stabilises at a value that is proportional to the liquid water content (LWC) of the air. The attenuation increases with increasing frequency to reach a peak at about 100GHz where resonance effects dominate, before dipping slightly at higher frequencies.

Measurements of frozen hydrometeor characteristics are much less common. Snow data are particularly difficult to quantify because of the broad range of snowflake diameters (between 2 and 15mm) and liquid water content. Some information bay be found in [67] pp160-166.

At IR and visible wavelengths, the drop size is much larger than the wavelength, so the attenuation will be independent of drop diameter [44] and is proportional to water content in g/m^3, and hence proportional to rain rate, R. However, this thesis is only concerned with frequencies up to 94GHz and so details of this interaction will not be discussed further.

A.3.2. Effect of Fog and Clouds

Cloud, fog and mist are defined as the condensation of atmospheric water vapour into water droplets suspended in the air.

Fog is defined as a water droplet density that restricts the visibility on the ground to less than 1km. It can be produced by advection (horizontal movement of a warm air mass over cold water) or by radiation (cooling of the air overnight) which often occurs over rivers and swamps.

When the total attenuation through a cloud or fog bank is required, the liquid water content, M (g/m^3), is first determined by Eldridge's empirical relationship [67] p138 that relates this to the visibility, V (m),

$$M = 308V^{-1.43}. \tag{A.12}$$

Visibility is defined rather loosely as the distance at which large dark objects can be discerned against the horizon by human operators.

Because the drop diameter of both fog and clouds is less than 100µm, the Rayleigh (low frequency) approximation can be used to evaluate the attenuation, α_f (dB/km), at microwave and millimetre-wave frequencies

$$\alpha_f = k\rho_o, \tag{A.13}$$

where k is the attenuation coefficient (dB/km per g/m^3) at a specific frequency and temperature, and ρ_o is the water content (g/m^3).The specific attenuation coefficients at a temperature of 10°C at 35 and 94 GHz, taken from a graph in [20] p166,.are shown in Table A.2.

Table A.2: Specific attenuation coefficients at 35 and 94GHz

Coefficient dB/km per g/m^3	**35GHz**	**94GHz**
k	0.7	4.5

Table A.3 gives an indication of the typical ranges in LWC that can be expected from various fog and cloud types [20] p167.

Table A.3: Range of LWC for clouds and fog

Cloud Type	**Liquid Water Content (g/m^3)**
Heavy Fog	0.15-0.4
Moderate Fog	0.01-0.1
Cumulus	0.5-1
Altostratus	0.35-0.45
Stratocumulus	0.3-0.6
Nimbostratus	0.6-0.7
Stratus	0.15-0.3

A.4. Multipath

Specular reflection of radar signals from the ground can have a number of effects on target detection probability, radar image quality and tracking accuracy.

Figure A.15 shows that if the antenna beamwidth is sufficiently wide or the grazing angle sufficiently low that the energy radiating from the antenna reaches the target via two separate paths, one is the direct line-of-sight path from the radar to the target and the other is the path reflected from the surface of the earth. The echo that is re-radiated by the target arrives back at the radar along the same two paths, so the magnitude of the resultant echo signal will depend on the amplitudes and relative phase differences between the direct and the reflected paths [175].

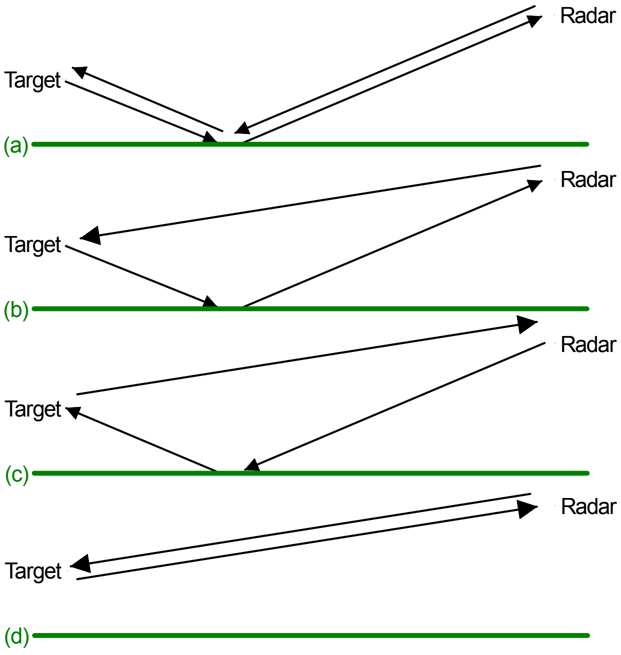

Figure A.15: Possible paths taken by a radar signal between the radar and the target

Modifications to the field strength, (V/m), at the target caused by the presence of the surface are expressed by the ratio η. In general the reflection coefficient from the surface may be considered as a complex quantity

$$\Gamma = \rho \exp(j\varphi), \tag{A.14}$$

where ρ is the real part of the reflection coefficient and φ the phase shift on reflection.

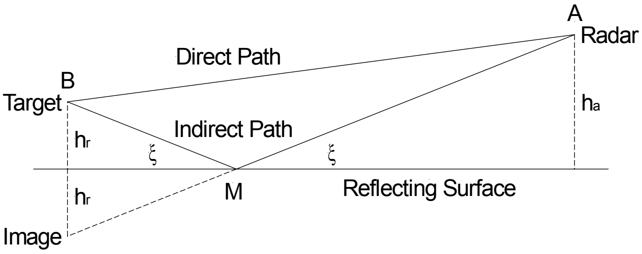

Figure A.16: Multipath interference geometry for a flat earth

---

In the simplest case, it can be assumed that the ground is perfectly reflecting and that $\Gamma = -1$, so the reflected wave suffers no change in amplitude but its phase is shifted by 180°. In Figure A.16, the difference between the reflected path AMB and the direct path AB for range $R \gg h_a$ is then given by

$$\Delta = 2h_a \sin\xi \,. \tag{A.15}$$

For small grazing angle, ξ, and $\sin\xi$ may be replaced by $(h_a+h_t)/R$ to produce

$$\Delta = \frac{2h_a(h_a + h_t)}{R}\,. \tag{A.16}$$

Finally if the target height h_t is much lower than the radar height h_a, then the path-length difference is further simplified to

$$\Delta \approx \frac{2h_a h_t}{R}\,. \tag{A.17}$$

The total phase difference (including the 180°) between the direct and reflected signals as they combine at the target is

$$\psi = \psi_d + \psi_r = \frac{2\pi}{\lambda}\frac{2h_a h_t}{R} + \pi \,. \tag{A.18}$$

The vector sum of the two signals with the same amplitude, but a phase difference ψ is

$$2(1+\cos\psi)^{1/2} \tag{A.19}$$

Since the ratio of the direct and the reflected powers at the target is the square of the amplitude

$$\eta^2 = 2\left(1 - \cos\frac{4\pi h_a h_t}{\lambda R}\right) = 4\sin^2\frac{2\pi h_a h_t}{\lambda R}\,. \tag{A.20}$$

By reciprocity, the path from the target back to the radar follows the same two paths, so the power ratio back at the radar is

$$\eta^4 = 16\sin^4\frac{2\pi h_a h_t}{\lambda R}\,. \tag{A.21}$$

The range equation describing the received echo power must be modified by the propagation factor η^4 (often also called F^4).

Appendix B.

Mutual Interference

B.1. Introduction

Mutual interference between radars is likely if they are operating in the same frequency band. This will result in degraded performance, and may even result in the generation of spurious targets.

The typical sensor payload for an AGV would include an FMICW radar for long-range feature identification and an FMCW radar for short range imaging along with a plethora of laser scanners and cameras. It can be assumed that the FMCW units would be based on automotive radar technology [140], while the FMICW units would have specifications similar to those described in Chapter 5.

Interference may be generated by another radar on the same vehicle, from the radar on another autonomous vehicle or from one of a large variety of automotive radar systems that are under development at this time. Most of these radars are based on FMCW principles [147], [164], [81], [101], a few use pulsed Doppler [95] and some, conventional pulse techniques.

B.2. Typical FMCW Radar Performance Specifications

The specifications for a typical automotive FMCW radar presented in Table B.1.

Table B.1: Typical automotive radar characteristics

Item	**Specification**
Frequency	76-77GHz
Output Power	<10mW
Range	0-120m (passenger car)
Range Resolution	1m
Relative Speed	-100 to + 200km/h
Speed resolution	1km/h
Detection Angle	+/-8°
Multiple Target Detection	Yes
Frame rate	100ms

FMCW systems are generally used in these applications as the required transmitter power is low. The homodyne process requires a single oscillator and they are capable of resolving both position and velocity to the required accuracy if the appropriate modulation is used. Pulsed Doppler units generally have longer pulse widths and poorer range resolutions than their pulsed cousins, but they do provide velocity measurements, while the latter must use successive range measurements to infer the relative velocity.

Antenna gains are quite low because of the limited aperture available for these devices. Angular target positions are either obtained by physically scanning the antenna or by processing the returns from multiple beams.

B.3. Spectrum Utilisation

Restrictions imposed by the Australian Communications Authority (ACA) limit the width of the spectrum that can be used in the 77GHz automotive and in the 94GHz experimental bands. At 77GHz the limit is only 2GHz (76-78GHz) and at 94GHz the limit is 4.9GHz (94.1-100GHz) in two bands. It is unlikely that these restrictions will be waived for autonomous research activities.

B.4. Sensitivity and Interference for FMCW Radars

For consistency, a standard target with a RCS of 1m^2 will be assumed. This may be a point target (trihedral reflector, vehicle, fence post etc.) or a distributed target (ground surface, rocks, trees etc.) with the appropriate reflectivity and gate size.

The return from such a target with a RCS of 1m^2 using a radar with the characteristics discussed above at various ranges and weather conditions is shown in Figure B.1. This is an extremely optimistic model which does not consider any of the phase-noise effects discussed in Appendix F.

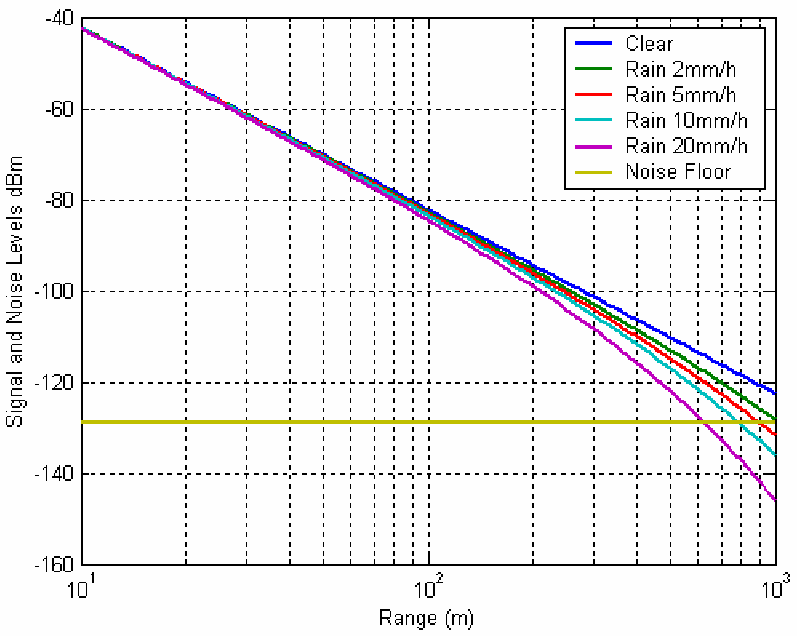

Figure B.1: FMCW radar signal level from a 1m^2 target under different weather conditions

For a detection probability P_d = 0.95 and a probability of false alarm, $P_{fa} = 10^{-6}$, assuming a fluctuating target, the required SNR = 13.6 + 10 = 26.6dB. This is lower than the 30dB achieved at a range of 200m for a rainfall rate of 20mm/h determined from Figure B.1 and so detection is assured. Any extraneous signal within the radar band with a level significantly larger than the -128dBm noise floor could conceivably interfere with the radar.

A simulation model was developed to test the interference mechanisms, and a typical return for a target vehicle at 70m and a signal to noise ratio of 30dB (plotted with an arbitrary dB scale) is shown in Figure B.2.

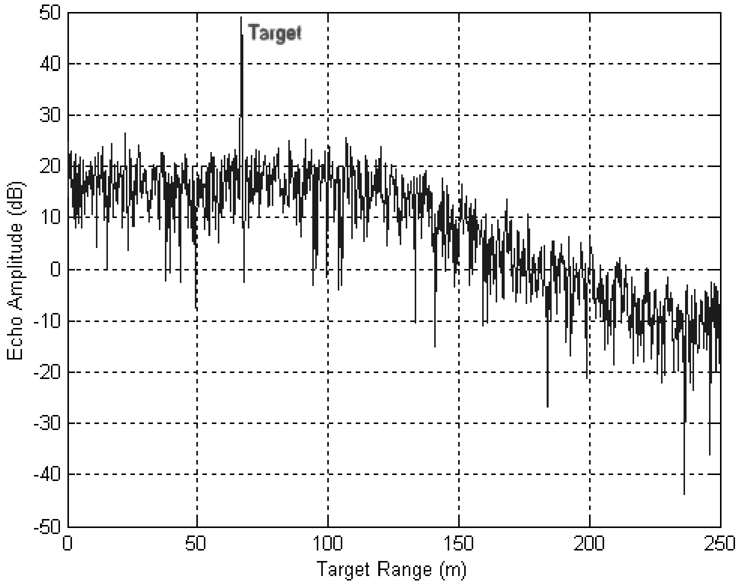

Figure B.2: Radar simulation output showing a 1m^2 point target at a range of 70m

B.4.1. Interfering Source Levels

It can easily be shown that the power received by one radar system from transmissions by another is

$$P_r = \frac{P_t G_t G_r \lambda^2}{(4\pi)^2 R^2}, \tag{B.1}$$

where the received power is P_r (W), the radiated power is P_t (W), G_t and G_r are respectively the transmitter and receiver antenna gains, λ is the wavelength (m) and R is the distance between transmitter and receiver (m).

For a transmit power of 10mW and antenna gains of 34dB for both the transmitter and the receiver, the interference levels are as shown in Figure B.3 below.

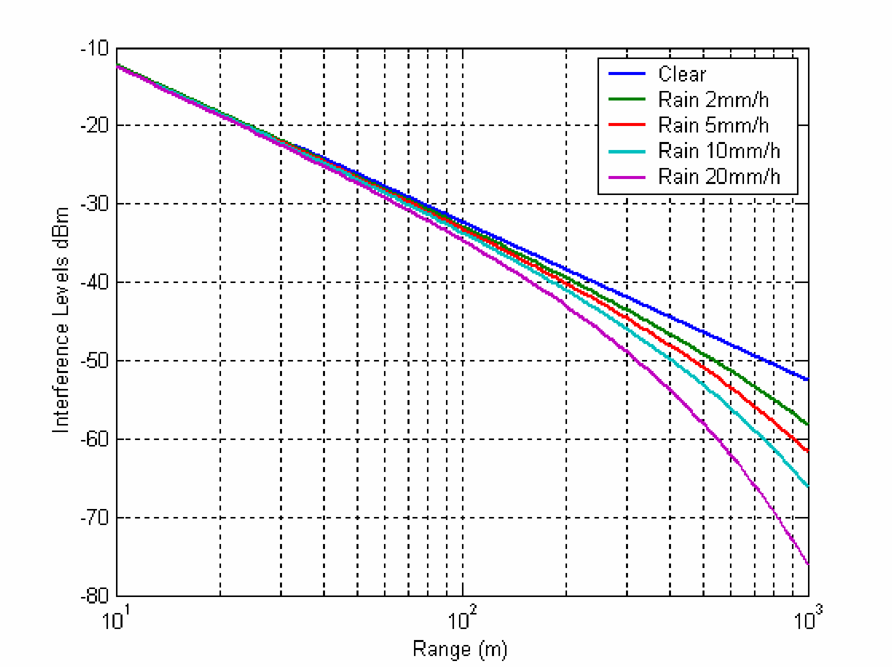

Figure B.3: FMCW Radar Mutual Interference Levels

From an examination of the signal levels in Figure B.1 and Figure B.3, it can be seen that the potential interference level by an FMCW radar at 200m is more than 50dB higher than the return from a $1m^2$ target at the same range.

B.4.2. Effect of Sidelobes

It is difficult to produce millimetre-wave antennas with near-in sidelobes of much less than -18dB. Thus, even if the mutual irradiation is only in the sidelobes of both the radars, the signal level drops by only 36dB and the interfering signal is still 14dB larger than the target return.

The magnitude of the sidelobes decreases with angle, and so a point will be reached beyond which the interference levels are smaller than the echo returns and can be ignored.

B.4.3. Effect of Target

For an AGV navigating through unstructured natural terrain, the target RCS will usually be much smaller than the $1m^2$ specified in the analysis. This implies that interference effects will be more severe in general if there is an overlap in the main beam or close-in sidelobes.

Because most natural objects have rough surfaces, scattering will be diffuse and so the probability of interference by secondary reflection will be limited. This is not the case in built-up areas where reflections will often be specular (road surfaces, walls etc.), and the probability that a secondary reflection large enough to cause interference to occur is high.

B.4.4. Effect of the Operating Band

It has been stated that there is a 2GHz band available for automotive radars, and the bandwidth of individual radars is 200MHz. This allows a total of ten vehicles to operate without interference. Assuming that the bands are equally likely, then the probability of the two radars sharing the same band is 0.1. If the radars can be allocated any 200MHz wide slot, then the probability that there will be some frequency overlap increases to $P_{ovr} = 0.22$.

B.4.5. Identical Radar Systems

For FMCW radars with identical triangular swept bandwidths and sweep times but with random relative phases, then the scenario shown in Figure B.4 can be assumed.

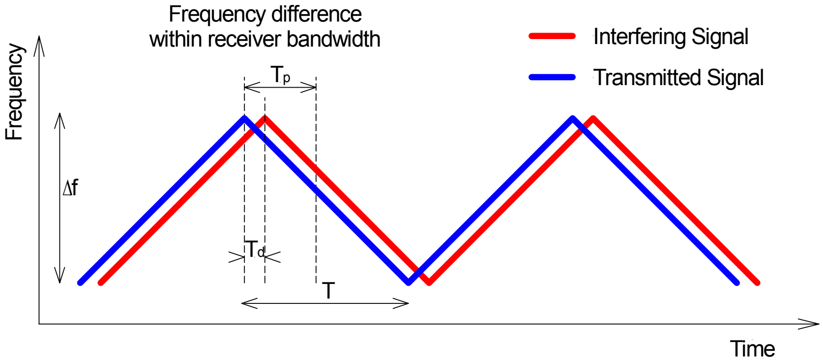

Figure B.4: Two Identical FMCW radars operating with random relative phase

If the relative phase of the interfering signal is anything within the T_p region (below the flat red trace in Figure B.5) then the beat frequency generated by the two signals will be within the receiver bandwidth, and the return will be interpreted as a target at a fixed range.

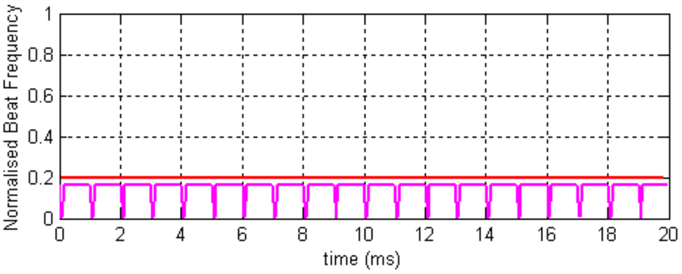

Figure B.5: beat signal for in-phase radars with the whole of the interference signal within the receiver bandwidth (<0.2)

This interference is shown clearly in the FMCW radar simulation output shown in Figure B.6, where a target echo can be seen at a range of 70m and the interference which is 30dB larger than the target, is present at a range of 100m.

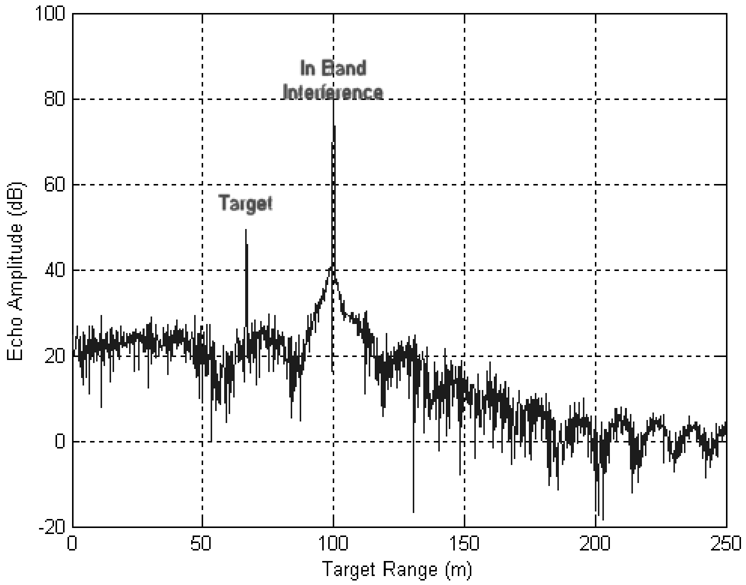

Figure B.6: Radar output for in-band interference with a magnitude 30dB larger than target return

For a total frequency sweep of Δf (Hz), then it is easy to show that the beat frequency, f_b, during the period where both of the sweeps are either increasing or decreasing is

$$f_b = \frac{T_d}{T}\Delta f\,. \tag{B.2}$$

For a typical automotive radar with a total swept frequency of $\Delta f = 200$MHz, a sweep time of $T = 1$ms and a maximum operating range of 200m, the round-trip time will be $T_d = T_p = 1.33\mu$s and the maximum beat frequency within the receiver bandwidth will be 267kHz.

If the relative phase moves out of this region, then the majority of the beat signal will be outside the receiver band, but during the crossover period when one sweep is increasing and the other is decreasing, the beat signal will sweep through the band in 1.33μs as shown in Figure B.7.

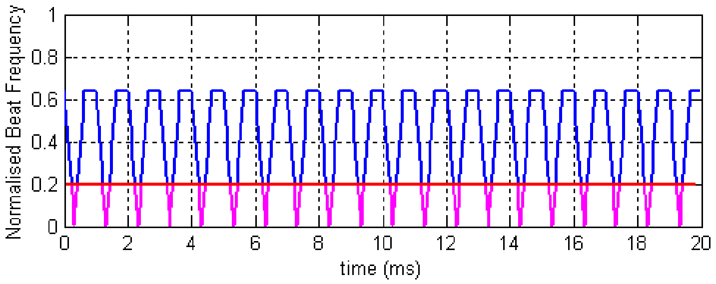

Figure B.7: Beat signal for out of phase radars showing the majority of the interference out-of-band (blue) and some in-band (magenta)

Obviously, it is not possible to reproduce the actual signal in so short a time, and so the magnitude of the interference would appear as a narrow pulse at the output of the mixer. The spectral width of such a pulse is very wide, and it would appear as an increase in the noise floor along with some sampling artefacts as shown in Figure B.8.

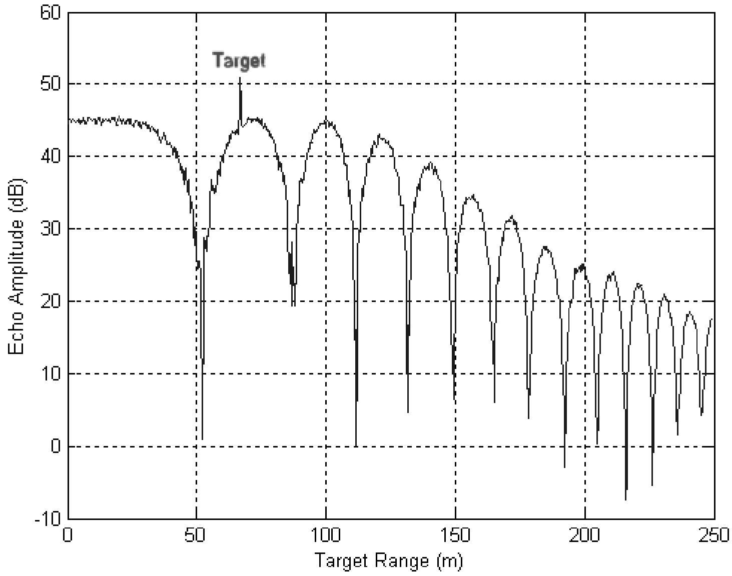

Figure B.8: Radar output for out-of-band Interference with a magnitude 30dB larger than the target return

The magnitude of the increase in the noise floor is directly proportional to the size of the interfering signal until the input stages of the receiver become saturated, after which other effects dominate. In this case, whereas the target SNR was about 25dB in the absence of interference, it has been reduced to only 5dB.

The probability of this out-of-band interference occurring is much higher than of the in-band interference because $T_p << T$ and the probability, assuming a uniformly distributed phase difference between the two signals, is

$$P_p = 1 - \frac{T_p}{2T} = 0.9993 \,. \tag{B.3}$$

It would appear from this analysis that if the two radars are operating in the same RF band, they will interfere, either by occasionally generating a fixed frequency spurious target at some arbitrary range, or by increasing the radar noise floor significantly for the remainder of the time.

In the general case when both the centre frequency and the phase are shifted, then a number of different interference possibilities exist, as shown in Figure B.9.

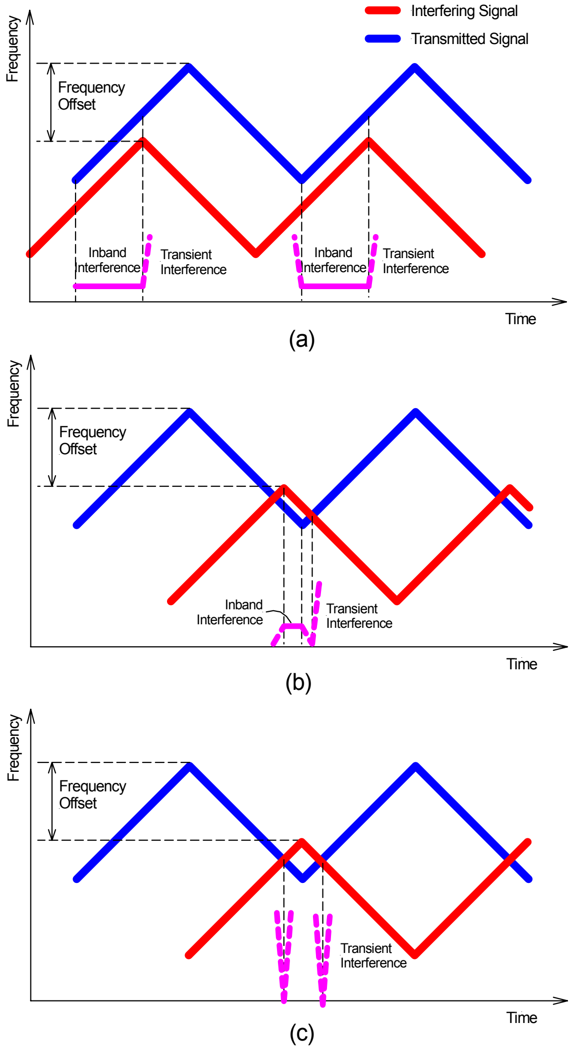

Figure B.9: Interference between FMCW radars with identical sweep periods but shifted in phase and offset in frequency.

It is clear from the figure that the duration of the in-band interference is inversely proportional to the frequency offset between the two signals until it exceeds Δf, after which no interference will occur. In contrast, the duration of the transient interference pulses remains constant, with the intra-pulse period being inversely proportional to the offset.

As with the zero offset frequency case, the probability that in-band interference will occur is very low but in this case the probability of transient interference occurring is proportional to the frequency offset, f_{off}. For a uniform distribution of frequency offset between $-\Delta f$ and $+\Delta f$ the probability is

$$P_p \approx \frac{1}{\Delta f}\int_0^{\Delta f} 1-\frac{f_{off}}{\Delta f}df = 0.5 \,. \qquad \text{(B.4)}$$

The combined probability that there will be a frequency overlap ($P_{ovr} = 0.22$) and that transient interference will occur ($P_p \approx 0.5$) is the product of the two, making $P_{tot} = 0.11$.

B.4.6. Similar Radars

If two different brands of radar are available with slightly different sweep bandwidths or sweep times, then the problem becomes much more involved. In the example shown in Figure B.10 there is a small difference between the sweep times of the two radars but the bandwidths are the same.

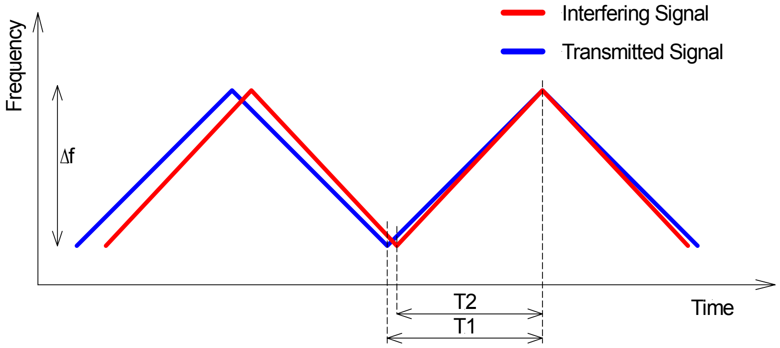

Figure B.10: Two FMCW radars with slightly different sweep times with a phase relationship that changes with time

In this case, as the figure shows, the phase difference between the transmitted and interfering signal changes with time. If the two periods are similar, this will result in the beat frequency changing over the sweep to generate a wide band of interference that will move slowly through the receiver bandwidth as shown by the simulated radar output spectrum in Figure B.11.

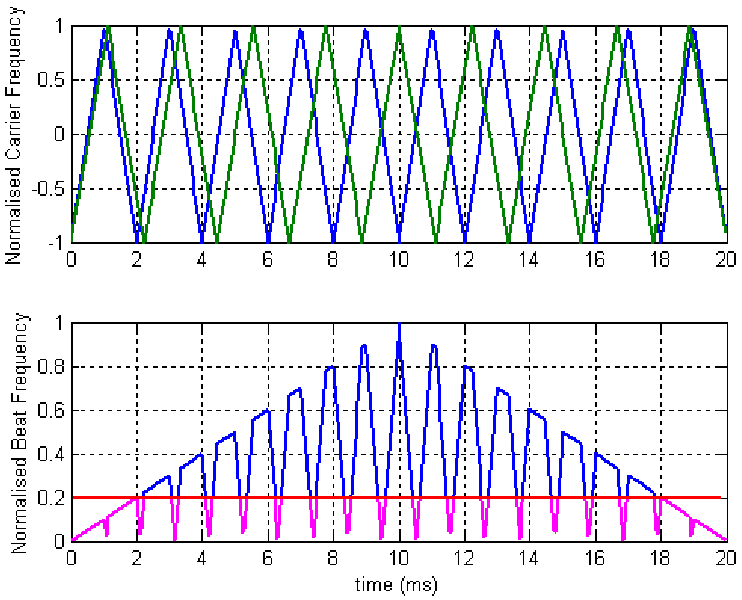

Figure B.11: Interference between FMCW radars with slightly different periods, showing blue out-of-band interference and magenta in-band interference

As with the previous case, even when the beat signal is out-of-band, the turn-around period will inject high amplitude impulses into the receiver with the associated increase in the noise floor as shown in Figure B.12.

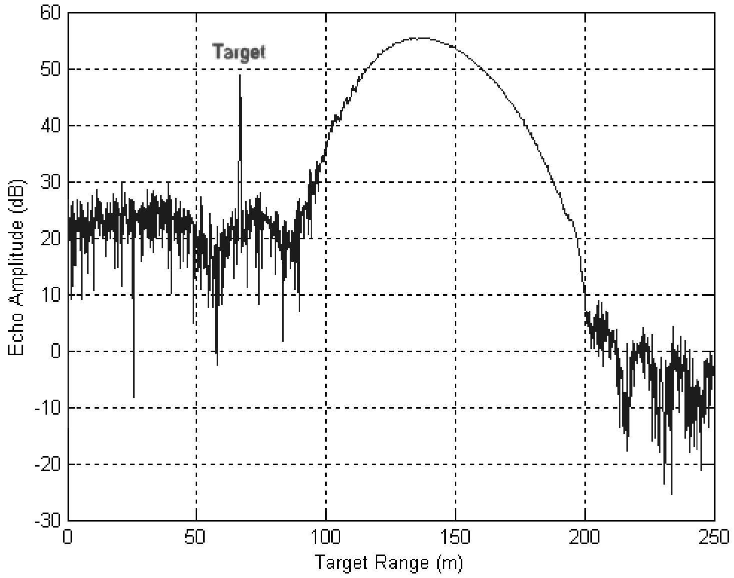

Figure B.12: Radar output interference for two FMCW radars with slightly different sweep periods (1.01 difference) with the interference signal level 30dB larger than the target return

If the two periods are significantly different, then the relative phase will change much more quickly and the beat frequency will move through the receiver bandwidth during a single sweep. An example of the simulated radar output is shown in Figure B.13 and Figure B.14.

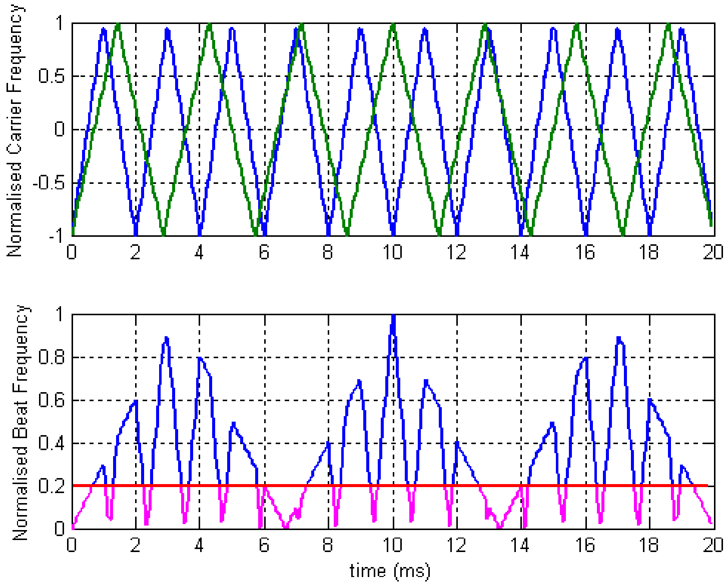

Figure B.13: Interference between FMCW radars with different periods, showing blue out-of-band interference and magenta in-band interference

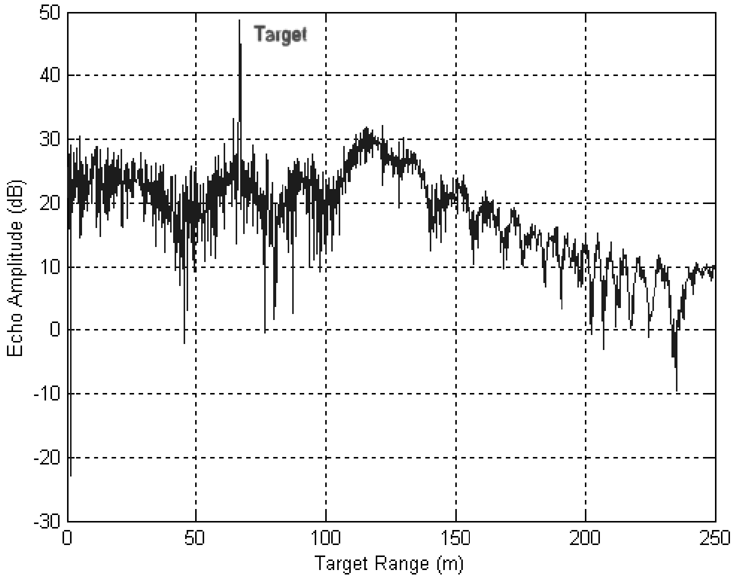

Figure B.14: Radar output interference for two FMCW radars with significantly different sweep periods (1.2 difference) with the interference signal level 30dB larger than the target return

With the particular parameters used for this example, the signal appears fleetingly at the start of the sweep, and then not again, so some ripples are seen in the noise floor and only a small interference return is seen at a range between 100 and 140m.

B.5. Techniques to Minimise Interference

To minimize the effects of mutual interference, the following should be considered when the radar system is designed [166], [183]:

- Use a narrow antenna beam that is physically scanned to minimize the probability of main-lobe interference,
- Use DSP techniques to process the received signal either pre or post FFT,
- Add jitter to both scan and sweep times to eliminate the possibility of coherence between the radar and the interference source.

B.5.1. Pre-FFT Signal Processing

The simplest interference suppression technique, in the time domain, is to clip the received signal amplitude, or to substitute zeros for the received signal over the period of any transient interference. These functions can be tailored to minimize edge transients by windowing appropriately. As an extension, it is possible to restore the original signal over a short period by extrapolation from a few pre-interference samples if the signal to noise ratio is sufficiently good [183].

In-band interference of long duration can be removed by an adaptive notch-filter adjusted to the interfering frequency.

B.5.2. Post FFT Signal Processing

If the interference is narrow band and constrained to within a single FFT bin, then a notch filter in the time domain can be replaced by a FIR filter in the frequency domain [183],

$$H(z) = 1 - a.z^{-1}, \qquad \text{(B.5)}$$

where $a = \exp(2\pi jM / N)$, M is the post FFT sample containing the interference frequency and N is the length of the FFT.

B.5.3. Detection and Tracking

Much of the interference mitigation occurs during the post-processing phase when targets are identified using CFAR methods [165], and when the range, range rate and acceleration are extracted from multiple detected target returns and track files are established and updated for each target [166].

Classical nearest neighbour and joint probabilistic data-association algorithms are often used to associate new measurements with existing tracks. However in heavy clutter these perform poorly and superior algorithms have been developed specifically for automotive applications [142].

It should be noted that notwithstanding the importance of the tracking phase, if the SNR of the target return is low, then the track initiation and target association processes will be compromised. Hence it is important to ensure that the amount of mutual interference is minimized.

B.5.4. Examples of Interference Reduction

In the case of the in-band interference shown in Figure B.6, if the frequency of the interference is known, a simple notch filter is can remove the offending signal with minimal disruption as shown in Figure B.15.

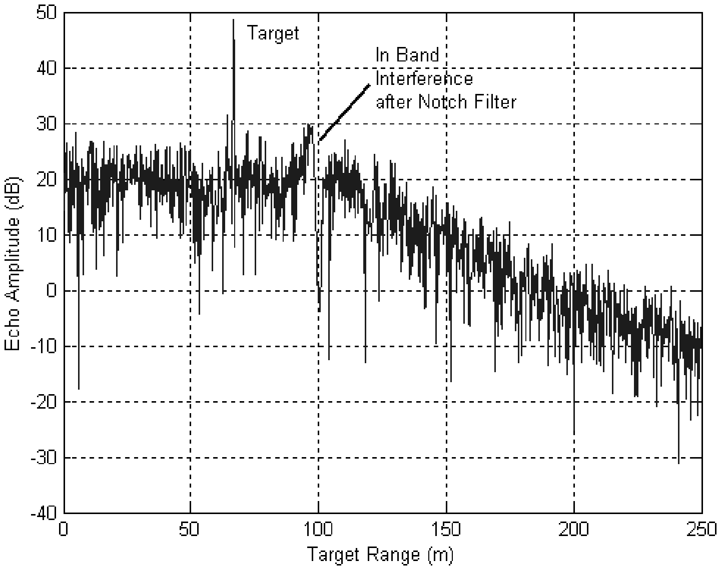

Figure B.15. Effectiveness of a notch filter to remove in-band interference

The more ubiquitous transient interference shown in Figure B.16a can be dealt with quite effectively by substituting zeros for the high-amplitude transient as shown.

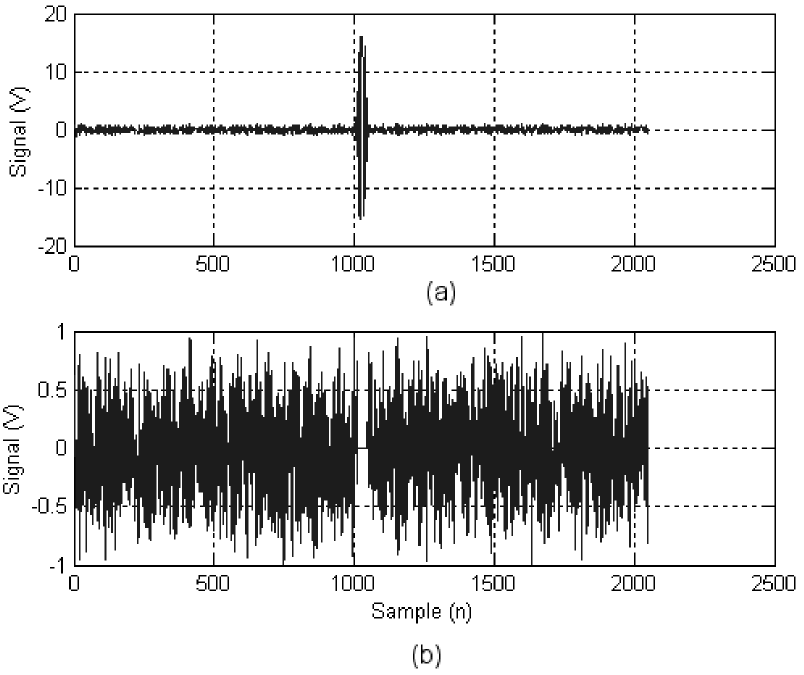

Figure B.16: Transient interference in the time-domain in shown in (a). This can be removed by substituting zeros during the interference period as shown in (b)

The effect on the post FFT spectrum is quite dramatic as shown in Figure B.17 when compared to the spectrum reproduced in Figure B.8. The residual noise, most noticeable at long range is caused by the abrupt masking of the interference.

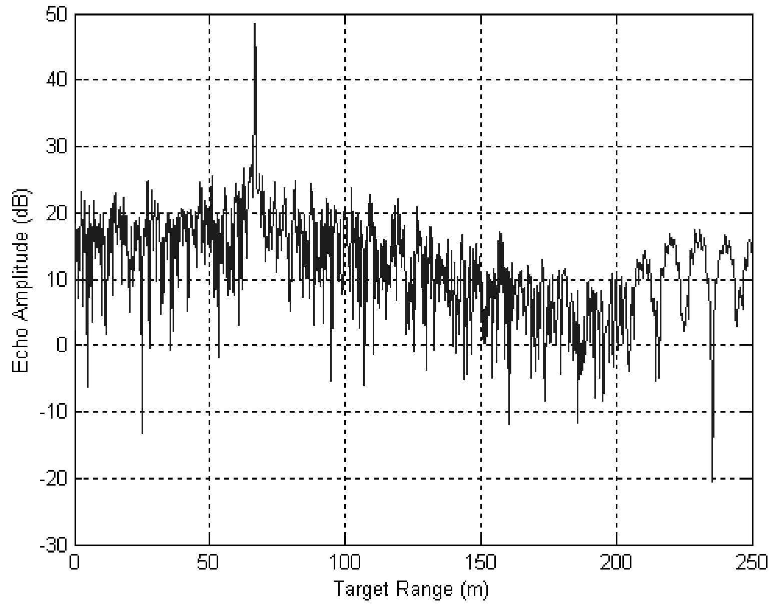

Figure B.17: Post FFT radar spectrum for transient interference after masking by zeros

It can be concluded from these examples that if the nature of the interference can be determined, then simple signal processing can reduce its effect significantly.

Under some circumstances, however, where the sweep time differences are short such as those shown in Figure B.12 and Figure B.14, where the nature of the interference is of the form of a chirp, then simple techniques are not effective. In these cases, the only effective measure is to ignore the corrupt sample and rely on the fact that the interference will be fleeting.

Applying a pseudo-random dither to the sweep period may not eliminate this form of interference, but it would ensure that it did not repeat at regular intervals.

B.6. Sensitivity and Interference for FMCW and FMICW Radars

The FMICW radar discussed in Chapter 5 has a transmit power of 300mW, a 50% duty cycle and an antenna gain of 44dB (to improve the angular resolution at long range). Figure B.18 shows the detection range during normal and inclement weather. It can be seen that this radar is operational out to 3km in good weather but its performance severely affected due to rain attenuation.

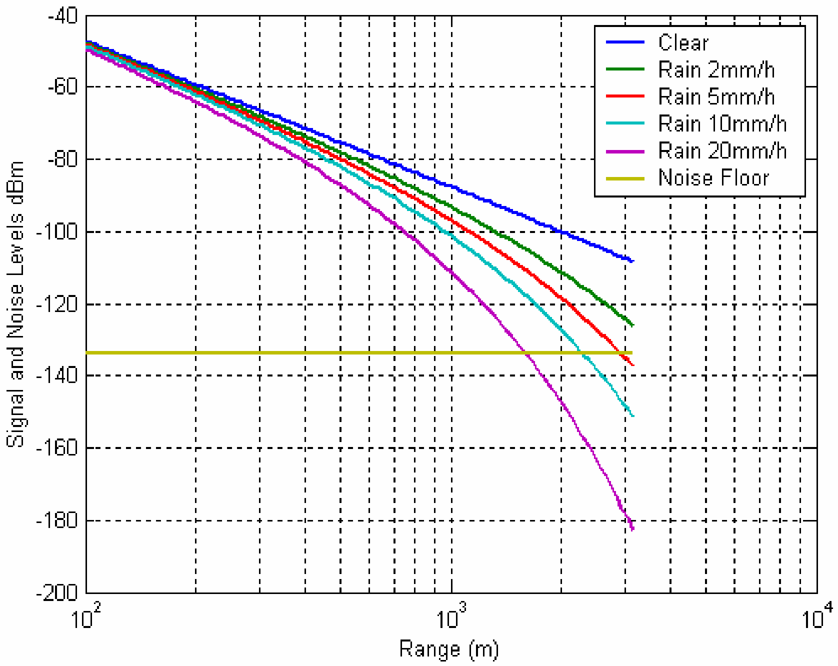

Figure B.18: FMICW radar signal level from a 1m^2 target under different weather conditions

Because of the higher transmit power of the FMICW radar it is more likely to interfere with the FMCW radar than vice versa. Figure B.19 shows the peak signal received by the latter if all of the radar characteristics with the exception of the transmitter power remain the same.

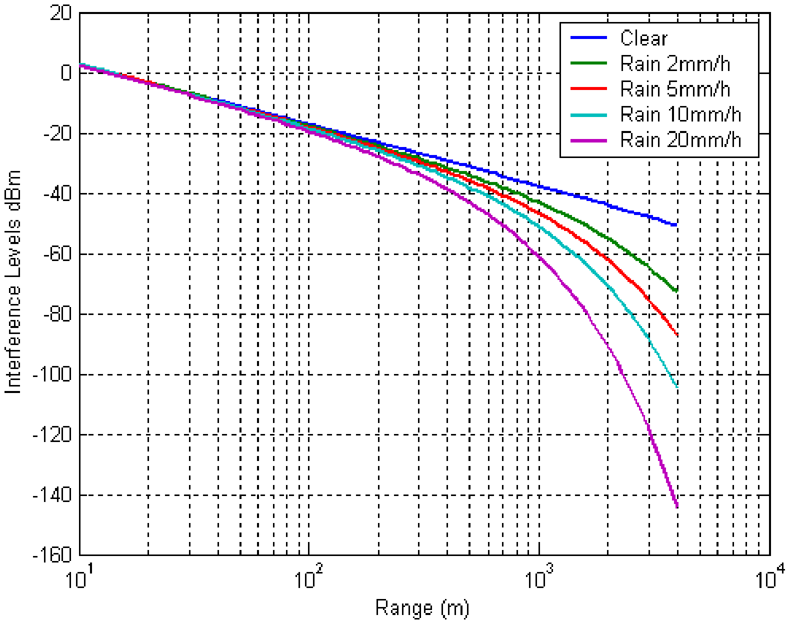

Figure B.19: Interference levels in an FMCW radar being illuminated by an FMICW radar

For an FMCW radar illuminating a $1m^2$ target at a range of 200m, the received signal level in clear air is about -94dBm. The interfering signal radiated by an FMICW radar at a range of 2km is -44dBm, 50dB higher than this.

As discussed previously, the actual signal levels will be affected by the sidelobe levels, the operating band and the target. In the following scenario, it is assumed that the two bands are completely overlapping, but that the interfering signal is only 15dB higher than the return from the target. Figure B.20 shows two full cycles of the FMCW radar with a sweep time of 1ms and almost twelve cycles of the FMICW radar with a sweep time of 180μs. It can be seen that the beat frequency is in-band for a couple of brief periods during each FMCW cycle.

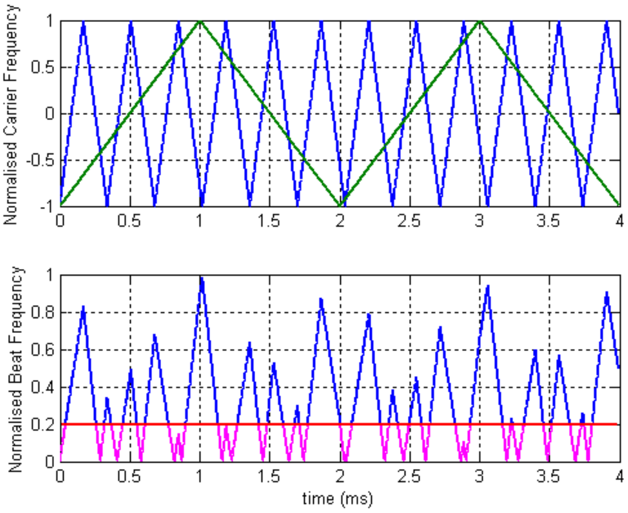

Figure B.20: Interference of an FMCW radar by an FMICW radar with different periods, showing blue out-of-band interference and magenta in-band interference

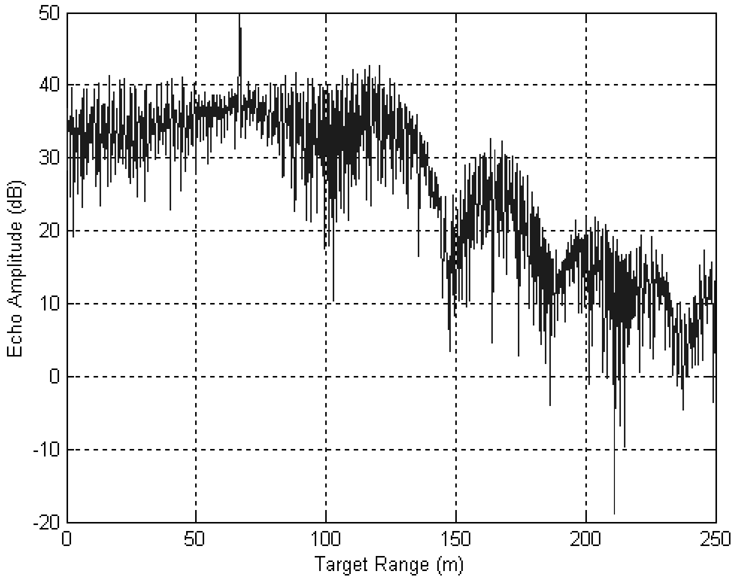

Figure B.21: Radar interference of an FMCW radar by an FMICW radar with different sweep periods (1ms and 170μs) with the interference signal level 15dB larger than the target return

The output spectrum from the FMCW radar in Figure B.21 shows the target return as before, but because of the short duration and random timing of the interference signal this appears as wideband noise that has increased the noise floor by about 20dB over the whole receiver bandwidth.

Even with this amount of interference, the P_d of the true target is reduced because of the low SNR. If the magnitude of the interfering signal is increased by decreasing the range or altering the antenna alignment, then the true target signal could be completely swamped.

Appendix C.

Implementation of 94GHz Pulsed Radar Front-End

C.1. Overview

The structure of the radar system that is described in the following section is based on a coherent radar developed as a short-range demonstrator [55]. The maximum range of interest was 3km which allowed for a pulse repetition frequency, f_s, of 50kHz as determined by

$$f_s = \frac{c}{2R}. \tag{C.1}$$

A nominal range resolution, δR, of about 5m was required which determined the pulse width requirement of τ = 50ns as calculated using (C.2). However, due to the characteristics of the transmitter which is discussed in the next section, this was not a straightforward process.

$$\delta R = \frac{c\tau}{2} \tag{C.2}$$

A single-stage pulsed IMPATT transmitter operating at 94GHz was implemented along with a conventional super-heterodyne receiver to produce the configuration shown in Figure C.1. Because of the cost and poor performance of amplifiers at 94GHz it was decided to dispense with RF amplification and feed a mixer directly. The local oscillator (LO) was a conventional 2nd harmonic Gunn device tuned to 93.7GHz to produce an IF frequency of 300MHz.

The IF stage consisted of a wide-band amplifier and a matched filter implemented as a four stage bandpass filter. This was followed by a fast rise-time successive-detection-log-amplifier (SDLA).

A low insertion-loss ferrite junction circulator operated as a duplexer to channel the transmitted pulses into the horn-lens antenna and to feed the received echo from the antenna back into the mixer.

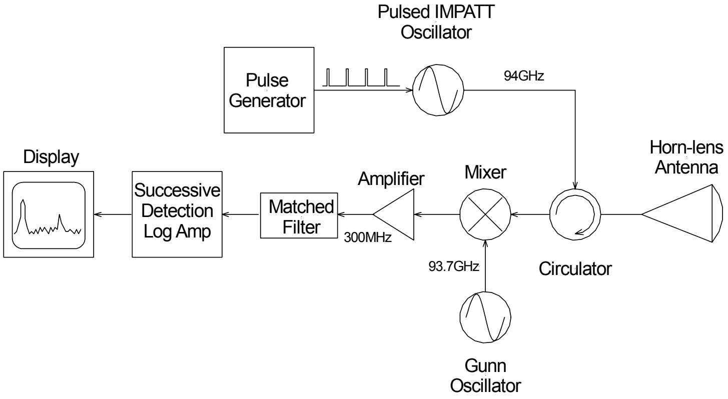

Figure C.1: Schematic block diagram showing the major components of a typical non-coherent pulsed millimetre-wave radar system

C.2. Pulsed IMPATT Transmitter

The basic IMPATT diode structure was proposed in 1958 [161] and alternatives which were more suitable for millimetre-wave operation were developed later.

A diode is typically mounted in a reduced-height waveguide along with a bias pin and an adjustable back short to supply power and match the impedance respectively as shown in Figure C.2.

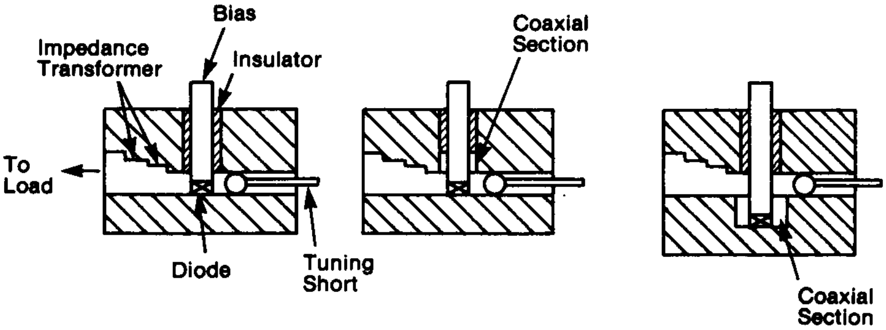

Figure C.2: Cut-away cross-sections of typical millimetre-wave oscillator circuits [20]

The optimum operational frequency and output power both increase with current density, whereas the maximum current-densities that can be applied to CW diodes are limited by their thermal characteristics. For short pulses, the diodes are not thermally limited [20] and the current density can be extended until space-charge effects cause saturation. More information on IMPATT-diode physics can be found in Appendix G.

One of the unique characteristics of pulsed IMPATT-diodes is the existence of chirp which is a consequence of the dramatic junction-temperature rise during the pulse. This chirp can be compensated for by providing an upward ramp on the current pulse with the slope adjusted to balance the thermal effects. The critical section of the pulse-forming network to achieve this nonlinear current pulse is a tapped delay line that produces ten individual outputs spaced 10ns apart. The amplitudes of these pulses can be independently adjusted and then summed to produce a pulse of the correct shape. This pulse is then gated to the required width (10ns < τ<100ns) before passing into a current amplifier that biases the IMPATT diode.

Unfortunately, even with fairly sophisticated programmable pulsed current sources, such as the one described, it is not possible to eliminate this chirp completely, and this leads to compromises in the design and hence performance of the matched filter that was developed for this application.

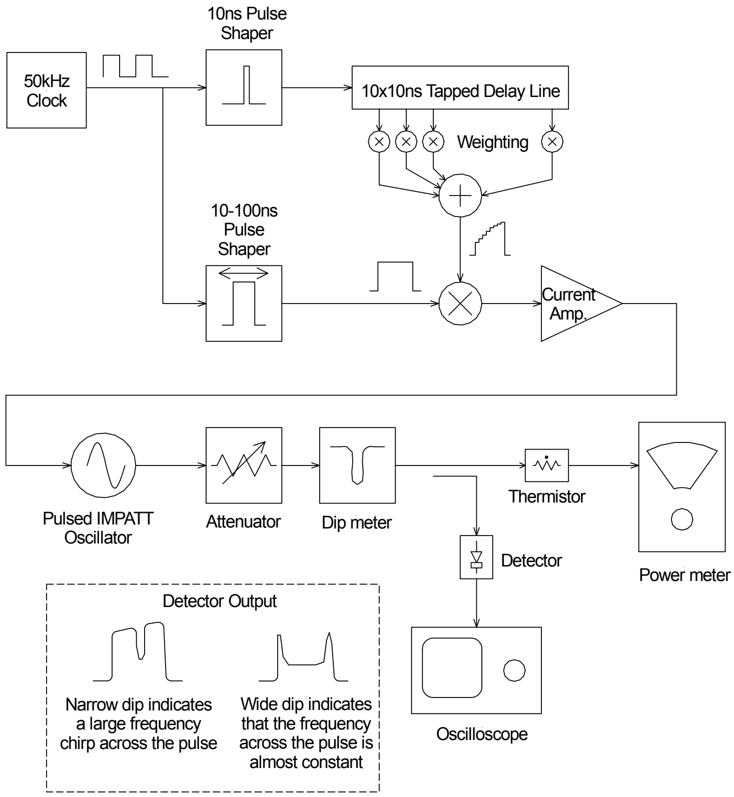

Figure C.3: Simplified schematic of the programmable current source and the test setup used to measure the characteristics of a pulsed IMPATT oscillator

The process of adjusting the current pulse is generally undertaken with the help of the test setup shown Figure C.3. The pulsed IMPATT oscillator output passes through an attenuator to reduce the signal level, to improve matching, and to reduce the effects of load pulling. A dip meter is then set to the frequency of interest before the pulse shape is monitored through a fast detector and a low-impedance load (typically the 50Ω setting on an oscilloscope). The dip meter contains a resonant cavity coupled into the signal path, so at that frequency, the cavity absorbs power and the signal-level output by the device dips.

Figure C.4 shows the measured spectra of 94GHz short pulsed IMPATT oscillators with photograph (a) being that of a high chirp 100ns pulse and (b) that of a 50ns low chirp pulse.

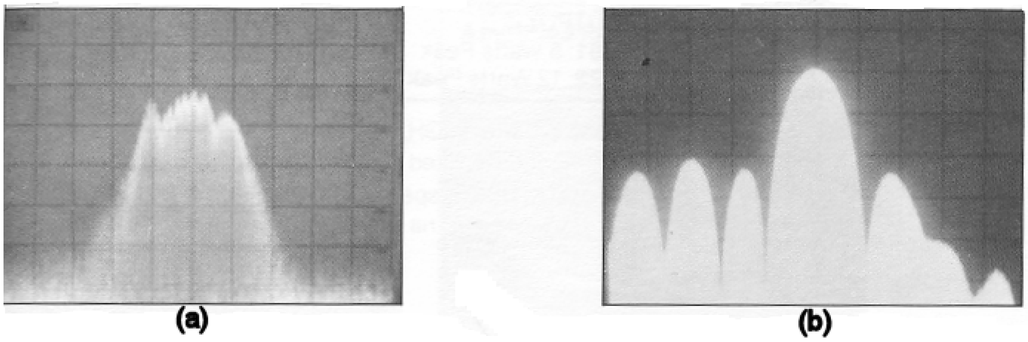

Figure C.4: Pulsed IMPATT oscillator showing (a) large chirp spectrum 100MHz/Div. and (b) small chirp spectrum 20MHz/Div [11].

C.3. The Duplexer

The function of guiding the transmitted signal out through the antenna, as well as the received echo back into the receiver can be accomplished in a number of ways using off-the-shelf components:

- 3dB Directional Coupler, 20dB directivity, 1.6dB Tx insertion loss and 4.6dB Rx insertion loss
- Junction Circulator, 20dB isolation, 0.8dB insertion loss for both Tx and Rx paths.

From both insertion loss and isolation (directivity) perspectives the circulator is either superior or equal to the coupler performance. Though the coupler can handle higher powers, the circulator can handle 5W peak which was sufficient for this application. The circulator is also smaller and lighter than the coupler.

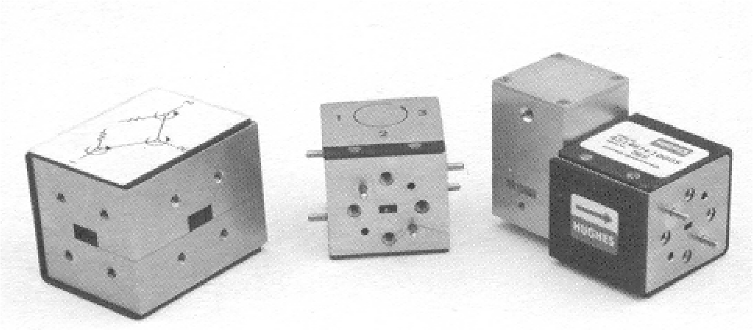

Figure C.5: Y-junction circulators

A junction circulator is a non-linear ferrite device that usually has three matched ports. When there is an input signal at one port, the output appears at the next adjacent port in cyclic order. Thus power is coupled from one port to the next in one direction only.

The most commonly used circulators are the three-port Y-junction types. These consist of a symmetrical junction with waveguides spaced 120° apart with a small ferrite puck (and matching network) mounted at the junction. A strong magnetic field is applied normal to the plane of the disk by a pair of rare-earth magnets placed above and below the waveguide. In the absence of a magnetic field when a signal is injected into one port, two counter-rotating fields are set up which generate a symmetrical standing wave pattern in the disk. When the correct magnetic field is applied, the standing wave pattern rotates by 30° effectively isolating one of the ports and coupling all of the power to the other.

With care, an insertion loss of less than 0.5dB and an isolation of greater than 20dB can be obtained across a wide bandwidth. Impedance matching using small quartz rods[1] can be used to obtain VSWRs of better than 1.3 over the pass-band.

C.4. The Antenna

In a similar manner to the function performed by reflectors, lenses are used in radiating systems to collimate the radiation from a wide angle source like a horn into a narrow beam. The aptly named horn-lens antenna has an advantage over a reflector in the sense that aperture blockage is absent with the result that the efficiency is higher and the sidelobe levels are usually lower for the same aperture.

The antenna constructed for the pulsed radar consisted of a Teflon singlet [55] designed using classic geometric-optics techniques with a rectangular horn mounted at its focal point.

For a Teflon lens with a relative dielectric constant of 2.08 and *F/D*=0.93, the required edge taper for good performance (balance between sidelobe level and gain) is -5dB [20]. For this application, where good quality measurements requiring the lowest possible sidelobe levels were more important than operational range, the edge taper was increased.

The rectangular horn had an aperture of 6×8.7mm that produced equal E and H plane beamwidths. It was designed to illuminate the lens with an edge taper of -15dB. This resulted in a beamwidth constant of about 72 using the nomenclature described in [105].

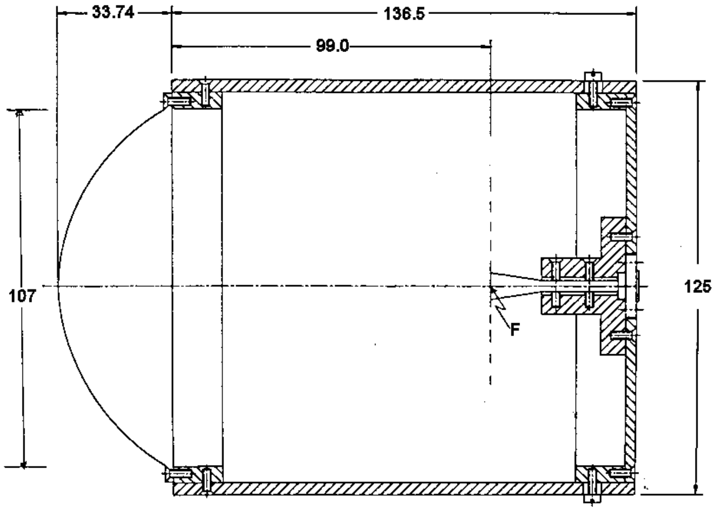

Figure C.6: Horn-lens antenna

---

[1] Demonstrated to the author during a visit to Philips Microwave

The directivity and the beamwidth of the antenna can be predicted

$$G = \frac{4\pi\rho_A A}{\lambda^2} = 6600\,(38\text{dB}), \tag{C.3}$$

$$\theta = \phi = \frac{k\lambda}{d} = 2.16^o, \tag{C.4}$$

where ρ_A – Aperture efficiency (0.55 [106])
A – Lens aperture (m^2)
k – Beamwidth constant (72)
d – Aperture diameter (m)

If no attempt is made to match the lens material to that of the air, a portion of the incident power will be reflected from the surface of the lens, and multiple reflections will occur within the lens. This phenomenon [106] increases the sidelobe levels to the extent that they are seldom lower than -20dB. The average loss due to reflections over all incidence angles and polarisations gives an approximate lens reflection loss in dB

$$\alpha_r = 8.69 \frac{\left(\sqrt{\varepsilon_r} - 1\right)^2}{\left(\sqrt{\varepsilon_r} + 1\right)^2}. \tag{C.5}$$

The attenuation in dB per unit wavelength through the lens is given by

$$\alpha_d = 27.3\sqrt{\varepsilon_r}\tan\delta. \tag{C.6}$$

For Teflon with ε_r = 2.08 and loss tangent, tan δ = 0.0005 and a lens thickness of 34mm, the total attenuation through the whole lens is 0.28 + 0.2 ≈ 0.5dB. The directivity is modified by this loss to produce the final antenna gain of 37.5dB.

Unfortunately no measurements were made to verify this beamwidth and gain, apart from some scans made past corner reflectors in the field.

C.5. Local Oscillator

At the time that this radar was constructed [55], GaAs Gunn diodes that were available commercially could only deliver power effectively to a fundamental frequency of 60GHz. IMPATT oscillators, though they could produce the required output powers, had phase-noise figures about 40dB higher than their Gunn counterparts making them unsuitable for low noise applications [11] and so a 2nd harmonic GaAs Gunn oscillator was developed that produced sufficient power to drive the mixer.

Unlike IMPATT devices, Gunn diodes are not junction but bulk-effect devices in which the negative differential conductance required for oscillation is a property of the semiconductor material. The mechanism responsible in this case is that the carriers (electrons in n-type GaAs) upon gaining energy from the applied field, jump from a low-mass high-mobility energy-band to a higher energy band. In this new state the carriers have higher mass and lower mobility with a resultant dip in current density as the electric field increases.

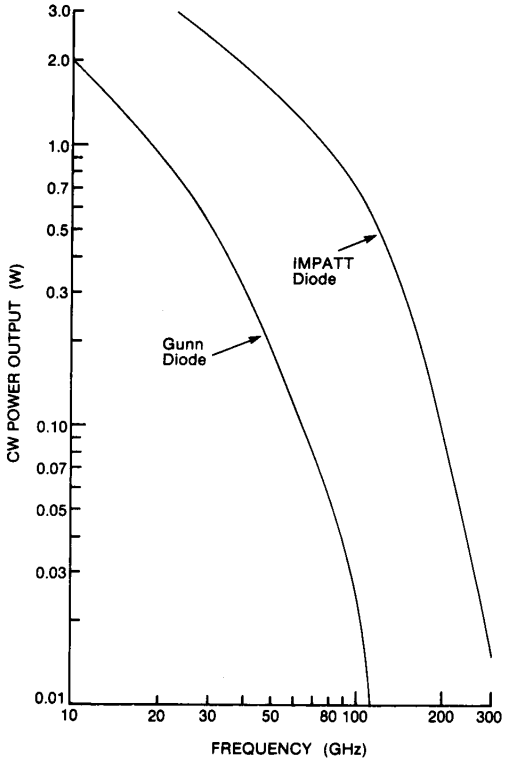

Figure C.7: State of the art in CW Gunn and IMPATT power [20]

Harmonic oscillators have some advantages over their fundamental counterparts including the following:

- They are relatively low noise,
- They are less susceptible to load pulling,
- It is often less expensive to generate the same power using harmonic operation than it is to use a fundamental mode device,
- Low frequency Gunn technology is mature, so good reliability can be expected.

A standard oscillator based on a disk resonator mounted above a Gunn diode in a full height waveguide was implemented which produced an output power of 9dBm at around 94GHz from a 20dBm diode operating at about 47GHz. The single-sideband (SSB) phase noise was -70dBc/Hz at an offset of 100kHz which, contrary to what is stated in [55], is about 10dBs higher than the state-of-the-art at that time [11]. As with IMPATT diodes, the efficiency of GaAs Gunn diode oscillators is very low, and this unit consumed about 5W (5V at 1A) most of which was output as heat which had to be dissipated.

C.6. The mixer

Because the local oscillator output power was limited, it was unable to drive a GaAs mixer, so a standard silicon waveguide-balanced unit manufactured by Hughes Microwave Products (now Millitech) was used. It required a LO drive of only +5dBm (compared to 10dBm for the GaAs unit), but it had a higher double-sideband noise-figure of 6dB. Both mixers were poorly matched to their inputs with a VSWR as high as 2:1, and for this reason an isolator (not shown in Figure C.1) is generally included in the path between the LO and the mixer.

C.7. The amplifier

A standard wide band amplifier (200-600MHz) was designed and built using the Mini-Circuits MAR range of monolithic amplifiers. Though the noise figure was never measured, it was estimated to be about 4dB, and so in conjunction with the mixer conversion loss, it defined the overall noise figure for the radar. The gain of the amplifier was set to supply the appropriate signal level to the SDLA.

C.8. Matched Filter Implementation

It is impractical to design a matched filter for a pulse that can be adjusted in width between 10 to 100ns and which will also chirp by up to 100MHz during this period. A compromise bandpass filter was constructed from cascaded tuned stages, shown in Figure C.8, to accommodate the largest expected bandwidth (100MHz).

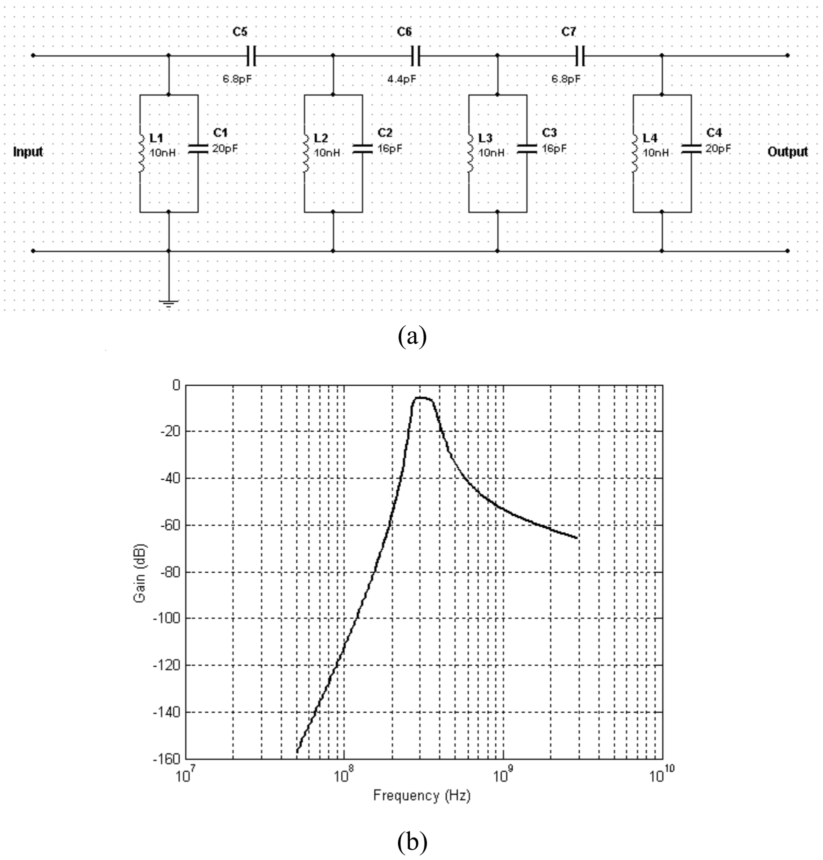

Figure C.8: Passive matched (bandpass) filter implementation for a pulsed millimetre-wave radar system (a) schematic diagram and (b) calculated transfer function

To realise a fairly wideband filter of this nature required that the IF frequency be made as high as was practical for the manufacture of the filter, amplifier and detector, so a centre frequency of 300MHz was selected.

The performance of this filter is hardly "matched" in the true sense. Ideally, either a pulse-compression network should have been implemented to make use of the residual chirp, or the IMPATT oscillator should have been injection locked to a fixed reference and the filter matched to the pulse width. Either way, the performance of the radar would have been superior to that which was achieved.

C.9. Closing the Calibration

Measurements were made using precision trihedral corner reflectors of known cross sections of 0, 10, 20 and 30dBm^2 at a range of about 150m to determine the performance of the system.

The characteristics of the IF chain from the mixer port through the amplifier, matched filter, SDLA and range gating were determined by injecting a CW signal into the input and logging the output to produce Figure C.9. In this configuration a pair of range gates used for split-gate tracking sampled the post SDLA signal to produce sum and difference-channel signals.

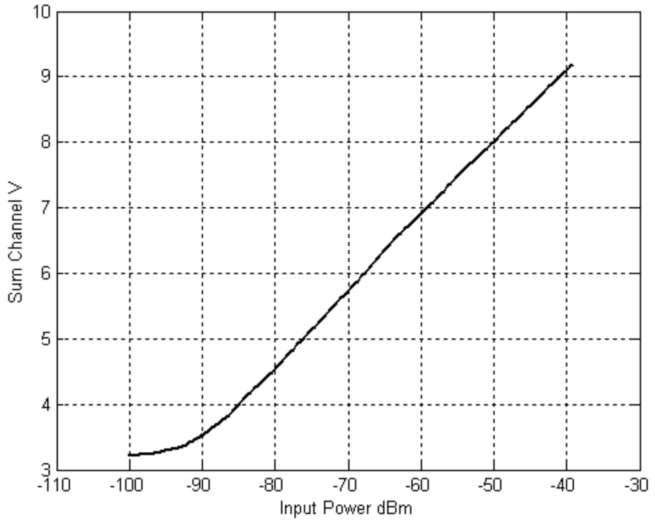

Figure C.9: Measured calibration transfer function for the pulsed millimetre-wave radar receiver chain from after the mixer to the range gate sum channel output

The target reflectors were placed at a range of 146m and the average return signal level measured and logged. These data were then converted to a received IF power level (directly after the mixer).

Table C.1: Measured radar signal levels for different target reflectors

Reflector Cross Section (dBm^2)	Output Voltage (V)	Mixer Output Power (dBm)
Tripod	4.16	-83.6
0	5.85	-69.0
10	7.06	-58.6
20	8.01	-50.0
30	9.49	-36.0

C.9.1. Received Power

The received power was determined at a range R = 146m. Substituting into (C.7) where the transmitted power $P_t = P_{osc} - L_{line} - L_{circ} = 37 - 0.4 - 0.8 = 35.8$dBm, the antenna gain G = 37.5dB and the conversion loss through the mixer, 8.5dB, making the total receiver loss $L = L_{mix} + L_{line} + L_{circ} = 8.5 + 0.4 + 0.8 = 9.7$dB

$$P_r = P_t + 2G + 10\log_{10}\frac{\lambda^2}{(4\pi)^3} + \sigma - L - 40\log_{10} R. \qquad (C.7)$$

A comparison was made between the predicted and measured received powers as shown in Figure C.10.

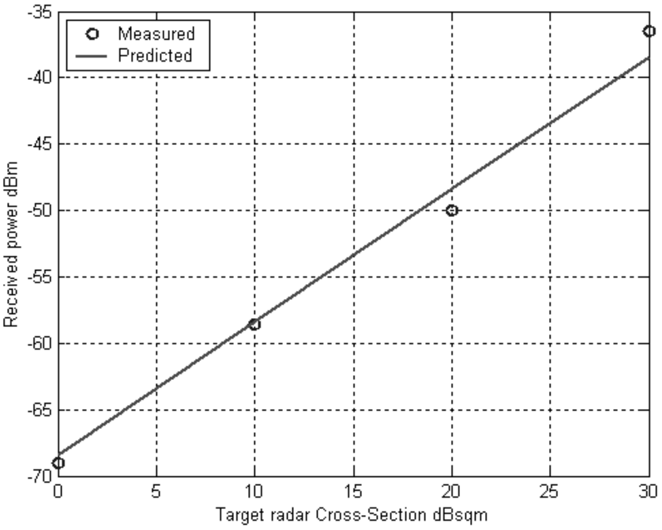

Figure C.10: Comparison between measured and predicted received power at the output of the mixer for a pulsed millimetre-wave radar system illuminating different RCS corner-reflectors

The figure shows that the calibration closed to between 0.22dB for the 10m^2 target and -2.38dB for the 1000m^2 target. This was exceptionally good for a first pass where closure to 3dB is considered to be acceptable [67].

C.9.2. Output Signal to Noise Ratio

The receiver noise figure can be calculated using the standard formula for a cascaded network shown in Figure C.11.

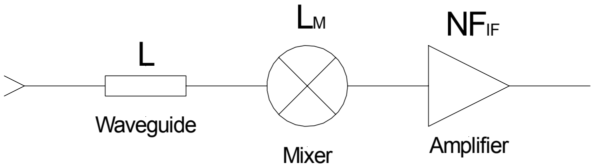

Figure C.11: Receiver schematic used for the calculation of noise figure

It can be shown that the noise figure *NF* for a cascaded receiver chain made up of a number of stages each with gain and individual noise figure is

$$NF = NF_1 + \frac{NF_2 - 1}{G_1} + \frac{NF_3 - 1}{G_1 G_2}. \qquad \text{(C.8)}$$

For the single sided mixer implementation shown in the diagram, substitute $L = NF_1$, $LM = NF_2$, $1/L = G_1$, $1/LM = G_2$ and $NF_{IF} = NF_3$ to obtain the total noise figure

$$NF_{SSB} = L + (L_M - 1) + (NF_{IF} - 1)L.L_M = L.L_M.NF_{IF}. \qquad \text{(C.9)}$$

It can be seen that the noise figure is just the product of all of the losses in the receiver chain and the noise figure of the first amplifier. Operating in dBs requires that these losses be added, so assuming a mixer conversion loss L_m = 8.5dB (equal to the specified SSB noise figure) and an IF amplifier with a noise figure of 4dB as well as line losses $L_{rec} = L_{line} + L_{circ} = 0.4 + 0.8 = 1.2$dB, then the noise figure is

$$NF_{rec} = L_{rec} + L_m + NF_{IF} = 1.2 + 8.5 + 4 = 13.7\text{dB}. \qquad \text{(C.10)}$$

The contributions of stages after the first IF amplifier to the overall noise figure can be neglected because its gain is sufficiently high to make them extremely small.

The total noise power in dBm for a temperature of 290K and a matched filter bandwidth of 100MHz can be calculated

$$P_n = 10\log_{10}(kT\beta) + NF_{tot} = -124 + 13.7 + 30 = -80.3\text{dBm}. \qquad \text{(C.11)}$$

Additional losses that decrease the output SNR include the mismatch of the bandpass filter which is difficult to determine accurately because of the transmitted chirp. In this case as the SNR is referred to the antenna port, the received power will be that calculated by the radar range-equation without any losses, Pr = -48.7dBm. If no additional losses are assumed then for a 10m^2 target at a range of 146m the following SNR can be expected

$$SNR = P_r - P_n - 1 = -48.7 + 80.3 = 31.6\text{dB}. \qquad \text{(C.12)}$$

Measurements made with the radar pointed at the sky gave a mean value for the noise of 3.2V at the sum-channel output. As can be seen from the calibration graph, this is just the noise floor of the IF and baseband sections of the receiver. Assuming that the SDLA is not a limiting factor and that the relationship between the input power and the measured voltage is still linear, then the measured noise floor will be about -91dBm, making the measured SNR = -58.6 + 91 = 32.4dB which is within 0.8dB of that calculated.

C.10. Imaging Performance

As discussed earlier in this thesis, radar images can be made either at steep grazing-angles where the returns are beamwidth-limited, or at shallower grazing-angles where they are range-gate-limited in the range axis.

The clutter image shown in Figure C.12 was made at a grazing angle of 23° where the antenna beam was scanned in a raster manner over a limited angle of view and the ground tracked in range. A reflectivity image was then produced by mapping the sum-channel-signal intensity onto the plane defined by the angular surface.

The angular resolution was determined by producing an image of a corner reflector and noting the size of the associated bright blob. This is depicted by the circle reproduced in the bottom right-hand corner of the image.

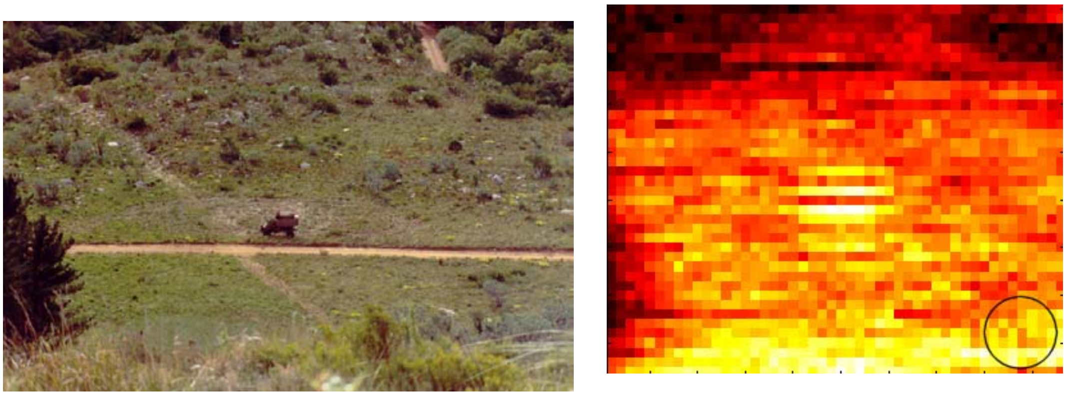

(a) (b)

Figure C.12: Millimetre wave radar test site at a range of 350m and a grazing angle of 23° to the target vehicle (a) Photograph and (b) beamwidth-limited radar image

A number of disadvantages of producing images that rely on the ability of the radar to track the ground surface exist. One problem is the tendency of the radar to lose lock, which happened frequently where a step change in range occurred, or where the target was obscured by a nearby object, as was the case with the pine trees that are visible to the left of both the photograph and the radar image. A second and more fundamental problem is that the range tracker straddles the centroid of the largest target within the beam. This causes the range estimate to jump from point-target to point-target rather than follow the ground return smoothly.

C.11. Slope Estimation

The ability to estimate the slope of the surrounding hillsides with respect to the radar line-of-sight would be extremely useful for an autonomous vehicle trying to navigate through unfamiliar terrain.

A simple and yet effective method to achieve this was developed for the pulsed radar. It involved scanning the antenna in a small circle with a diameter of 3° centred on the section of hillside to be measured while tracking the surface to produce a sinusoidal variation in the measured range. The amplitude of this signal and its phase determine the magnitude and direction of the slope in that region. An example of the data produced for the test site is shown in Figure C.13.

In this example, the minimum and maximum ranges to the surface, as determined from the sinusoidal signal fitted to the data points, are r_1= 327m and r_2 = 370m respectively. From these and the included angle, $\alpha = 3°$, the cosine rule can be used to determine the distance between the two points on the surface,

$$a = \sqrt{r_1^{\ 2} + r_2^{\ 2} - 2r_1r_2\cos\alpha} \qquad \text{(C.13)}$$
$$= 46.7m.$$

The sine rule is then used to determine the approximate grazing angle, β,

$$\beta = Sin^{-1}\left(\frac{r_1\sin\alpha}{a}\right) + \frac{\alpha}{2} \qquad \text{(C.14)}$$
$$= 23^o.$$

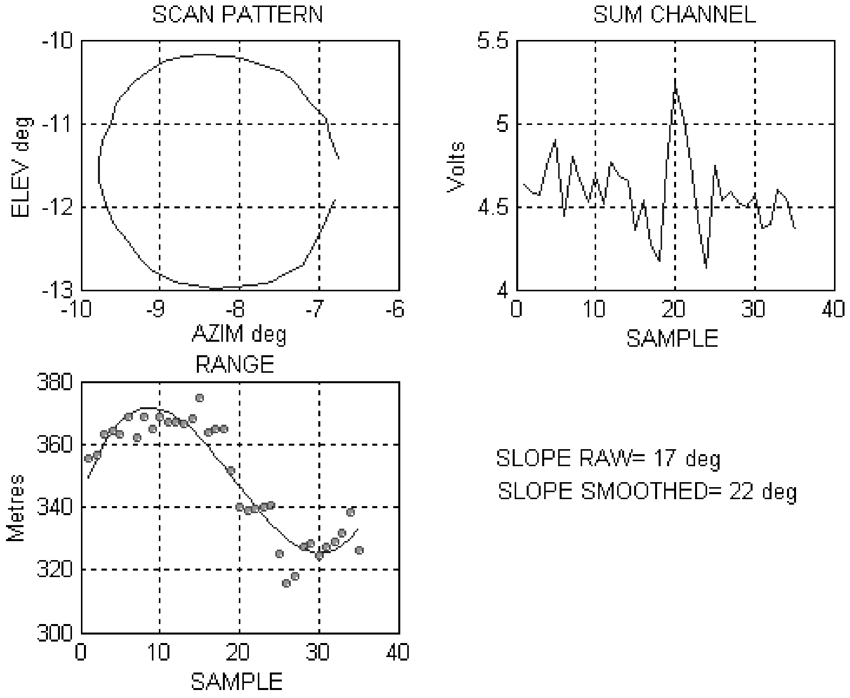

Figure C.13: Determining the slope of the terrain by conically scanning the pulsed millimetre-wave radar and measuring the range to the surface

The accuracy of this method was verified using ordnance survey maps of the same region. In this example, the angle was also measured using an inclinometer and was found to be about 23°, which is exactly the value determined in C.14 and within one degree of the smoothed estimate produced by the MATLAB script

Appendix D.

Effect of Chirp Linearity on the Range Resolution of an FMCW Radar

D.1. Introduction

A conventional FMCW radar shown in Figure D.1, operating at a centre frequency of 100GHz produces a 100MHz chirp in 1ms. It is used to show that the range resolution, δR, for a quadratic chirp-non-linearity is the product of the range, R, and the linearity, Lin,

$$\delta R = R.Lin\,. \tag{D.1}$$

The relationship between the beat frequency output and the other radar parameters can be expressed in the following form for linear chirp

$$\frac{\Delta f}{f_{beat}} = \frac{Tc}{2R}\,, \tag{D.2}$$

where Δf – Swept bandwidth (Hz)
f_{beat} – Beat frequency (Hz)
T – Sweep time (s)
c – Speed of light (m/s)
R – Range (m)

In this case the chirp is not linear and exhibits a quadratic slope nonlinearity with a maximum excursion from the linear of 1MHz/ms.

Chirp linearity is defined in terms of the chirp slope

$$Lin = \frac{S_{\max} - S_{\min}}{S_{\min}}\,, \tag{D.3}$$

where Lin – Radar chirp linearity
S_{max} – Maximum chirp slope (Hz/s)
S_{min} – Minimum chirp slope (Hz/s)

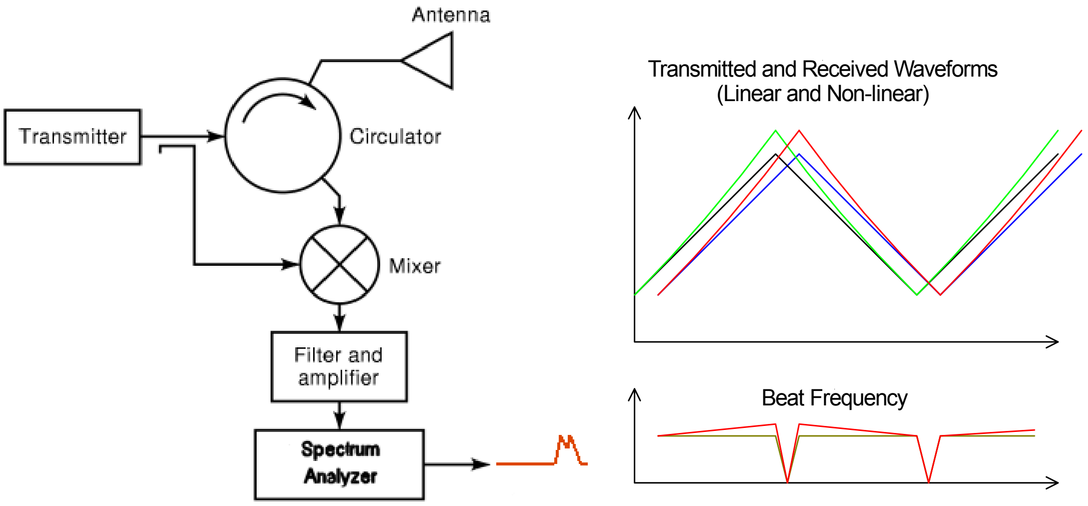

Figure D.1: FMCW radar block diagram and signals

D.2. Analytical Solution

Frequency modulation of a signal containing a linear and a quadratic modulation term can be written

$$\begin{aligned} v_{fm}(t) &= \cos\left[\omega_c t + A_b \int_{-\infty}^{t} t\,dt + B_b \int_{-\infty}^{t} t^2 dt\right]. \\ v_{fm}(t) &= \cos\left[\omega_c t + \frac{A_b}{2}t^2 + \frac{B_b}{3}t^3\right] \end{aligned} \tag{D.4}$$

This signal is transmitted and an echo is received τ seconds later

$$v_{fm}(t-\tau) = \cos\left[\omega_c(t-\tau) + \frac{A_b}{2}(t-\tau)^2 + \frac{B_b}{3}(t-\tau)^3\right]. \tag{D.5}$$

The mixer within the radar produces the product of these two terms

$$v_{fm}(t-\tau)v_{fm}(t) = \cos\left[\omega_c t + \frac{A_b}{2}t^2 + \frac{B_b}{3}t^3\right]\cos\left[\omega_c(t-\tau) + \frac{A_b}{2}(t-\tau)^2 + \frac{B_b}{3}(t-\tau)^3\right] \tag{D.6}$$

From the trig identity cos$A$.cos$B$ = 0.5[cos(A+B) + cos(A-B)] the individual sum and difference terms are determined.

D.2.1. Cos(A+B) Term from (D.6)

Expanding

$$\cos\left\{\begin{array}{l} \omega_c t+\frac{A_b}{2}t^2+\frac{B_b}{3}t^3+ \\ \omega_c t-\omega_c\tau+ \\ \frac{A_b}{2}\left[t^2+\tau^2-2\tau t\right]+ \\ \frac{B_b}{3}\left[t^3+\tau^2 t-2\tau t^2-\tau t^2-\tau^3+2\tau^2 t\right] \end{array}\right\}. \tag{D.7}$$

Gathering like terms from (D.7)

$$\cos\left\{\begin{array}{l} \omega_c t+\omega_c t-A_b\tau t+\frac{B_b\tau^2}{3}t+\frac{2B_b\tau^2}{3}t+ \\ \frac{A_b}{2}t^2+\frac{A_b}{2}t^2-\frac{2B_b\tau}{3}t^2-\frac{B_b\tau}{3}t^2+ \\ \frac{B_b}{3}t^3+\frac{B_b}{3}t^3+ \\ -\omega_c\tau+\frac{A_b\tau^2}{2}-\frac{B_b\tau^3}{3} \end{array}\right\}. \tag{D.8}$$

Simplifying (D.8)

$$\cos\left\{\begin{array}{l} \left[2\omega_c-A_b\tau+B_b\tau^2\right].t+ \\ \left[A_b-B_b\tau\right].t^2+ \\ \frac{2B_b}{3}t^3+ \\ -\omega_c\tau+\frac{A_b\tau^2}{2}-\frac{B_b\tau^3}{3} \end{array}\right\}. \tag{D.9}$$

D.2.2. Cos(A-B) Term from (D.6)

Expanding

$$\cos\left\{\begin{array}{l} \omega_c t+\frac{A_b}{2}t^2+\frac{B_b}{3}t^3+ \\ -\omega_c t+\omega_c\tau+ \\ -\frac{A_b}{2}\left[t^2+\tau^2-2\tau t\right]+ \\ -\frac{B_b}{3}\left[t^3+\tau^2 t-2\tau t^2-\tau t^2-\tau^3+2\tau^2 t\right] \end{array}\right\}. \tag{D.10}$$

Gathering like terms from (D.10)

$$\cos\left\{\begin{array}{l} \omega_c t-\omega_c t+A_b\tau t+\dfrac{B_b\tau^2}{3}t-\dfrac{2B_b\tau^2}{3}t+ \\ \dfrac{A_b}{2}t^2-\dfrac{A_b}{2}t^2+\dfrac{2B_b\tau}{3}t^2+\dfrac{B_b\tau}{3}t^2+ \\ \dfrac{B_b}{3}t^3-\dfrac{B_b}{3}t^3+ \\ \omega_c\tau-\dfrac{A_b\tau^2}{2}+\dfrac{B_b\tau^3}{3} \end{array}\right\}. \tag{D.11}$$

Simplifying (D.11)

$$\cos\left\{\begin{array}{l} \left[A_b\tau-B_b\tau^2\right]t+ \\ B_b\tau t^2+ \\ 0+ \\ \omega_c\tau-\dfrac{A_b\tau^2}{2}+\dfrac{B_b\tau^3}{3} \end{array}\right\}. \tag{D.12}$$

The final simplified equation combining (D.9) and (D.12)

$$\cos\left\{\begin{array}{l} \left[2\omega_c-A_b\tau+B_b\tau^2\right]t+ \\ \left[A_b-B_b\tau\right]t^2+ \\ \dfrac{2B_b}{3}t^3+ \\ -\omega_c\tau+\dfrac{A_b\tau^2}{2}-\dfrac{B_b\tau^3}{3} \end{array}\right\}+\cos\left\{\begin{array}{l} \left[A_b\tau-B_b\tau^2\right]t+ \\ B_b\tau t^2+ \\ \omega_c\tau-\dfrac{A_b\tau^2}{2}+\dfrac{B_b\tau^3}{3} \end{array}\right\}. \tag{D.13}$$

D.2.3. Values of some constants

For the given problem, the values of the various constants can be determined as follows:

$\omega_c = 2\pi f_c = 2\pi\times10^{11}$ rad/s for a frequency of 100GHz

$\tau = 2R/c = 2/3\times10^{-5}$ s for a range of 1km

For the linear frequency chirp term

$A_b t = \omega_b = 2\pi f_b$ for a total linear change in frequency after time T

$$A_b=\frac{2\pi f_b}{t}=\frac{2\pi\Delta f_L}{T}. \tag{D.14}$$

For $\Delta f_L = 100\times10^6$ and $T = 1\text{ms}$

$$A_b = \frac{2\pi\Delta f_L}{T} = \frac{2\pi\times100\times10^6}{10^{-3}} = 2\pi\times10^{11}.$$

The quadratic change in frequency term determines the change in the slope of the chirp signal.

The instantaneous value of this term is $B_b t^2 = \omega_{bq} = 2\pi f_{bq}$.

The derivative of this function, which is the non-linear portion of the chirp slope, equals Δf_Q at $t = T$ as defined,

$$\begin{aligned} \text{slope} &= \frac{df_{bq}}{dt} = \frac{d}{dt}\frac{B_b}{2\pi}t^2 = \frac{B_b}{\pi}t \\ \therefore B_b &= \frac{\pi.\text{slope}}{t} = \frac{\pi\Delta f_Q}{T} \end{aligned} \tag{D.15}$$

At $T = 1\text{ms}$ $\Delta f_Q = 1\text{MHz/ms} = 10^9$ Hz/s

$$B_b = \frac{\pi\Delta f_Q}{T} = \frac{\pi\times10^9}{10^{-3}} = \pi\times10^{12}.$$

D.2.4. Evaluation of the first cosine term (D.9) reproduced here

$$\cos\left\{\begin{array}{l} \left[2\omega_c - A_b\tau + B_b\tau^2\right]t + \\ \left[A_b - B_b\tau\right]t^2 + \\ \dfrac{2B_b}{3}t^3 + \\ -\omega_c\tau + \dfrac{A_b\tau^2}{2} - \dfrac{B_b\tau^3}{3} \end{array}\right\}. \tag{D.9}$$

The first cosine term (D.9) exhibits a linear frequency component at about twice the carrier frequency of ω_c, because the carrier frequency component is much larger than the other two constant frequency components as determined below.

$$2\omega_c = 4\pi\times10^{11}.$$

$$A_b\tau = 4\pi\times10^{11}\times\frac{2\times10^{-5}}{3} = \frac{8\pi\times10^6}{3}.$$

$$B_b\tau^2 = 3\pi\times10^{12}\times\left(\frac{2\times10^{-5}}{3}\right) = \frac{4\pi\times10^2}{3}.$$

The linear chirp term reaches a maximum value when $t = T = 10^{-3}$ s

$$\begin{aligned}(A_b - B_b\tau)T &= \left(4\pi\times10^{11} - 3\pi\times10^{12}\times\frac{2\times10^{-5}}{3}\right)\times10^{-3}\\ &\approx 4\pi\times10^{8}\end{aligned}$$

which is also much smaller than the constant frequency term and so can also be ignored.

Examination of the quadratic term shows that it is also much smaller than the constant frequency term and can also be ignored.

Finally, the last term shows the phase of the received signal and is not important in this analysis.

D.2.5. Evaluation of the second cosine term (D.12) reproduced here

$$\cos\left\{\begin{array}{l}\left[A_b\tau - B_b\tau^2\right]t + \\ B_b\tau t^2 + \\ \omega_c\tau - \dfrac{A_b\tau^2}{2} + \dfrac{B_b\tau^3}{3}\end{array}\right\}. \tag{D.12}$$

The second cosine term (D.12) consists of a constant frequency term which is a function of the round-trip time τ (and hence the range). Unlike the linear FM case the function includes both linear and quadratic terms. However, the quadratic term is very small and can be ignored.

In addition to this constant frequency term, there is a phase term which is not important and a linear chirp term which is also proportional to the round-trip time and determines how much the echo spectrum is spread.

This leaves the following simplified equation defining the received beat frequency

$$\cos\left(A_b\tau.t + B_b\tau.t^2\right). \tag{D.16}$$

Substituting for A_b (D.14) and B_b (D.15) determined earlier

$$\cos\left(\frac{2\pi\Delta f_L\tau}{T}t + \frac{\pi\Delta f_Q\tau}{T}t^2\right). \tag{D.17}$$

This is the standard FM modulation representation, so the instantaneous frequency can be obtained by differentiating the phase terms

$$\begin{aligned} f_{inst} &= \frac{1}{2\pi}\frac{d}{dt}\left(\frac{2\pi\Delta f_L\tau}{T}t+\frac{\pi\Delta f_Q\tau}{T}t^2\right) \\ f_{inst} &= \frac{\Delta f_L\tau}{T}+\frac{\Delta f_Q\tau}{T}t \end{aligned} \tag{D.18}$$

This equation shows that there is a constant beat frequency term that is proportional to the round-trip time, τ, and a linear chirp term the magnitude of which is also proportional to τ.

The linearity of a FMCW radar is defined as the change in slope of the frequency chirp divided by the minimum slope, which is equal to the change in beat frequency divided by the minimum beat frequency

$$Lin = \frac{\Delta slope}{slope} = \frac{\Delta f_{beat}}{f_{beat}}. \tag{D.19}$$

Substituting the two terms from the expression for the instantaneous frequency

$$Lin = \frac{\Delta f_Q\tau}{T}t.\frac{T}{\Delta f_L\tau} = \frac{\Delta f_Q}{\Delta f_L}t. \tag{D.20}$$

The worst case nonlinearity occurs at the end of the sweep where $t = T$

$$Lin_{\max} = \frac{\Delta f_Q T}{\Delta f_L}. \tag{D.21}$$

The standard formula that determines the beat frequency of a FMCW radar as a function of the other parameters as described in the problem statement

$$\frac{\Delta f_{tot}}{f_{beat}} = \frac{Tc}{2R}, \tag{D.1}$$

can be used to determine the range

$$R = \frac{Tcf_{beat}}{2\Delta f_{tot}}. \tag{D.22}$$

Assuming that the non-linear term is small so $\Delta f_{tot} \approx \Delta f_L \approx \Delta f$, then the measured range can be determined from the static portion of the instantaneous frequency

$$\bar{f}_{beat} = \frac{\Delta f_L\tau}{T}. \tag{D.23}$$

Substituting into the equation for range

$$R = \frac{Tc}{2\Delta f} . \frac{\Delta f \tau}{T} = \frac{c\tau}{2} . \tag{D.24}$$

The range resolution due to the non linear chirp can be expressed in terms of the spread in the beat frequency

$$\delta R = \frac{Tc\delta f_{beat}}{2\Delta f_{tot}} . \tag{D.25}$$

In this case the range resolution is determined from the change in beat frequency which is the chirp portion of the instantaneous frequency

$$\delta f_{beat} = \frac{\Delta f_Q \tau}{T} t , \tag{D.26}$$

which will be at its worst at $t = T$

$$\delta f_{beat} = \Delta f_Q \tau . \tag{D.27}$$

Substituting in the equation for the range resolution and grouping. The expression can be rewritten as

$$\begin{aligned} \delta R &= \frac{Tc\Delta f_Q \tau}{2\Delta f_{tot}} \approx \frac{\Delta f_Q T}{\Delta f_L} . \frac{c\tau}{2} \\ \delta R &= Lin.R \end{aligned} \tag{D.28}$$

Appendix E.

Improving the Chirp Linearity of an FMCW Radar

The effect of chirp non-linearity is shown conceptually in Figure E.1. In this illustration there is an abrupt change in slope that results in the production of two distinct beat frequencies for the same target. In general however, the change in slope is more gradual making the spread in beat frequencies more uniform.

In a more formal sense, if the chirp is not linear, the standard matched filter assumptions for resolution are not satisfied and the range resolution will suffer.

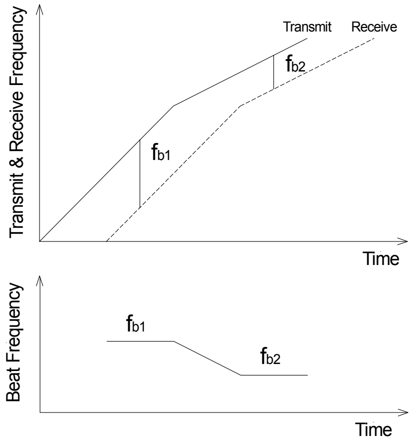

Figure E.1: Conceptual diagram showing the effect of chirp non-linearity on the beat frequency output of an FMCW radar

It was shown in Appendix D that if the nonlinearity is quadratic, then the range resolution degrades linearly with range as defined

$$\delta R = R.Lin\,, \tag{E.1}$$

where the linearity, *Lin,* is defined as the change in chirp slope $S = df/dt$ normalised by the minimum slope,

$$Lin = \frac{S_{\max} - S_{\min}}{S_{\min}}\,. \tag{E.2}$$

This sensitivity to slope linearity is one of the fundamental problems that limits the resolution of real FMCW radar systems. Techniques to circumvent this limitation are addressed in the following sections of this appendix.

E.1. Open-loop Techniques

Most short-range millimetre-wave radar systems use voltage-controlled oscillators (VCOs) to generate the chirp signal. These generally comprise a reduced-height waveguide, housing a Gunn diode and a hyper-abrupt varactor diode in series with a radial disc resonator inserted between them, as discussed at length in [153].

Typical measured results for this configuration show an extremely non-linear tuning characteristic, if bandwidths in excess of 100MHz are required, as can be seen in Figure E.2.

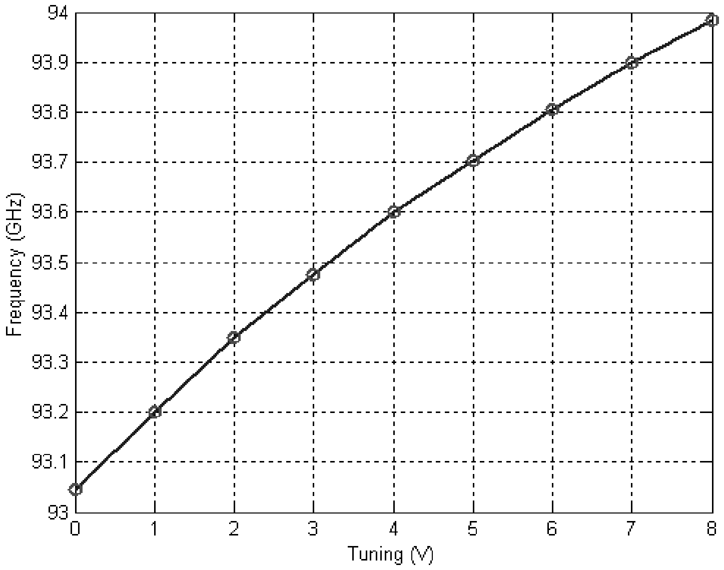

Figure E.2: Measured tuning characteristic of a typical millimetre-wave Gunn VCO

The depicted oscillator non-linearity is almost entirely quadratic in nature with a linearity of 0.49 over the full operational band. This translates into a range resolution of 49m at 100m if the complete bandwidth is utilised. This is clearly unsatisfactory for most applications.

One obvious solution is to apply a correction to the tuning voltage to compensate for this nonlinearity as determined by the construction in Figure E.3.

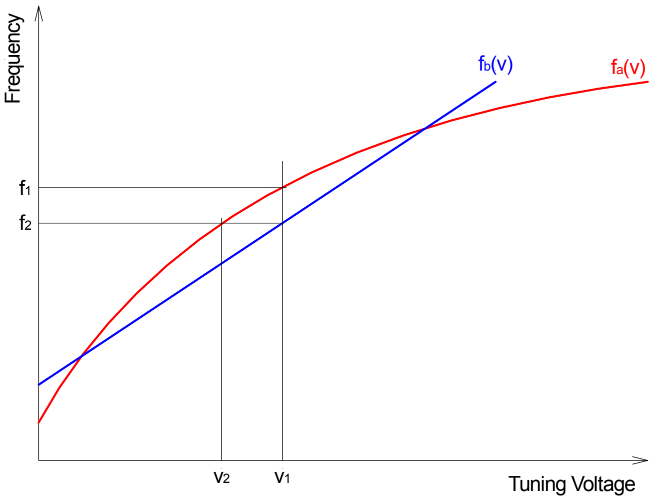

Figure E.3: Geometric construction to illustrate the process of open-loop linearization correction achieved by mapping from the nonlinear function *fa*(*v*) to the linear function *fb*(*v*)

For a nonlinear function $f_a(v)$ shown in Figure E.3, a tuning voltage v_1, results in an output frequency f_1. However to map onto the linear function $f_b(v)$ requires that the frequency be f_2 at that point which corresponds to a voltage v_2. This transformation can be accomplished analytically by fitting polynomials to the two functions and then solving for v_2 in terms of the coefficients and v_1. A second order polynomial requires the solution of a quadratic equation the results of which are shown in Figure E.4.

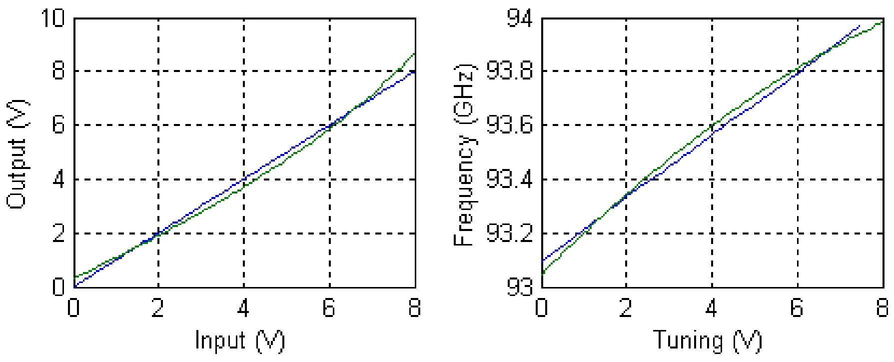

(a) (b)

Figure E.4: Open-loop linearization results showing (a) nonlinear tuning voltage compared to its linear counterpart and (b) unaltered and linearised output frequency

In this example, in which only the quadratic error is corrected, the measured slope linearity has been reduced to 0.0016. This is exceptional, and seldom if ever occurs because, in practice, VCO nonlinearities are usually not so well behaved.

A number of different techniques have been developed to implement this linearization process, of which the most simple was developed by Philips Microwave [187]. In this technique the ramp signal is integrated with respect to time to produce a quadratic signal correction which is added to the ramp. Another technique [30] implemented the quadratic correction using an analog multiplier integrated circuit. The most common method in use today involves measuring the nonlinearity and then programming the correction in a lookup table (EPROM) that is clocked into a digital-to-analog converter (DAC) and output to the VCO.

These techniques can improve the linearity of a typical VCO to about 0.05 which translates into a range resolution of 5m at a range of 100m which is adequate for many applications. However, as the oscillator ages or the temperature changes, the linearity degrades in an unpredictable manner.

E.2. Closed-loop Techniques

This open-loop linearization technique is often augmented by a correction loop which can improve the ultimate linearity by a further factor of 50 to better than 0.001 (10cm at 100m). The core of this technique is the delay line discriminator [44] first developed as part of the ALCOR[2] radar signal generation suite [51]. This process was developed further for both microwave [54], [52], [29] and millimetre-wave applications. As shown in Figure E.5, the delay-line discriminator mixes the chirp output with a delayed version of the same signal to produce a beat signal in a similar manner to that generated by an FMCW radar. If the chirp is perfectly linear, then a constant frequency beat will be produced, but changes in the slope manifest themselves as variations in the frequency. A phase detector compares this beat frequency to a reference frequency, and the resulting phase error is then filtered and added to the tuning voltage to correct for error as in a standard phase-locked-loop [89]. In this configuration, because the delay-line discriminator produces the derivative of the chirp frequency, the loop filter must include an integrator to produce the proper corrections.

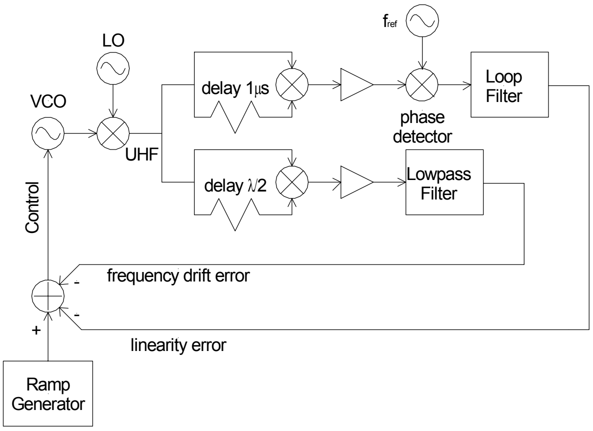

Figure E.5: Schematic block diagram of the closed-loop chirp linearization technique showing both centre frequency control and slope linearization loops

A great deal of work has been done in designing the appropriate loop filter to produce the most linear sweep, but few of them address one of the fundamental shortcomings of this loop structure which is that it is only the sweep slope which is controlled and not the centre frequency. In theory, this should not have much effect, but because the bandwidths of some of the components (particularly commercially available SAW

---

[2] ALCOR is a C-band radar on the Kwajalein Atoll in the Pacific.

delay lines) are narrow, even a small drift in the centre frequency can result in significant decreases in the signal level and loss of lock over part or all of the sweep. An additional frequency discriminator followed by a filter with a time constant of a couple of seconds combats the long-term frequency drift to keep the centre frequency within tight limits [32].

If tight control of oscillator characteristics can be maintained by using similar oscillator configurations for the VCO and LO, and by attaching them to a common substrate to maintain identical temperatures, as is done in implementations by Philips Microwave [21] and Farran Technology, amongst others, then the additional loop is not required. However in cases where a low-frequency LO is used along with a harmonic mixer, then the loop is required.

The selection of delay line depends on the required chirp bandwidth and the size of the radar. For compact applications, a SAW delay line is the component of choice. However it is limited in bandwidth to about 300MHz at a centre frequency of 700MHz. For wider bandwidth operation, a higher frequency UHF signal can be divided down to the 700MHz centre frequency. For example, a divide-by-two circuit operating on a 1.4GHz UHF signal accommodates a 600MHz chirp [57], [43]. New processes [162] have produced laboratory samples of SAW delay-lines operating with bandwidths of up to 800MHz at a centre frequency of 2.45GHz which could be used without division.

Broader band delay-lines that have been implemented in less constrained circumstances include fibre-optic or coaxial and even free-space types [99]. The latter uses the return from a trihedral reflector at a known range to produce the appropriate reference for linearisation.

Because the delay line discriminator output as shown in Figure E.6 is equivalent to that from the actual FMCW radar at a range equivalent to the round-trip time through the delay line, its output spectrum is the template for all of the target spectra that are obtained by the radar. If the linearization loop is locking and this spectrum is well defined and sharp, then the target returns will be similarly sharp, but if the loop is not locking and the spectrum is broad, then the target returns will be broad, and the range resolution will be poor. Residual non-linearities will still result in increasingly wide spectral returns with increasing range.

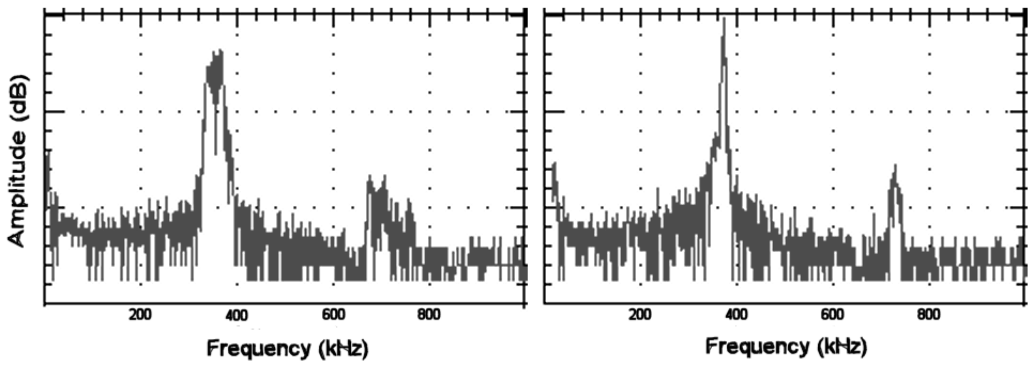

(a) (b)

Figure E.6: Measured delay-line discriminator output spectra (a) unlinearised chirp and (b) linearised chirp

E.3. Other Methods

Another common method to improve the linearity is to use an oscillator that is inherently more linear than the standard Gunn VCO. Examples of these oscillators include YIG tuned oscillators [132], and transistor-based VCOs. The use of a transistor-based VCO operating at low frequency which is then multiplied up into the millimetre-wave band is described in [38]. More recently, the use of direct digital synthesis (DDS) to generate perfectly linear chirp signals has become practical at clock rates of 1GHz. This option requires that the signal be upconverted to the appropriate band which adds significantly to the cost of the radar.

A final method that has become popular in the last few years since the advent of sophisticated synthesizer integrated circuits is the use of a phase-locked loop to generate the chirp in a piecewise fashion. Because this technique could only generate fairly coarse frequency steps at the reference frequency, the spectra generated suffered reduced resolution and higher sidelobe levels. However the use of a fractional divider [145] allows the generation of many more points per sweep (>50,000) and produces a chirp with a slope linearity of 10^{-4}.

E.4. Linearisation, Chirp Bandwidth and Spectral Width

If the open-loop case is considered, it is obvious that as the chirp bandwidth is increased the range resolution will improve, but also as the chirp bandwidth increases, the total non-linearity increases and the range resolution degrades simultaneously as described

$$\delta R = \sqrt{\left(\frac{c}{2\Delta f}\right)^2 + (R.Lin)^2}\ . \tag{E.3}$$

It can easily be shown that an optimum bandwidth can be determined for every operational range.

For the VCO tuning characteristics plotted in Figure E.2 and for a specific region of operation around 6V at a range of 500m. Figure E.7 shows the effects of the bandwidth and linearity on the overall range resolution as a function of the chirp bandwidth utilised.

Probably the most interesting conclusion that can be drawn from this graph is that more is not always better, and in this case the chirp bandwidth should be kept quite small, only about 15MHz, to produce the best resolution.

Obviously, it is not always possible to adjust the bandwidth to obtain an optimum resolution dynamically, nor is it practical to do so if the radar is used for imaging and targets of interest span a large range. However, if the radar were to be operated against a point target at a known range, then it would be practical to adjust the ramp voltage to obtain the best range resolution possible.

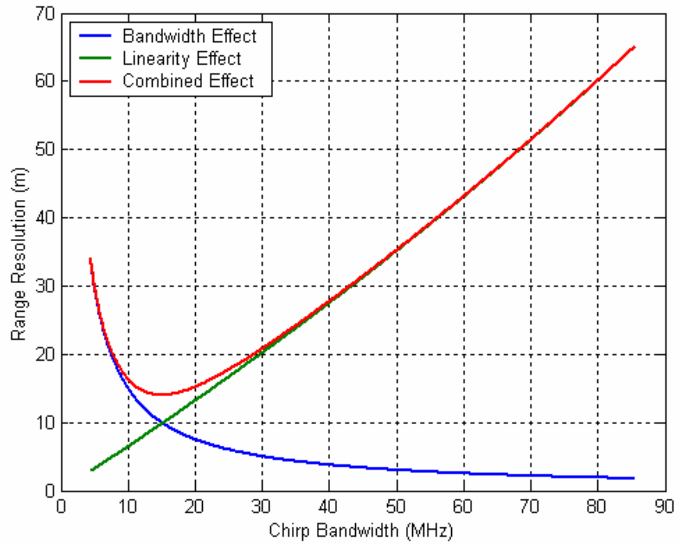

Figure E.7: Effect of optimising the chirp bandwidth on the range resolution of a non linearised FMCW radar illuminating a target at 500m shows that the best performance is obtained for a bandwidth of about 15MHz

Considering the closed-loop case where the linearity is much better than that provided in the non-linearised case and is not necessarily quadratic in nature, then it is no longer practical to try to optimise the bandwidth. In this case the resolution degrades with range in a predictable way as shown in Figure E.8 which is generated for a radar with a chirp, Δf = 600MHz and a closed-loop linearity of Lin = 0.001.

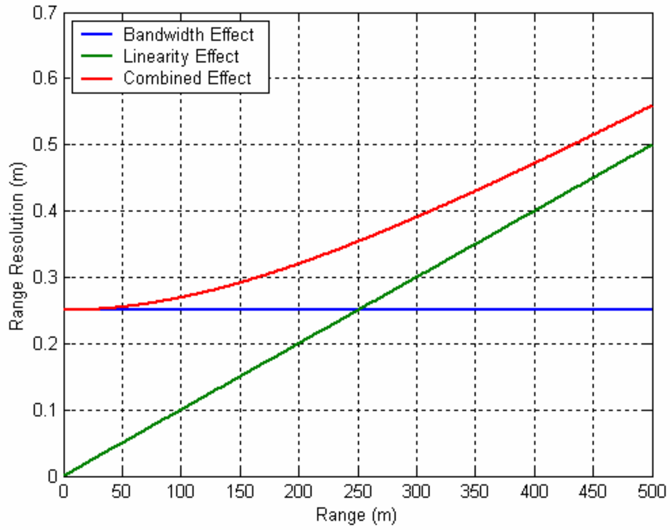

Figure E.8: Range resolution of an FMCW radar as a function of range showing the contributions of the chirp bandwidth and linearity

In this example it can be seen that the resolution is determined primarily by the bandwidth at ranges of less than 250m, and by the chirp linearity beyond that. For a closed-loop linearised radar, it is often difficult to determine the chirp linearity in any way other than by measurement, and it can be seen that this is only possible at long range where these effects dominate.

Appendix F.

Improving the Imaging Performance of an FMCW Radar

F.1. Reducing Range Sidelobes

The spectrum of a truncated sine wave output by an FMCW radar for a single target, has the characteristic $|\sin(x)/x|$ shape determined by the matched ambiguity-function $\chi_o(t_d, 0)$ for the FMCW radar with zero Doppler.

The range sidelobes in this case are only 13.2dB lower than the main lobe which is not satisfactory as it can result in the occlusion of small nearby targets as well as introducing clutter from the adjacent lobes into the main lobe. To counter this unacceptable characteristic of the matched filter, the time domain signal is deliberately mismatched. This mismatch generally takes the form of amplitude weighting of the received signal.

The reduction in sidelobe levels comes at a price. The main-lobe amplitude is marginally reduced and is also widened quite substantially as seen in Table F.1.

Table F.1: Properties of some weighting functions

Window	**Rectangle**	**Hamming**	**Hanning**	**Blackman**
Worst Sidelobe (dB)	-13.2	-42.8	-31.4	-58
3dB Beamwidth (bins)	0.88	1.32	1.48	1.68
Scalloping Loss (dB)	3.92	1.78	1.36	1.1
SNR Loss (dB)	0	1.34	1.76	2.37
Main-lobe Width (bins)	2	4	4	6
a_0	1	0.54	0.50	0.42
a_1		0.46	0.50	0.50
a_2				0.08
$W(n)=a_0-a_1\cos[2\pi(n-1)/(N-1)]+a_2\cos[4\pi(n-1)/(N-1)]$				

One method of achieving this weighting is to increase the FM slope of the chirp pulse near the ends of the transmitted pulse to weight the power spectrum. This will result in the desired low sidelobe levels after the application of the matched filter. This is easy to achieve in SAW based systems. A more conventional method, often used in digital systems, is to apply the function to the signal amplitude prior to processing.

The rectangular, or uniform, weighting function provides a matched filter operation with no loss in SNR, while the weighting in the other cases introduces a tailored mismatch in the receiver amplitude characteristics with an associated loss in SNR which can be quite substantial as listed in Table F.1.

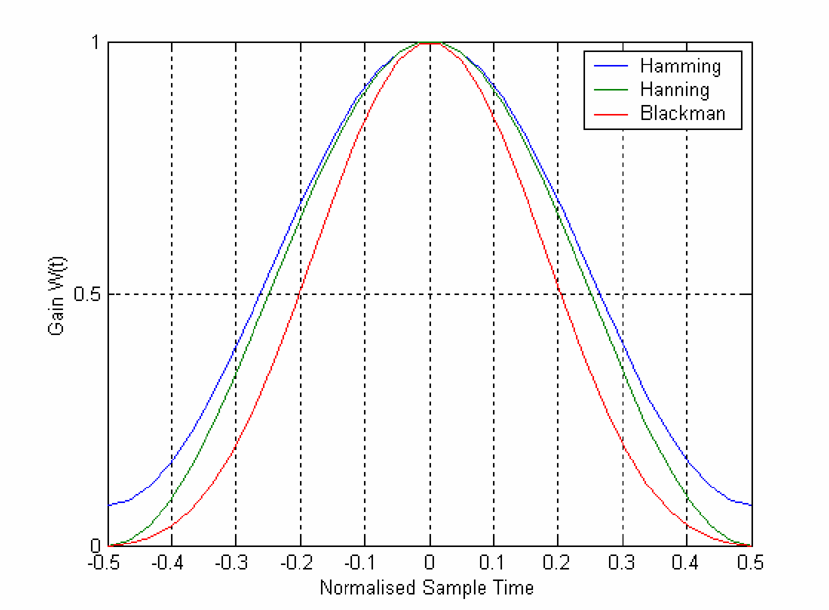

Figure F.1: Gains for a number of common weighting functions

Uniform weighting also provides the best range resolution (narrowest bandwidth), but this characteristic comes with unacceptably high sidelobe levels. The other weighting functions offer poorer resolution but improved sidelobe levels with falloff characteristics that can accommodate almost any requirement as seen in Figure F.2.

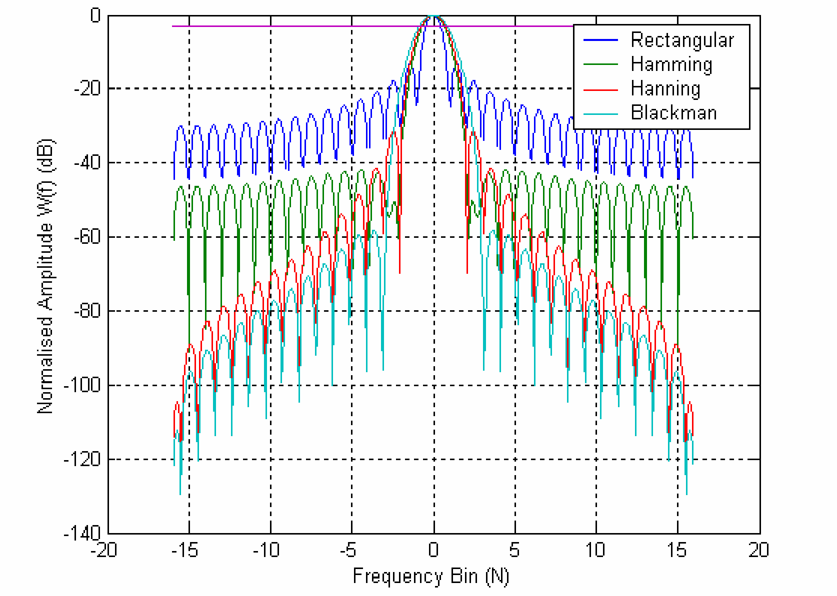

Figure F.2: Normalised amplitude spectra for finite-duration constant-frequency signals weighted by different weighting functions showing the differences in the peak spectral width (range resolution) and the sidelobe levels

Of particular interest are the Hamming and Hanning weighting functions which offer similar loss in SNR and resolutions, but with completely different sidelobe characteristics. As can be seen in Figure F.2, the former has the form of a cosine-squared-plus-pedestal, while the latter is just a standard cosine-squared function. In the Hamming case, the close-in sidelobe is suppressed to produce a maximum level of -42.8dB but that energy is spread into the remaining sidelobes resulting in a falloff of only 6dB/octave, while in the Hanning case, the first sidelobe is higher, -31.4dB, but with a falloff of 18dB/octave.

For most FMCW applications, the Hamming window is used as it provides a good balance between sidelobe levels (-42.8dB), bandwidth (1.32 bins) and loss in SNR compared to a matched filter (1.34dB). For imaging applications, where a large dynamic-range of target reflectivities is expected, then the Hanning window with its superior far-out sidelobe performance is the function of choice.

F.2. Phase Noise, Mixing and Common Aperture Problems

Most applications cannot afford the luxury of using separate transmit and receive antennas, and instead combine the two functions into a single antenna. However, this compromise should not be undertaken without due consideration to its ramifications on the overall performance of the FMCW system.

A single antenna, or indeed, a dual antenna configuration mounted behind a radome results in a significant portion of the transmitter power leaking into the receiver. This is not a problem for a pulsed radar that separates its transmit and receive functions in time, but it does pose significant problems for an FMCW system that must receive echoes while it is transmitting. These problems include a limit to the maximum transmit power and a requirement for careful matching of the antenna to minimise the magnitude of reflections back into the receiver.

For short-range operation, the FMCW radar may transmit a signal power up to about 50mW (17dBm) while simultaneously receiving signals smaller than -80dBm, a difference of about 100dB. The best Y-junction circulators seldom offer isolations much better than 20dB, for leakage path L_1 shown in Figure F.3, and the return loss of a good antenna seldom exceeds -25dB for leakage path L_2. In addition, if there is also a radome, leakage path L_3 is likely to be of the same order of magnitude as L_2, so at best the leakage signal will be some 80dB higher than the received signal.

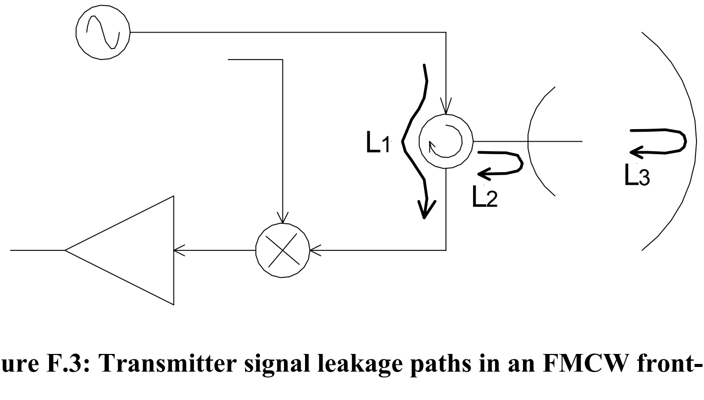

Figure F.3: Transmitter signal leakage paths in an FMCW front-end

Because the direct path and the leakage paths are about the same length, the frequency of the signal that reaches the mixer by the two routes will be the same, and so it will operate as a phase detector with an output voltage proportional to the product of the two input powers multiplied by the sine of the phase difference

$$v(t) \approx \frac{A_c A_r}{2} \sin \frac{2\pi \Delta R}{\lambda}, \tag{F.1}$$

where A_c and A_r are the direct and leakage path signal amplitudes (V) and ΔR is the path length difference (m).

The sine term is used here instead of the cosine term because most balanced mixers use a hybrid to couple the signals onto the diodes and a phase shift of $\pi/2$ exists between the RF and LO ports. It can be seen from (F.1) that the output voltage will be a function of both the RF signal amplitude and the path-length difference.

The non-linear I-V characteristic of a semiconductor diode that is required for mixing is valid only over a small section of the I-V curve [135]. Therefore, if the leakage signal, A_r is too large, it can bias the mixer out of this region into saturation and degraded performance results. This does not occur if the path lengths are matched making $\Delta R = 0$, in which case the output bias voltage $v(t)$ is zero and the mixer performs normally for AC signals.

In addition to this desensitisation effect which is well documented [154], the leakage signal also introduces additional noise into the receiver over and above the standard thermal-noise level. This additional noise is due to the phase-noise of the transmitter which widens the spectrum in a predictable fashion as shown schematically in Figure F.4.

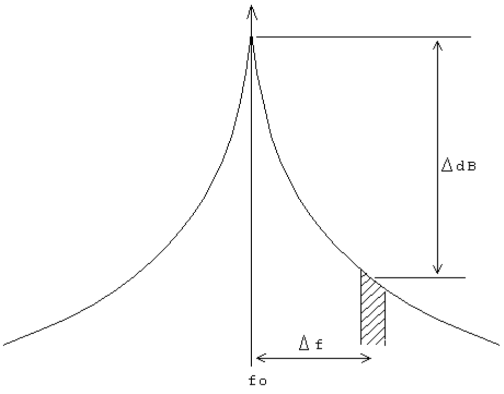

Figure F.4: Characteristic phase-noise spectrum out of an oscillator showing the relationship between the SSB noise spectral density and the offset from the carrier

The phase-noise produced by a number of 94GHz VCOs has been measured and this varies between -69 and -74dBc/Hz at an offset of 100kHz from the carrier. The power spectrum $S(f)$ for a Millitech oscillator was measured to be

$$S(f) = 10^{7.85} f^{-3.05}. \tag{F.2}$$

If the phase-noise contributions are included in the equations derived for the FMCW beat signal, then the equations can be rewritten as

$$v_{out}(t) = \frac{A_c^2}{2}\cos\left[A_b T_p + \left(\omega_c T_p - \frac{A_b}{2}T_p^2\right) + \phi(t) - \phi(t - T_p)\right]. \tag{F.3}$$

The transfer function describing the frequency difference of a signal and its copy is

$$H(j\omega) = 1 - \exp\left(-j\omega T_p\right), \tag{F.4}$$

Making the magnitude squared function

$$\left|H(j\omega)\right|^2 = 2\left(1 - \cos\omega T_p\right). \tag{F.5}$$

The output power spectral density for a phase-noise input of *S*(*f*) is just the product of this transfer function and the noise power spectrum

$$S_r(f) = 2S(f).\left(1 - \cos 2\pi f T_p\right), \tag{F.6}$$

so the noise power relative to the carrier at an offset Δf from the carrier in dB/Hz is just

$$N(\Delta f) = 10\log_{10} 2S(\Delta f).\left(1 - \cos 2\pi\Delta f T_p\right). \tag{F.7}$$

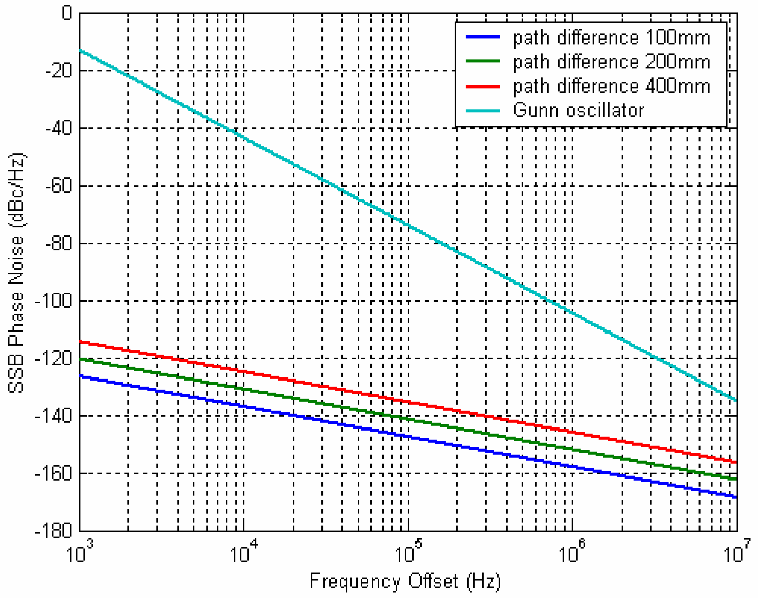

Figure F.5: Phase-noise levels at the FMCW radar mixer output due to leakage with path length differences as a parameter

In the leakage case, the round-trip time is replaced by its equivalent path-length difference, $T_p = \Delta R/c$, and the modified phase-noise spectrum plotted. It should be remembered that the velocity of the electromagnetic radiation in a waveguide is lower than that in free space, and this difference should be taken into account.

Figure F.5 displays the phase-noise as a function of frequency in dB relative to the transmitter power level (dBi) and does not consider the actual power, nor the actual leakage level. Hence if the transmitter power is P_t dBm and the leakage is L_{leak}, then the power levels displayed must be scaled by P_t - L_{leak} to obtain the actual noise power density.

To obtain the actual noise power output by each range gate, the noise power density must be integrated over the gate bandwidth, so for a typical FMCW radar that transmits a power P_t = 15dBm with a moderately low leakage level of L_{leak} = -20dB and a range-gate bandwidth β = 1kHz, then the noise power levels must be increased by $15 - 20 + 10\log_{10}(10^3) = 25$dB.

The magnitude of this phase-noise signal in comparison to the thermal noise power levels is significant at short range as shown in Figure F.6.

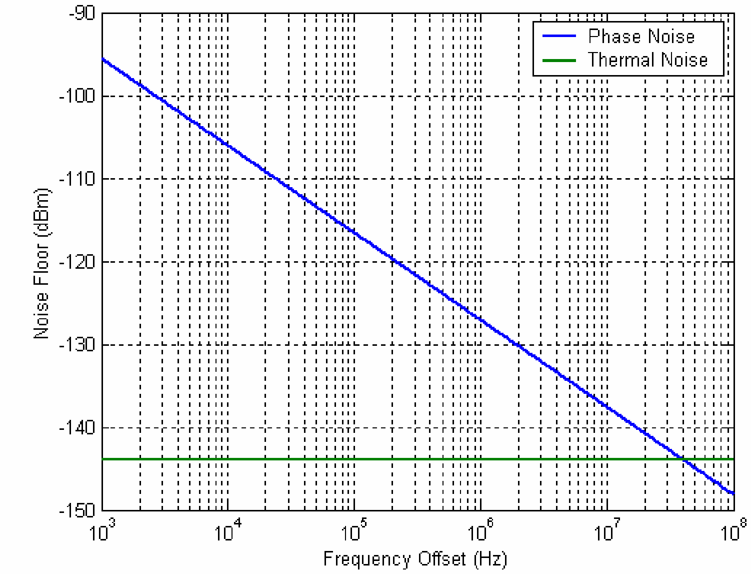

Figure F.6: Comparison between phase-noise and thermal noise at the mixer output of a typical FMCW radar

From this graph it is quite clear that the radar performance is limited by oscillator phase-noise right up to 40MHz, and that increasing the transmitter power will just raise the noise floor proportionally and no improvement in performance would be obtained.

The only way to improve the performance of the standard homodyne configuration described is to decrease the magnitude of the leakage signal by using superior components with low VSWRs or low leakage, to reduce the transmitted power, or to use an oscillator that has superior phase-noise characteristics [31].

To overcome this problem, alternative heterodyne configurations that use much higher beat frequencies can be implemented at a cost. However, to address the problem directly, techniques are available to inject a portion of the transmitter signal into the mixer in antiphase to cancel some of the leakage power [116]. A more effective option is to monitor the leakage-power amplitude and phase in real time and inject an antiphase signal into the receive path just prior to the mixer to cancel the leakage signal. The latter approach has been introduced with good effect [19] at X-band where improvements of up to 40dB are obtained over a 650MHz bandwidth This technique has been demonstrated at W-band [114] though the vector-modulator components are not readily available.

F.3. Phase Noise around the Target and Image Contrast

The phase-noise fringes also appear around any received target as shown in Figure F.7, and if it is large, leak into the adjacent range bins. This results in a blurring of edges in a radar image and can even result in smaller targets being completely swamped.

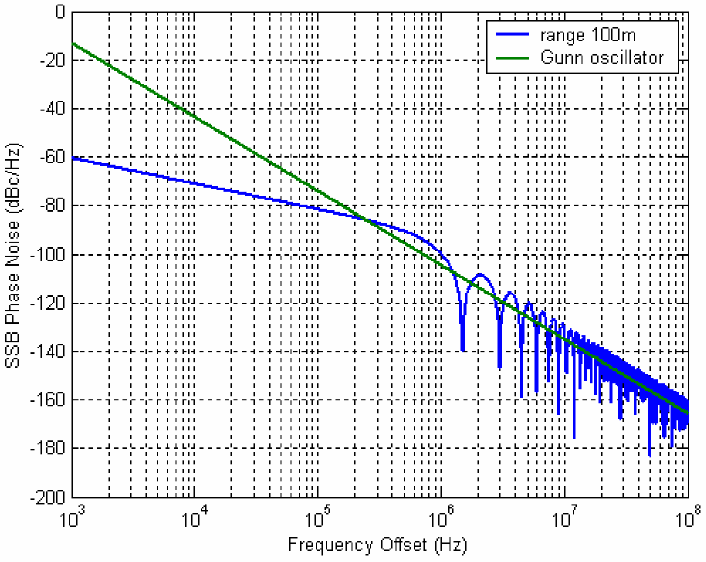

Figure F.7: Phase-noise around a target return at a range of 100m compared to the phase-noise from a standard W-band Gunn oscillator

To determine the noise levels in the adjacent range gates, this noise is integrated over the gate bandwidth at the appropriate offsets as shown in Figure F.8.

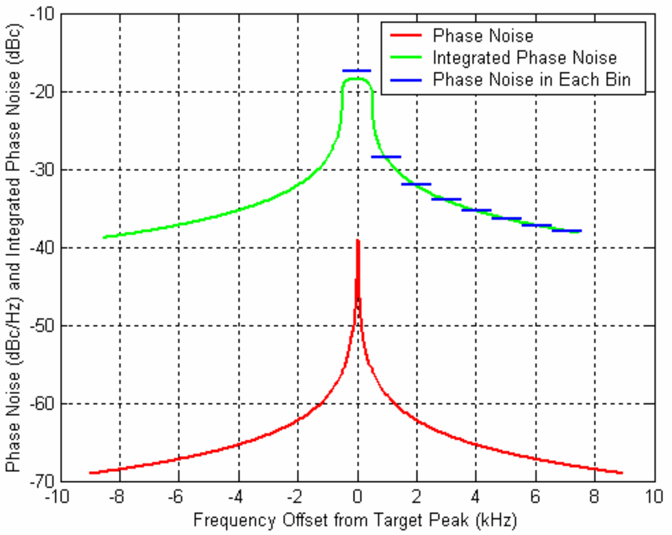

Figure F.8: Phase-noise and integrated phase-noise in each 1kHz wide range-bin around a target at a range of 100m

This figure shows the integrated phase-noise power with respect to the reflected signal level in each of the range bins adjacent to the peak echo signal. In this example with a 1kHz range-gate bandwidth, the integrated phase-noise level in the bins straddling the target is less than 29dB down on the peak signal level. In addition, the level drops off more and more slowly, so even by the 7th bin, the noise level is only 38dB down.

This characteristic ensures that there can never be a contrast of more than 29dB across a range-gate boundary irrespective of the actual differences in RCS for this particular configuration and at this range. It also means that the returns from smaller targets adjacent to a large target will often not be detectable.

If the target is sufficiently large, then these phase-noise skirts can rise above the noise floor and produce bright radial lines on images made using FMCW radars as is shown in Figure F.9.

In this case, the nearby hangars, (at a range of about 400m) towards the top of the image, have sufficiently large radar cross sections to lift the noise floor higher than the target echoes along that radial.

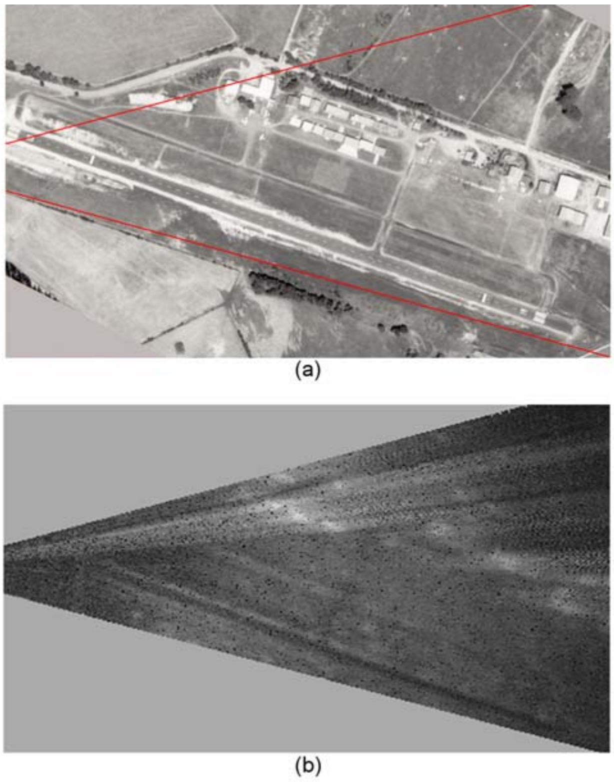

Figure F.9: Aerial photograph (a) and range-gate limited radar image showing the bright radial lines generated by the phase-noise signal around large RCS targets

From a navigation perspective, such artefacts would make the interpretation of any image being processed, much more complex, and because actual features might be lost, less effective. For example, had there been an ILS antenna with a large RCS at the end of the runway then its phase-noise radial could completely obliterate the negative-contrast runway return.

F.4. AM Noise

The AM noise spectral density from a Gunn VCO is typically -125dBc/kHz [11]. For a 15dBm oscillator power and after the 20dB attenuation around the leakage path, the noise level at the mixer has reduced to -125 + 15 - 20 = -130dBm.

One final source of AM noise is through the direct path to the LO input of the mixer. Assuming an externally biased mixer (typical of most FMCW systems), with a drive level of 3dBm and an AM leakage suppression through the balanced mixer of 35dB, the noise contribution will be -125 + 3 - 35 = -157dBm. This is much smaller than the AM noise signal via the leakage path and can be ignored in this instance.

The total AM-noise contribution is 14dB higher than the thermal-noise level calculated earlier in this appendix, and so becomes one of the main limiting factors to the performance of an FMCW radar. Increasing the transmitter power just increases the noise level which negates any increase in the detection range so, once again, the only method to improve the performance is to increase the isolation between the transmitter and the receiver.

Improving the isolation between transmitter and receiver can be achieved by using superior components such as circulators with particularly good isolation and antennas with good VSWR, but these are often not available. An alternative which is often impractical is to use separate transmit and receive antennas, or to use the interrupted FMCW technique.

F.5. Signal Processing Effects

The beat frequency output by an FMCW radar encodes the target range information as a frequency component with an amplitude proportional to the radar cross-section. If only a single target is illuminated, then a single beat frequency is returned, and if the SNR is sufficiently high, the range can be obtained using a counter. However if the beam illuminates a number of targets at different ranges, then the beat signal contains all of these returns and spectrum analysis is required to extract the individual range and amplitude information.

The classical spectrum analyser operates by sweeping a bandpass filter through the frequency range of the beat signal or by using banks of bandpass filters [175]. However, considerable simplification is possible by digitising the signal and applying an FFT.

The radar signal is first amplified and then filtered by a high pass filter to remove the DC and low frequency components (and thus decreasing the magnitude of the quantisation error). It is then lowpass filtered to limit the maximum signal-frequency to conform to the Nyquist conditions before being sampled and digitised. Finally the signal is weighted by one of the windows discussed earlier before the frequency spectrum is obtained using a conventional FFT algorithm.

If the bandwidth of interest exceeds the available sample rate from the ADC, then it is possible to divide the received signal into smaller bands and downconvert each sequentially prior to digitisation. This procedure is discussed in detail in Chapter 5.

F.5.1. Signal Quantisation and Noise

If the quantisation level Q is the smallest change in signal level that can be represented digitally and the analog signal $s(n)$ is rounded to produce a digital representation $s_Q(n)$, then the relationship between $s(n)$ and $s_Q(n)$ is shown in Figure F.10 [158]:

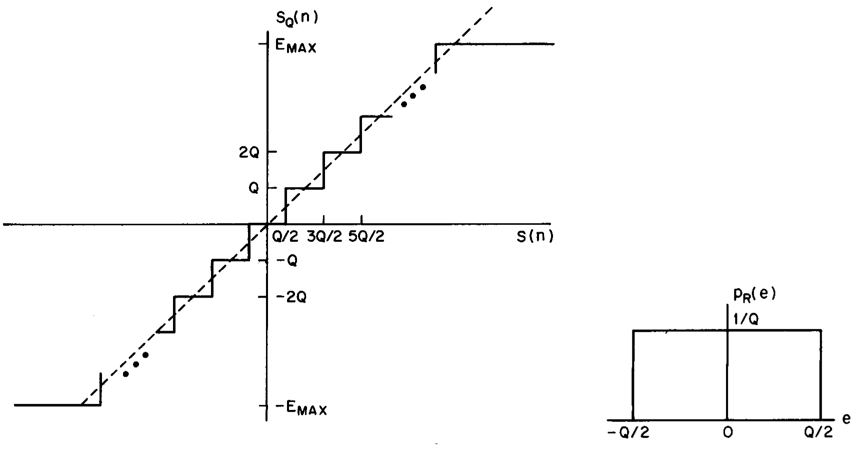

(a) (b)

Figure F.10: Quantiser (a) characteristic with rounding (b) probability distribution

If the signal level is constrained to be within E_{MAX} and $-E_{MAX}$ then it is clear from the figure that the magnitude of the error signal never exceeds $Q/2$, and the distribution of the error signal will be uniform with a variance of $Q^2/12$.

In the case of a sine wave with an amplitude of E_{MAX} to utilise the full dynamic range of the ADC, it will have an RMS value equal to $E_{MAX}/\sqrt{2}$, and then the signal to quantisation noise ratio will be

$$\mathrm{SNR} = \left(\frac{E_{\max}}{\sqrt{2}}\right)^2 \frac{12}{Q^2} \,. \tag{F.8}$$

For an ADC with $Q = E_{MAX}/2^{\mathrm{m-1}}$ where m is the number of bits, it is easy to show that the SNR reduces to

$$\mathrm{SNR}_{\mathrm{dB}} = 10\log_{10}\left(6\times 2^{2m-2}\right), \tag{F.9}$$

which for a 12-bit ADC equates to 74dB. Real ADCs never reach this theoretical value, with faster units performing less well than the slower units. A typical achievable SNR for a 10MHz ADC is about 70dB.

The smallest sine wave that can be digitised by an ADC must have a peak magnitude that exceeds $Q/2$ which implies a signal dynamic range of 2^{m} (or 72dB). However, because thermal noise is present along with the input signal, and an N-point FFT has a coherent-integration gain equal to $10\log_{10}(N)$, signals much smaller than the quantization level can be identified as long as the combined magnitude of the signal + noise exceeds one quantisation level.

The following example is of a sine wave with a peak magnitude of 1.414 and normally distributed noise with variance $\sigma_n^2 = 1$ making the SNR = 1. For a maximum excursion of 3σ for the noise, the total peak-to-peak excursion will never exceed $2\times(1.42 + 3) = 8.83$. So, if the quantisation level is set below this value, then the signal should be visible if enough samples are taken.

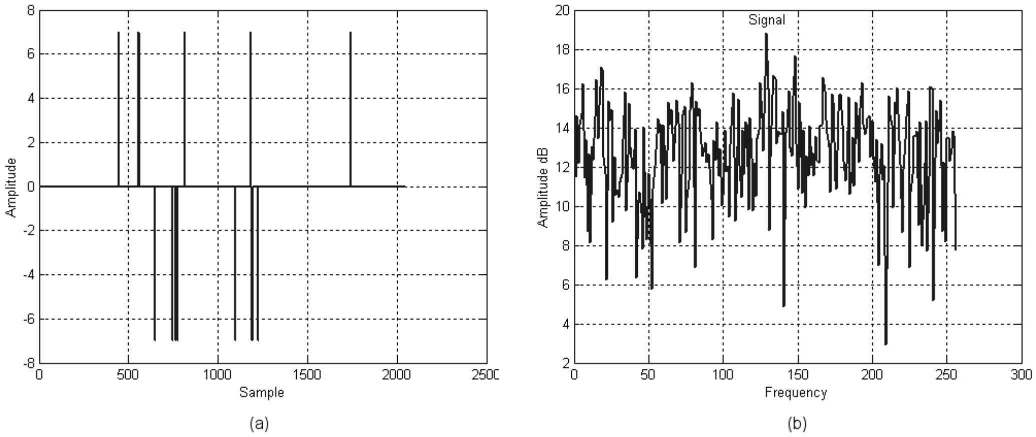

(a) (b)

Figure F.11: The effect of noise and quantisation on the extraction of signals at low SNR is shown here for a quantisation level of 7, a signal magnitude of 1.414 and thermal noise variance of 1.

In Figure F.11 the dominant noise source is the quantisation, with a variance $\sigma_Q^2 = 4$ which is four times higher than that of the thermal noise.

F.5.2. Resolution and the FFT

There is very little point in using an FFT with a resolution that exceeds the range resolution of the radar, but it is often advantageous in imaging applications to use a much wider bandwidth than necessary for the required resolution as this provides some clutter smoothing [67].

A radar is generally specified by its maximum operational range, R_{max}, and the range resolution, δR, that is required. The required chirp bandwidth can be obtained from the equation that relates it and the range resolution

$$\Delta f = \frac{c}{2\delta R}. \tag{F.10}$$

Theoretically, the sample frequency is equal to twice the maximum beat frequency as determined by the Nyquist criterion. However, for realistic anti-aliasing filter characteristics the more usual relationship is

$$f_s = 2.5 f_{b\max}. \tag{F.11}$$

The maximum beat frequency is in turn related to the maximum range and the chirp slope, thus making the sample frequency

$$f_s = \frac{5R_{\max}\Delta f}{T_d c}. \tag{F.12}$$

By specifying T_d at this point, the sample frequency f_s is fixed.

Finally, the bin size is f_s/N where N is the number of range bins output by the FFT, so if a Hamming window is applied, then the resolution will be 1.3 bins and the following holds

$$\delta f_b = \frac{1.3 f_s}{N} = \frac{1}{T_d} . \tag{F.13}$$

Because T_d and f_s have already been determined, then N can be found. $N = 1.3 f_s T_d$ which specifies the radar and the FFT completely. Ideally N=2^{m} and so a compromise is often used to obtain a neat solution.

Appendix G.

IMPATT Oscillator Fundamentals

G.1. Device Physics

Enormous RF power densities can be achieved from the non-self-destructive operation of double-drift silicon IMPATT diodes. The reasons for this are that the diodes typically operate at the maximum electric field-strength possible (dielectric breakdown ≈ 500 kV/cm) and enormous current densities ($>10^5$ A/cm^2) [20].

Double-drift IMPATT diodes are fabricated by first growing an n-type epitaxial layer on an n+ substrate, then either epitaxially growing or ion implanting a p-layer, and finally forming a thin p+ contact layer by means of a diffusion process to form the p+ - p - n - n+ structure shown in Figure G.1 [122].

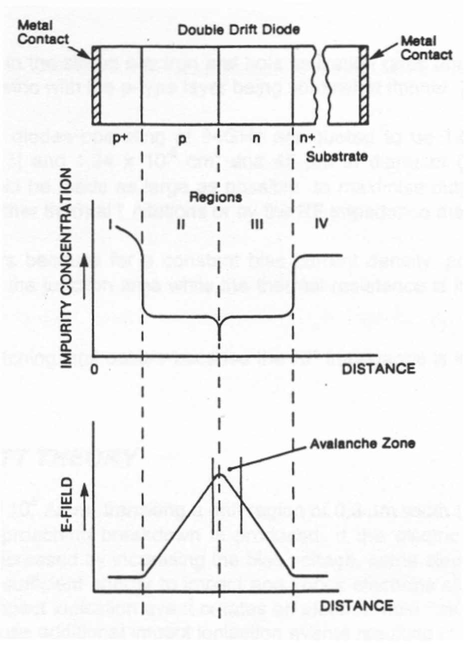

Figure G.1: IMPATT diode internal structure

Junction areas for CW diodes operating at 94GHz are quoted to be 1.06×10^{-5} cm^2 for a 100mW Hughes diode and 1.24×10^{-5} cm^2 and 45 μm in diameter (1.25×10^{-5} cm^2) [87]. Typically the area should be made as large as possible to maximise output power. However, this is constrained by either thermal limitations or by the RF impedance matching limitation.

The thermal limit occurs because, for a constant bias current density, power dissipation in a diode is proportional to the junction area while the thermal resistance is inversely proportional to the junction diameter.

The RF impedance-matching limit occurs because the RF impedance is inversely proportional to the junction area.

G.1.1. Simplified IMPATT Theory

For a current density of 10^5 A/cm^2 transiting a drift region of 0.3 μm width (n, p doped areas), a space change field approaching breakdown is produced. If the electric field of the reverse-biased p-n junction is increased by increasing the bias voltage, some electrons in the region of the peak field will gain sufficient energy to impact-ionise atoms in the crystal lattice. An impact-ionisation event creates an electron-hole pair which is accelerated by the field and can cause additional impact-ionisation events resulting in a large multiplication of current (avalanche breakdown).

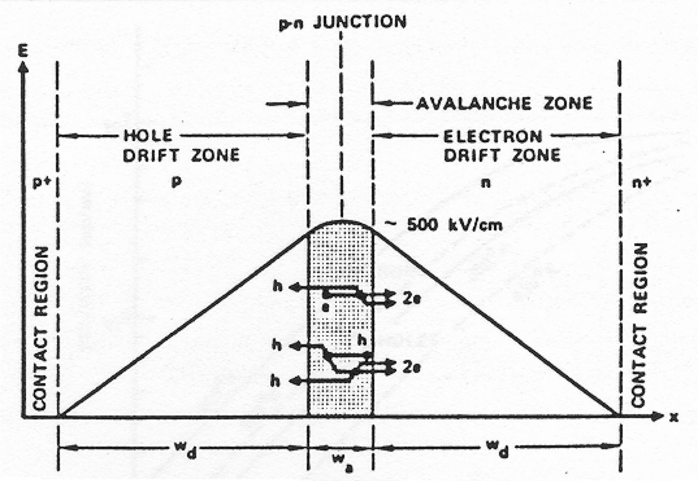

Figure G.2: Electric field profile in an avalanching double-drift IMPATT diode

If the doping levels and the p and n layer thicknesses are properly selected, the transit time delay associated with the holes and electrons moving across their respective drift regions (the p and n layers) will be correct and RF energy at the chosen frequency will be generated.

The ionisation process can be defined by an ionisation rate (the number of ionising collisions per unit length of travel of an accelerated carrier).

$$\alpha = a.\exp(-b/E), \tag{G.1}$$

where: α – Ionisation rate,
E – Electric field strength,
a,b – Constants.

It can be seen that the *E* field must be extremely high before α becomes significant. At low field strengths electrons and holes suffer collisions with phonons (and impurities) before gaining enough energy for an ionising collision. Electron and hole velocities tend to saturate with increasing electric field for the same reasons. This effect is shown in Figure G.3.

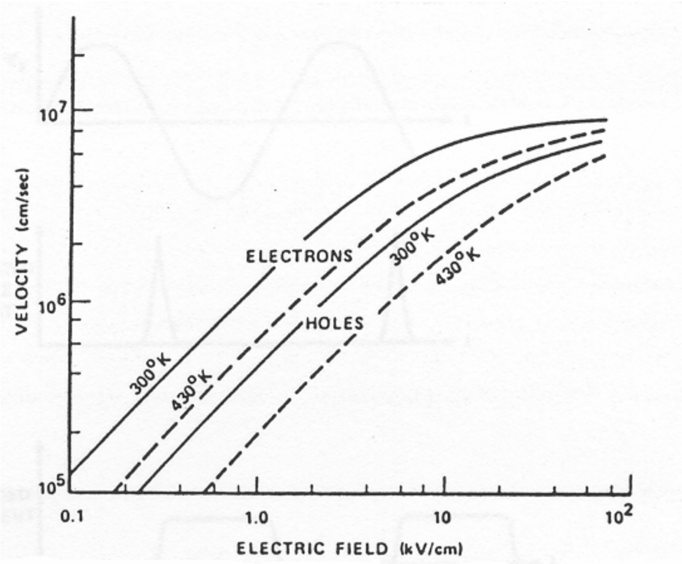

Figure G.3: Drift velocities of electron and holes in silicon

For the field strengths shown above, both holes and electrons will have reached their saturated value of just under 10^7 cm/s.

In simple terms the operation of an IMPATT diode can be explained as follows. An applied AC voltage operating around the breakdown voltage would have the effect of increasing the particle current exponentially while the voltage is positive, peaking at about the zero crossing and then decaying. The electron and hole currents become packets of negative and positive charge which drift across the n and p regions respectively inducing a current as shown in Figure G.4.

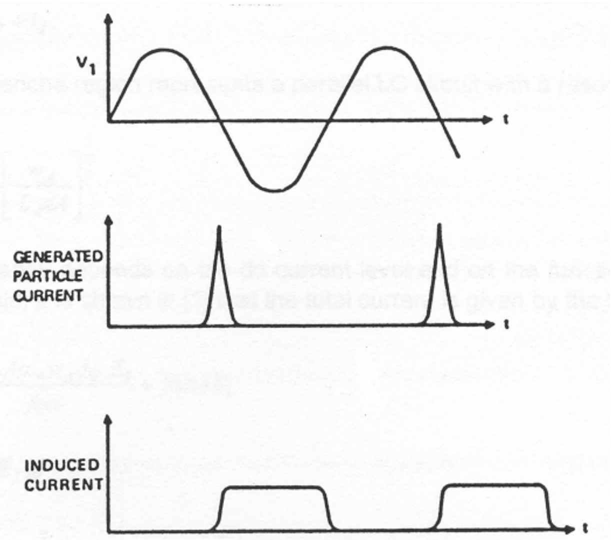

Figure G.4: Waveform for an IMPATT diode

For an excitation frequency $V_I = E\varpi_A$ the induced current is shown for a transit angle $\omega\varpi_d/\upsilon_s = \pi$ (Actually for optimum performance the transit angle should be 0.74π).

Note that the induced current due to electron and hole drift is nearly a square wave which is 180° out of phase with the applied AC voltage, which amounts to an AC negative resistance.

A small pulse of charge δQ is generated at $x = 0$, which causes a drop in the field $\delta E = (4\pi/k)\ \delta Q$. If the field at the edges is to remain constant as the charge moves across the drift region, the voltage will drop at the rate $\upsilon_s\delta E = (4\pi/k)\upsilon_s\delta Q$. Therefore, if the voltage is forced to remain constant, a current δI_e must flow in the external circuit and increase the voltage by adding charges to the edge of the drift region. Rate of voltage increase is $\delta I_e/C$ which should be equal to $\upsilon_s\delta E$ so $\delta I_e = \upsilon_s\delta Q/\varpi_d$.

From the small-signal theory, a typical diode will have an admittance function as shown in Figure G.5 below.

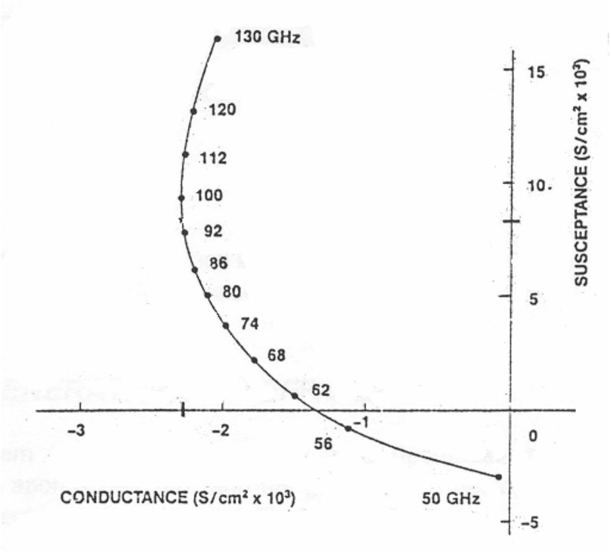

Figure G.5: Small signal admittance of a Double Drift Si IMPATT diode

G.1.2. Diode Packaging

The usefulness of an RF diode depends not only on the processes which generate millimetre-wave energy but also to a large degree on the techniques for packaging the chip.

Reliability is often determined by packaging since bond integrity, exclusion of contaminants and heat removal play an important part in achieving long operating lifetimes.

Because the skin effect is important at millimetre wavelengths, the diode chips are mechanically thinned to a total thickness of 10 to 20μm. Chip diameters at 94GHz are typically 50μm. It is also desirable to minimise the fringing capacitance C_f that shunts the chip in order to reduce circulating RF currents that are dissipated in the resistive parasitics (R_S) [11].

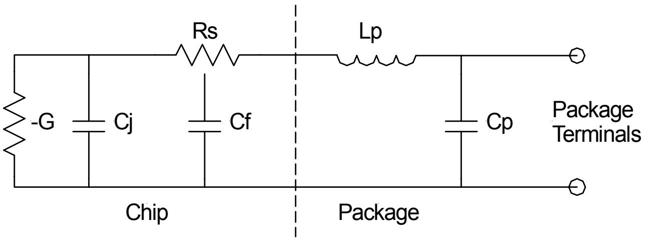

Figure G.6: Equivalent Circuit of Packaged Diode

L_p, the inductance in the connecting lead, often has an optimum non-minimum value for use in a particular application at a particular frequency.

The package shunt-capacitance should be a small fraction of the operating diode capacitance. This is achieved through use of the now ubiquitous quartz ring method shown in Figure G.7.

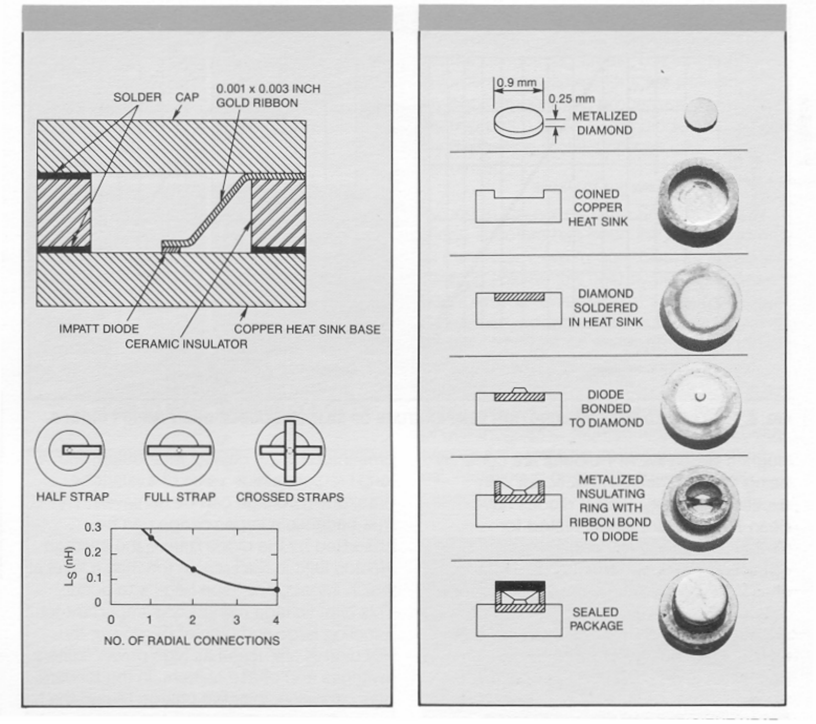

Figure G.7: Diode package design using diamond heat sinks for efficient heat removal and multiple strapping to adjust the series inductance.

Typical values of the package parasitics as listed by the device supplier are:

$L_p = 0.05$ nH
$C_p = 0.13$ pF

This is compared to a total capacitance at V = 0 of between 0.7 and 2.5 pF (75 - 110 GHz) for CW diodes. Pulsed diodes have higher capacitances as they have larger cross-sectional areas.

G.1.3. Thermal Effects

For reliable operation, the junction temperature of a Si IMPATT diode must be kept below 250°C.

Pulsed IMPATTs can produce well over 10 times more power for short pulses (<100ns) than CW devices. This is because the peak temperature reached with moderate duty factors (<0.5%) is more than an order of magnitude below the temperature reached for steady state operation.

Typical results for a 94GHz DDR for diamond and copper heat sinks are presented in Figure G.8.

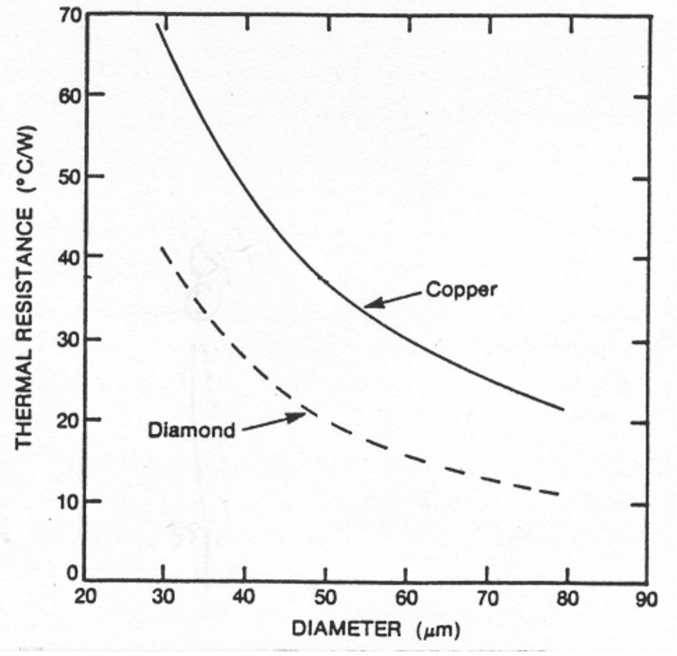

Figure G.8: Copper and diamond thermal resistance as a function of diode diameter.

For a 300 mW CW IMPATT Diode operating at a breakdown voltage of 14.5V at an operating current of 0.7A, the thermal power generated is about 10W. If the diode diameter is 50μm (typical) then the temperature difference between the junction and the heat sink is 370°C for Cu and 200°C for diamond. As the heat sink is maintained at a constant 50°C by massive heat sinking, the junction temperature would be 420°C for Cu and 250°C for diamond. These calculations indicate that such high power CW IMPATT diodes must use diamond heat sinks.

Newer IMPATT Diodes operate with improved efficiency and require a more moderate 400mA to produce 300mW output power. In this case copper heat-sinks are adequate to retain a reasonable junction temperature.

G.2. Oscillator Description

A millimetre-wave oscillator consists of an active device in a resonant cavity as shown in Figure G.9.

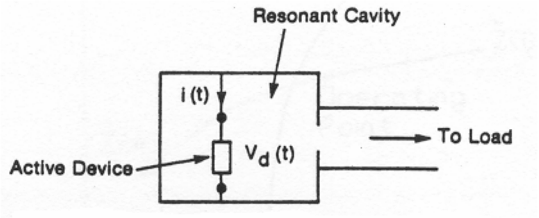

Figure G.9: Typical oscillator configuration comprising an active device mounted within a resonant cavity and iris-coupled to a load

If the harmonic components are neglected the current in the device can be defined as

$$i(t) = A\cos(\omega t + \phi)\,. \tag{G.2}$$

Assuming that the device differential impedance is complex[3],

$$Z^*(A) = -R(A) + jX(A)\,. \tag{G.3}$$

The voltage across the device can be expressed as the real component of the product of the impedance and the current

$$V_d = \mathrm{Re}\left|Z^*(A)A_e \exp(j(\omega t + \phi))\right|. \tag{G.4}$$

If $Z(\omega) = R + jX(\omega)$ is the impedance of the circuit then the voltage V_c across it is

$$V_c(t) = \mathrm{Re}\left|Z(\omega)A_e \exp(j(\omega t + \phi))\right|. \tag{G.5}$$

A free-running oscillator must satisfy

$$V_c(t) + V_d(t) = 0\,. \tag{G.6}$$

Combining the above equations gives

$$\left[Z(\omega) - Z^*(A)\right]A_e \exp(j(\omega t + \phi)) = 0\,. \tag{G.7}$$

For this to be true $Z(\omega) = Z(A)$. Hence the operating point of the oscillator is fixed at the intersection of the locus of the current impedance and the negative of the device impedance as illustrated in Figure G.10.

---

[3] $Z^*(A)$ is the complex conjugate of $Z(A)$

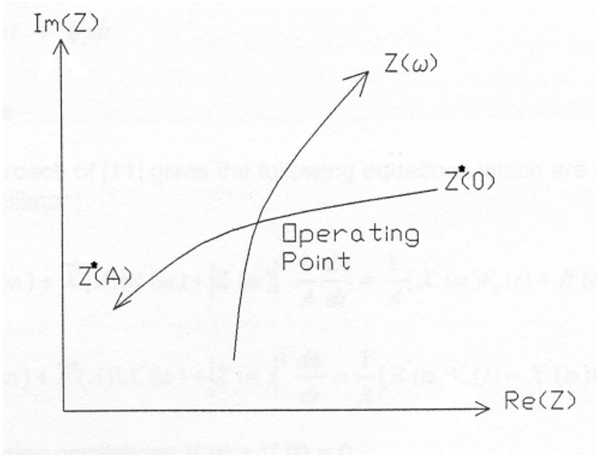

Figure G.10: Complex plane plot of impedance $Z(\omega)$ and $Z^*(A)$ showing the operating point of the oscillator at the intersection of the two loci

G.3. Injection Locking

To perform the injection locking function, a small signal $V(t)$ is injected into the oscillator cavity at a frequency ω_i close to the frequency of the free-running oscillator, the oscillation frequency is synchronised to the frequency of the injected signal

$$V(t) = |V| \cos \omega_i t \,. \tag{G.8}$$

Assuming that the oscillator is locked, then both A and ϕ are locked and the oscillator equations reduce to

$$R(\omega_i) - R^*(A) = \frac{1}{A}|V| \cos \phi \,, \tag{G.9}$$

$$-X(\omega_i) - X^*(A) = \frac{1}{A}|V| \sin \phi \,. \tag{G.10}$$

For $|V|$ small, A stays close to A_0 and the equations reduce to

$$Z(\omega_i) - Z^*(A) = \left|\frac{V}{A_0}\right| \exp(-j\phi) \,, \tag{G.11}$$

where ϕ is the phase of the device current with respect to the injection signal. To satisfy this equation, the vector drawn from the operating point on the device line $Z(A)$ to the ω_I point on the impedance line should have an amplitude $|V|/A_0$ and an angle ϕ.

For ϕ, the phase angle of $Z(\omega)$, and θ, the phase angle of $Z^*(A)$, injection locking will occur over the range ω_1 to ω_2 where ϕ moves from $-90° + \theta$ to $+ 90° + \theta$.

From the diagram in Figure G.11, it can be seen that as ω_i is varied within the locking range ω_1 to ω_2 the operating point moves from the intersection 0 out to A' and then back to 0.

If ω_i is taken outside the limits ω_1 and ω_2 it can be seen that the injected vector amplitude $|V|/A_0$ would have to be increased.

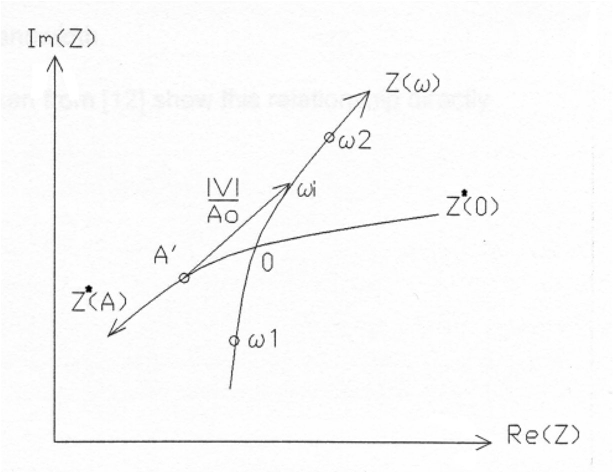

Figure G.11: Effect of a locking vector on the oscillator operating point

G.3.1. Implementation

The method that is commonly used to inject a locking signal into the cavity of an IMPATT oscillator is by means of a non-reciprocal ferrite circulator discussed in Section C.3. Circulators, as the name implies, are 3-port devices in which RF power can circulate from port to port in one direction only as shown in Figure G.12.

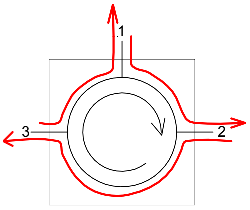

Figure G.12: Direction of power flow through a circulator

This can be used to isolate the input of the oscillator from its output as shown in Figure G.13.

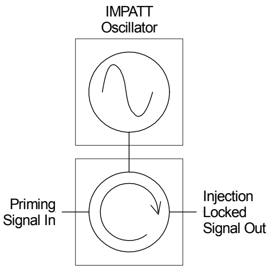

Figure G.13: Injection locking configuration

For the Millitech PILO used in the FMICW radar, the measured output power as a function of injected power and of pulse current is shown in Figure G.14. It can be seen that if the input power is below -5dBm then the PILO free-runs and the output power remains constant. As the input power increases beyond this value up to 12dBm, the output power increases linearly from about 24dBm to 24.9dBm.

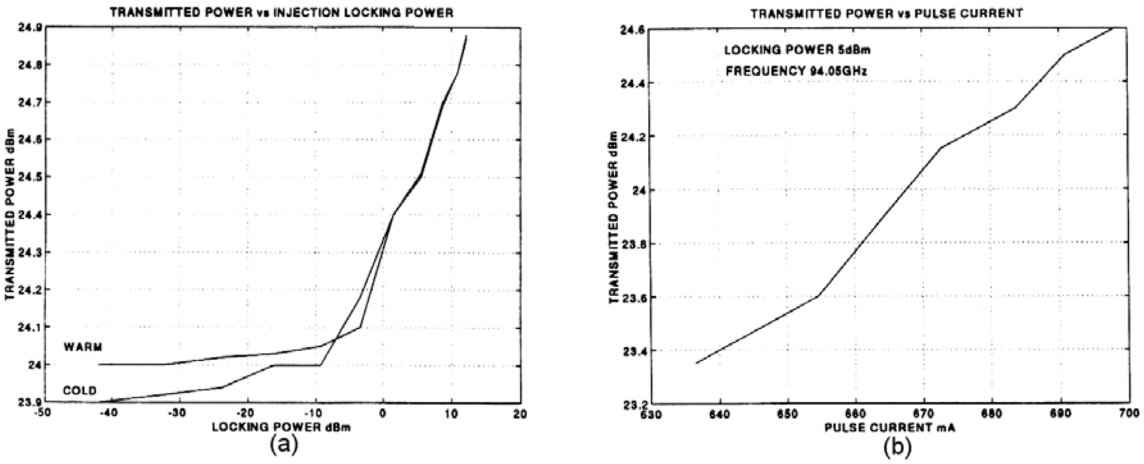

Figure G.14: Measured PILO characteristics including (a) the transmitted power as a function of the injected power and (b) the transmitted power as a function of the peak pulse-current

G.4. Spectral Splitting

The Millitech PILO exhibited some bizarre behaviour as a constant frequency input signal amplitude was increased: the spectrum broadened and then split into two distinct peaks as shown in Figure G.15.

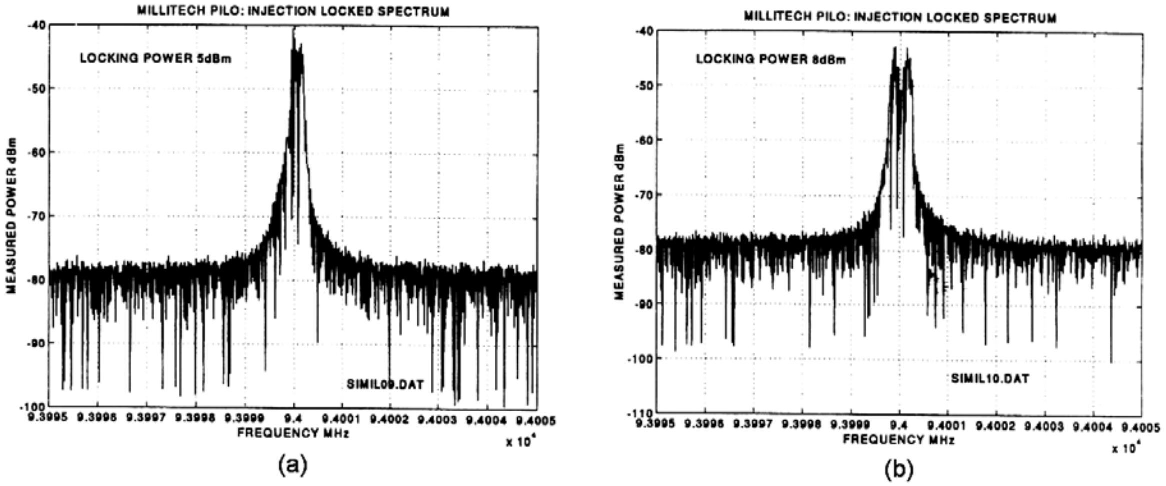

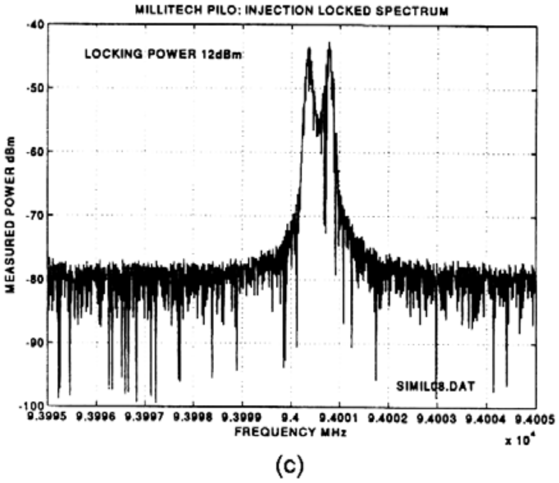

Figure G.15: PILO output spectra showing the relationship between input power and the magnitude of the spectral split for the Millitech PILO

The mechanisms that generate this splitting are not well understood as it produced this splitting even though the input signal was clean and the detected output power showed no signs of AM. Additionally, the phenomenon did not occur in the PILO built by AMS (Figure G.16).

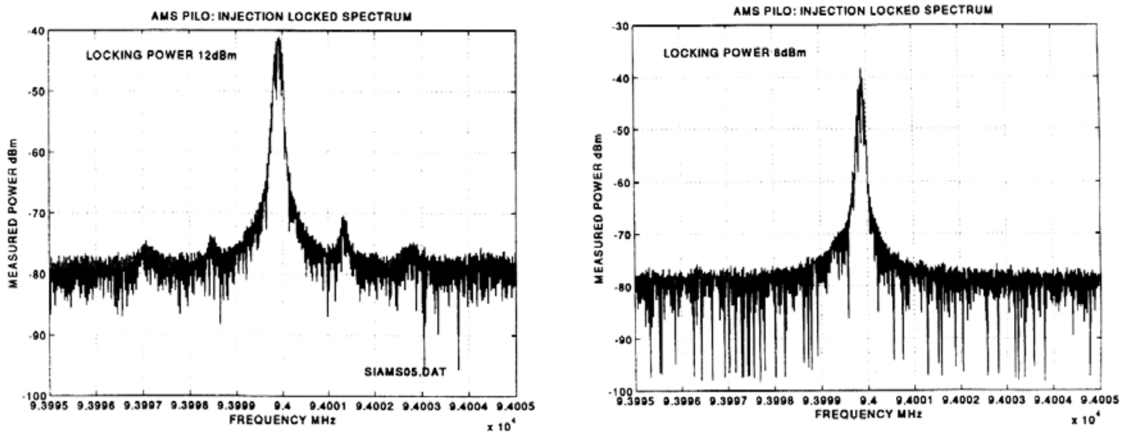

Figure G.16: PILO output spectra with different injected powers for the AMS PILO show no indication of spectral splitting

The effect of this splitting depends on the frequency difference between the two peaks. Remembering that it is only the transmitted signal that is split, the homodyne process will produce a pair of targets. If the difference is sufficiently small then the target peaks will fall within the receiver band, but at the incorrect range. However, as the frequency difference increases, the pair will be shifted out of band.

Bibliography

[1] "3mm Pulse Radar for Collision Avoidance," http://lreri.tripod.com/products.html, accessed 11/05/03

[2] "Analog Devices," http://www.analog.com/uploaded files/Data_Sheets/643619520AD9221_23_20_e.pdf, accessed 29/08/03

[3] "Brimstone Anti Armour Missile: United Kingdom," http://www.army-technology.com/projects/brimstone/, accessed 07/12/04

[4] "Cassini-Huygens Mission to Saturn," http://www.nasa.gov/mission_pages/cassini/main/index.html, accessed 26/11/04

[5] "Directory of US Military Rockets and Missiles," http://www.designation-systems.net/dusrm/m-109.html, accessed 26/11/04

[6] "Geolas Consulting," http://www.geolas.com/Pages/Hwy.html, accessed 30/03/2001

[7] "Magellan Mission to Venus," http://www2.jpl.nasa.gov/magellan/, accessed 26/11/04

[8] "Millimeter Wave Scanning Radar Sensor," http://radio.rphf.spbstu.ru/a263/mars.htm, accessed 16/02/2001

[9] "Thales MESL SAW," http://www.thales-mesl.com/products/sawpcsum.htm, accessed 29/08/03

[10] "X-band Synthetic Aperture Imagery, Sandia Labs," http://www.sandia.gov/RADAR/imageryx.html, accessed 26/11/04

[11] "Hughes Millimeter-Wave Products," Microwave Products Division, Hughes Aircraft Company, Torrance, California,1990.

[12] M. Alhaider and A. Ali, "Experimental studies on millimeter wave and infrared propagation in arid land: the effect of sand storms," in Sixth International Conference on Antennas and Propagation, Coventry, UK, pp.268 - 270, 1989.

[13] M. Ali and M. Alhaider, "Millimeter Wave Propagation in Arid Land- A Field Study in Riyadh," *IEEE Transactions on Antennas and Propagation*, vol. 40, pp. 492-498, 1992.

[14] D. Allerton and A. Clare, "Real-Time Modelling of a Radar Sensor for Enhanced Vision," in SPIE Aerosense, , Proc. SPIE Vol. 5081, Enhanced and Synthetic Vision, Orlando, Florida USA, pp.39-50, 2003.

[15] T. Bailey, "Mobile Robot Localisation and Mapping in Extensive Outdoor Environments," Ph.D thesis, University of Sydney, Australian Centre for Field Robotics, 2002.

[16] A. Baraldi and F. Parmiggiani, "Segmentation of SAR Images by Means of Gabor Filters Working at Different Spatial Resolution," in International Geoscience and Remote Sensing Symposium: Remote Sensing for a Sustainable Future, Lincoln, NE USA, pp.709-713, 1996.

[17] D. Barton, *Modern Radar Systems Analysis*: Artech House, 1988.

[18] R. Baum, "A Novel Algorithm for Resolution of Point Targets," *IEEE Transactions on Antennas and Electronic Systems*, vol. AES-22, pp. 1260-1268, 1986.

[19] P. B. Beasley, A. G. Stove, B. J. Reits, and B. As, "Solving the problems of Single Antenna Frequency Modulated CW Radar," in IEEE International Radar Conference, Arlington, VA USA, pp.391-395, 1990.

[20] P. Bhartia and I. Bahl, *Millimeter Wave Engineering and Applications*: John Wiley & Sons, 1984.

[21] P. Binns, "AMS 94GHz FMCW Radar Project File," Philips Microwave PMHG.010.001, June 1991.

[22] S. Boemhke, J. Bares, E. Mutschler, and N. Keith-Lay, "A High Speed 3D Radar Scanner for Automation," in IEEE International Conference on Robotics and Automation, Leuven, Belgium, pp.2777-2782, 1998.

[23] P. Bolger, "Detecting the Presence of Target Multiplicity," *IEEE Transactions on Antennas and Electronic Systems*, vol. AES-22, pp. 197-203, 1986.

[24] R. Boothe, "The Weibull Distribution Applied to Ground Clutter Backscatter Coefficient," US Army Missile Command, Huntsville, Al. RE-TR-69-15, June 1969.

[25] D. Borghys, V. Lacroix, and C. Perneel, "Edge and Line Detection in Polarimetric SAR Images," in 16th International Conference on Pattern Recognition, Brussels, Belgium, pp.921-924, 2002.

[26] R. Bracewell, *The Fourier Transform and its Applications*, 3rd ed: Mc Graw Hill, 2000.

[27] M. Brady, S. Cameron, H. Durrant-Whyte, M. Fleck, D. Forsyth, A. Noble, and I. Page, "Progress Towards a System that can Acquire Pallets and Clean Warehouses," in Fourth International Symposium on Robotics Research, pp.359-374, 1987.

[28] A. Britton and D. Joynson, "An all weather millimetre wave imaging radar for UAVs," *The Aeronautical Journal*, vol. November, pp. 609-612, 2001.

[29] D. Bromaghim and J. Perry, "A Wideband Linear FM Ramp Generator for the Long-Range Imaging Radar," *IEEE Transactions on Microwave Theory and Techniques*, vol. MTT-26, pp. 322-325, 1978.

[30] G. Brooker, "Integrated FMCW/ICW Front-End Performance," AMS 5840-mmW-0000-TPM, June 1995.

[31] G. Brooker, "Edge Track Mode Feasibility Study," AMS 5840-mmW-C160-SRP, December 1997.

[32] G. Brooker, "Examination of the Re-Built mmWave Front-End Noise Figure," AMS 97-S065, April 1997.

[33] G. Brooker, "Front-End Test Results," AMS 5840-mmW-000-TPR, December 1997.

[34] G. Brooker, "PILO Modulator Test Results," AMS 5840-mmW-1900-TPR, August 1997.

[35] G. Brooker, "Overview of Flight Tests Conducted to Evaluate the Performance of a mmWave Seeker," AMS June 1998.

[36] G. Brooker, "Procedure for the Installation of the mmWave Radar into an Oryx Helicopter," AMS January 1998.

[37] G. Brooker, "Autonomous Aircraft Navigation Using a Millimetre Wave Imaging Radar," in 4th Asian Conference on Robotics and its Applications, Singapore, pp.39-44, 2001.

[38] G. Brooker, "A Robust mmWave Radar Sensor for Underground Applications," in 7th International Conference on Control, Automation, Robotics and Vision, Singapore, pp.1-6, 2002.

[39] G. Brooker, "A W-Band Interrupted FMCW Imaging Radar," in SPIE Aerosense, , Proc. SPIE Vol. 5081, Enhanced and Synthetic Vision, Orlando, Florida USA, pp.11-22, 2003.

[40] G. Brooker, D. Birch, and J. Solms, "A W-Band Airborne Interrupted Frequency Modulated Continuous Wave Radar," *IEEE Transactions on Aerospace and Electronic Systems*, vol. to be published.

[41] G. Brooker and T. Carter, "A Millimetre Wave Radar Sensor for Autonomous Navigation and Landing," in Australian Conference on Robotics and Automation, Melbourne, Australia, pp.59-64, 2000.

[42] G. Brooker, S. Scheding, M. Bishop, and R. Hennessy, "Development and Application of Millimetre wave Radar Sensors for Underground Mining," *IEEE Sensors Journal*, vol. to be published.

[43] G. Brooker and S. Youds, "Using Millimetre Wave Radar to Monitor In-Stope Backfilling at Olympic Dam Mine, South Australia," in CMMI Conference 2002, International Codes, Technology and Sustainability for the Minerals Industry, Cairns, Australia, 2002.

[44] E. Brookner, *Radar Technology*: Artech House, 1982.

[45] R. Buderi, *The Invention that Changed the World - The Story of Radar from War to Peace*: Abacus, 1998.

[46] L. Bui, Y. Alon, and D. Nielson, "Extended Range Coverage of an Imaging Radar System with Feed-Mounted 94GHz MIMIC HEMT Low Noise Amplifier and External ILO," in IEEE MTT-S Digest, Albuquerque, NM USA, pp.687-690, 1992.

[47] L. Bui, D. Uecker, E. loose, and Y. Alon, "Test results of an experimental autonomous aircraft landing system utilizing a 94 GHz FM-CW imaging radar," in Microwave Symposium Digest, Atlanta, GA USA, pp.857-860, 1993.

[48] M. Burgess and R. Hayes, "Synthetic Vision - A View in the Fog," *IEEE Aerospace and Electronic Systems Magazine*, vol. March, pp. 6-13, 1993.

[49] R. Buse and Z. Liu, "Feature Measurement and Analysis Using Gabor Filters," in International Conference on Acoustics, Speech and Signal Processing, Detroit MI, USA, pp.2447-2450, 1995.

[50] J. Cadwallader and D. English, "Millimeter Front End Provides Frequency Agility," in *MSN*, vol. December, pp. 41-51, 1980.

[51] W. Camp, "ALCOR, a wide-bandwidth range measurement radar," in Thirteenth Annual Tri-Service Radar Symposium, pp.520-551, 1967.

[52] B. Campbell, "High-resolution Radar Coherent Linear FM Microwave Source," *IEEE Transactions on Aerospace and Electronic Systems*, vol. AES-6, pp. 62-72, 1970.

[53] J. Canny, "A Computational Approach to Edge Detection," *IEEE Transactions on Pattern Analysis and Machine Intelligence*, vol. 8, pp. 679-698, 1986.

[54] W. Caputi-Jr, "Stabilised Linear FM Generator," *IEEE Transactions on Aerospace and Electronic Systems*, vol. AES-9, pp. 670-678, 1973.

[55] A. Celliers, "The Design of a 94GHz High Resolution Coherent Radar," Ph.D thesis, University of Cape Town, 1987.

[56] K. Chong and L. Kleeman, "Feature-Based Mapping in real, Large Scale Environments using an Ultrasonic Array," *International Journal Robotics Research*, vol. 18, pp. 3-19, 1999.

[57] S. Clark, "Autonomous Land Vehicle Navigation Using Millimetre Wave Radar," Ph.D thesis, University of Sydney, 1999.

[58] S. Clark and G. Dissanayake, "Simultaneous Localisation and Map Building Using Millimetre Wave Radar to Extract natural Features," in IEEE International Conference on Robotics and Automation, Detroit MI, USA, pp.1316-1321, 1999.

[59] S. Clark and H. F. Durrant-Whyte, "The Design of a High Performance MMW Radar System for Autonomous Land Vehicle Navigation," in International Conference on Field and Service Robotics, Australia, pp.292-299, 1997.

[60] S. Clark and H. F. Durrant-Whyte, "Autonomous Land Vehicle Navigation Using Millimeter Wave Radar," in IEEE International Conference on Robotics and Automation, Leuven Belgium, pp.3697-3702, 1998.

[61] G. Comparetto, "The Impact of Dust and Foliage penetration on Signal Attenuation in the Millimeter Wave Regime," *Journal of Space Communication*, vol. 11, pp. 13-20, 1993.

[62] C. Connolly and R. Grupen, "On the Applications of Harmonic Functions to Robotics," *Journal of Robotic Systems*, vol. 10, pp. 931-946, 1993.

[63] N. Corron and J. Brooks, "Resolving Closely Spaced Targets Using Linear FM Envelope Processing," in IEEE International Radar Conference, Alexandria, VA USA, pp.62-66, 1995.

[64] C. Covault, "New French Missiles Expand Attack Options," in *Aviation Week & Space Technology*, Jaunary 1995, pp. 44-45.

[65] N. Currie, *Techniques of Radar Reflectivity Measurement*: Artech House, 1984.

[66] N. Currie, *Radar Reflectivity Measurement: Techniques and Applications*: Artech House, 1989.

[67] N. Currie and C. Brown, *Principles and Applications of Millimeter-Wave Radar*: Artech House, 1987.

[68] N. Currie, R. Hayes, and R. Trebits, *Millimeter-Wave Radar Clutter*: Artech House, 1992.

[69] W. Deats, D. Farina, and J. Bull, "Super-Resolution Signal Processing Aids RCS Testing," in *Microwaves & RF*, vol. March, 1991, pp. 74-82.

[70] J. Detlefsen, "Imaging Applications of Millimeter Wave sensors in Robotics and Road Traffic," in IEEE Microwave Systems Conference, Orlando, FA USA, pp.115-124, 1995.

[71] Y. M. deVillers, "A Coherent Ka Band FMCW Radar for Real Time Target Acquisition," in IEEE National Radar Conference, Lynnfield, MA USA, pp.1-5, 1993.

[72] G. Dissanayake, H. Durrant-Whyte, and T. Bailey, "A Computationally Efficient Solution to the Simultaneous Localisation and Planning (SLAM) Problem," in IEEE International Conference on Robotics and Automation, pp.1009-1014, 2000.

[73] T. Duffield, C. Smith, P. Pusateri, D. English, and F. Bernues, "Millimeter Solid-State Pulsed Coherent Radar," in IEEE-MTTS International Microwave Symposium, 1979 (late paper).

[74] A. Dunkin, "Automated Guided vehicle Systems: An Introduction," in *Industrial Engineering*, vol. 26, 1994, pp. 47-53.

[75] D. Dunn and W. Higgins, "Optimal Gabor Filters for Texture Segmentation," *IEEE Transactions on Image Processing*, vol. 4, pp. 947-964, 1995.

[76] M. duPlessis, "Measured Performance Report for the 94GHz Cosec Squared Antenna," Avitronics 210701-00000R24, July 1995.

[77] H. Durrant-Whyte, "An Autonomous Guided Vehicle for Cargo Handling Applications," *International Journal Robotics Research*, vol. 15(5), pp. 407-440, 1996.

[78] H. Durrant-Whyte, E. Bell, and P. Avery, "The design of a radar-based navigation system for large outdoor vehicles," in IEEE International Conference on Robotics and Automation, Nagoya Japan, pp.764-769, 1995.

[79] A. Elfes, "Using Occupancy Grids for Mobile Robot Perception and Navigation," in *Computer Magazine*, vol. June, 1989, pp. 46-47.

[80] L. Eriksson and S. Broden, "High Performance Automotive Radar," in *Microwave Journal*, vol. October, pp. 24-38, 1996.

[81] L. H. Eriksson and B. As, "Automotive Radar for Adaptive Cruise Control and Collision Warning/Avoidance," in IEE International Conference on Radar, Edinburgh, UK, pp.16-20, 1997.

[82] T. Ersson and X. Hu, "Path Planning and Navigation of Mobile Robots in Unknown Environments," in IEEE/RSJ International Conference on Intelligent Robots and Systems, Maui, Hawaii, pp.858-864, 2001.

[83] D. Ferguson and J. Radke, "Synthetic Vision/Enhanced Vision System Implementation," in Telesystems Conference, 1993. 'Commercial Applications and Dual-Use Technology', Atlanta, GA USA, pp.91-95, 1993.

[84] M. Ferri, G. Galati, and M. Naldi, "A Novel W-Band Radar for Aircraft Traffic Monitoring Implementation, First Operational Results, Perspectives," in MSMW, Kharkov, Ukraine, pp.27-32, 2001.

[85] A. Foessel, "Radar Sensor Model for Three-Dimensional Map Building," in Mobile Robots XV and Telemanipulator and Telepresence Technologies VII, 2000.

[86] A. Foessel, "Scene Modelling from Motion-Free Radar Sensing," Ph.D thesis, Carnegie Mellon University, 2002.

[87] T. T. Fong and H. J. Kuno, "Millimeter-Wave Pulsed IMPATT Sources," *IEEE Transactions on Microwave Theory and Techniques*, vol. MTT-27, pp492-499, 1979.

[88] D. Fox, S. Thrun, W. Burgard, and F. Dellaert, "Particle Filters for Mobile Robot Localization," in *Sequential Monte Carlo methods in Practise*, A. Doucet, N. deFreitas, and N. Gordon, Eds., 2000.

[89] F. Gardner, *Phaselock Techniques*, 2nd ed: John Wiley & Sons, 1979.

[90] S. Ghobrial and S. Sharief, "Microwave Attenuation and Cross Polarization in Dust Storms," *IEEE Transactions on Antennas and Propagation*, vol. AP-35, pp. 418-425, 1987.

[91] G. Goebel, "Modern Western Cruise Missiles," http://www.vectorsite.net /twcruz.html, accessed 07/12/04

[92] B. Gold and C. Radar, *Digital Processing of Signals*: McGraw-Hill, 1969.

[93] J. Goldhirsh, "Attenuation and Backscatter From a Derived Two-Dimensional Duststorm Model," *IEEE Transactions on Antennas and Propagation*, vol. 49, pp. 1703-1711, 2001.

[94] G. Gray, "Radar Imaging with ALG- the On-Board Low Visibility Landing Aid," *IEE Aviation Surveillance Systems*, vol. 10, pp. 10/11-10/14, 2002.

[95] I. Gresham, N. Jain, T. Budka, A. Alexanian, N. Kinayman, B. Zeigler, S. Brown, and P. Staecker, "A 76-77GHz Pulsed-Doppler Radar Module for Autonomous Cruise Control Applications," in IEEE International Microwave Symposium, pp.1551-1554, 2000.

[96] J. Guivant and E. Nebot, "Optimisation of the Simultaneous Localisation and Map Building Algorithm for Real Time Implementation," *IEEE Transactions on Robotics and Automation*, vol. 17, pp. 242-257, 2001.

[97] S. Halversen, "Calculating the Orientation of a Rectangular Target in SAR Imagery," in IEEE National Aerospace and Electronics Conference, Dayton OH, USA, pp.260-264, 1992.

[98] F. Henderson and J. Lewis, "Principles and Applications of Imaging Radar," in *Manual of Remote Sensing*, vol. 2, 3 ed: John Wiley & Sons, 1998.

[99] L. Hoffman, K. Hurlburt, D. Kind, and H. Wintroub, "A 94GHz Radar for Space Object Identification," *IEEE Transactions on Microwave Theory and Techniques*, vol. MTT-17, pp. 1145-1149, 1969.

[100] L. H. Holloway, "Transient Temperature Behaviour in Pulsed Double-Drift IMPATT Diodes," *IEEE Transactions on Electron Devices*, vol. ED-27, pp. 433-442, 1980.

[101] S. Honma and N. Uehara, "Millimeter-Wave Radar Technology for Automotive Applications,". http://global.mitsubishielectric.com/bu/automotive/advanced_technology/pdf/vol94_tr5.pdf, accessed 10/04/05.

[102] W. Horne and B. Hudson, "Evaluation of Candidate Millimeter Wave Radars for Synthetic Vision," in Telesystems Conference, 1993. 'Commercial Applications and Dual-Use Technology', Atlanta, Georgia, USA, pp.83-89, 1993.

[103] W. Irving, L. Novak, and A. Willsky, "A Multiresolution Approach to Discrimination in SAR Imagery," *IEEE Transactions On Aerospace and Electronic Systems*, vol. 33, pp. 1157-1169, 1997.

[104] A. Jain, *Fundementals of Digital Image Processing*: Prentice Hall, 1989.

[105] R. Johnson, *Designer Notes for Microwave Antennas*: Artech House, 1991.

[106] R. Johnson, *Antenna Engineering Handbook*, 2 ed: McGraw Hill, 1993.

[107] K. Kaliyaperumal, S. Lakshmanan, and K. Kluge, "An Algorithm for Detecting Roads and Obstacles in Radar Images," *IEEE Transactions on Vehicular Technology*, vol. 50, pp. 170-179, 2001.

[108] N. Kees, E. Schmidhammer, and J. Detlefsen, "Improvement of Angular Resolution of a Millimeterwave Imaging System by Transmitter Location Multiplexing," in IEEE Microwave Systems Conference, Orlando, FL USA, pp.105-108, 1995.

[109] S. Kesler, *Modern Spectrum Analysis, II*: IEEE Press, 1986.

[110] R. Khan and D. Mitchell, "Waveform Analysis for High-Frequency FMICW Radar," *IEE Proceedings on Radar and Signal Processing*, vol. 138, pp. 411-419, 1991.

[111] R. Khan and D. Power, "Doppler Processing for Coherent Chirp Radars," in Canadian Conference on Electrical and Computer Engineering, Halifax, NS Canada, pp.767-770, 1994.

[112] K. Kimoto and C. Thorpe, "Map Building with Radar and Motion Sensors for Automated Highway Vehicle Navigation," in IEEE/RSJ International Conference on Intelligent Robots and Systems, Grenoble, France, pp.1721-1728, 1997.

[113] H. Kirsten, "mmW radar Imaging Resolution Enhancement Options," AMS 91-S433/HADK, September 1991.

[114] D. Klugmann, "A Monostatic Solid State W-Band FM-CW Doppler Profiler," in IEEE International Geoscience and Remote Sensing Symposium, pp.3646-3648, 2002.

[115] E. Knott, J. Shaeffer, and M. Tuley, *Radar Cross Section*: Artech House, 1985.

[116] S. Kobayashi and A. Hatono, "Unwanted Signal Reflection in FMCW Radar for Measuring Slag level in BOF," in International Symposium on Noise and Clutter Rejection in Radars and Image Sensors, pp.240-245, 1984.

[117] K. Koester, L. Kosowsky, and J. Sparacio, "Millimeter Wave Propagation," in *Millimeter Wave Radar*, S. Johnston, Ed.: Artech House, 1980.

[118] K. Koester and W. Vaillancourt, "Talons 95 GHz Radar Sensor for Autonomous Landing Guidance," *IEEE Aerospace and Electronic Systems Magazine*, vol. July, pp. 40-44, 1992.

[119] B. Korn and P. Hecker, "Enhanced and Synthetic Vision: Increasing Pilot's Situation Awareness under Adverse Weather Conditions," in 21st Digital Avionics Systems Conference, pp.C.2-1 - C.2-10, 2002.

[120] G. Krieger, J. Mittermayer, S. Buckreuss, M. Wendler, T. Sutor, F. Witte, and A. Moreira, "Sector Imaging Radar for Enhanced Vision," *Aerospace Science and Technology*, pp. 147-158, 2003.

[121] G. Kulemin, *Millimeter-Wave Radar Targets and Clutter*: Artech House, 2003.

[122] H. J. Kuno, "Solid State Millimeter-Wave Power Sources and Combiners," in *Microwave Journal*, June 1981, pp. 21-34.

[123] S. Lakshmanan, A. Jain, and Y. Zhong, "Detecting Straight Edges in Millimeter-Wave Images," in International Conference on Image Processing, Washington DC, USA, pp.258-261, 1995.

[124] M. Lange and J. Detlefsen, "94 GHz Three Dimensional Imaging Radar Sensor for Autonomous Vehicles," *IEEE Transactions on Microwave Theory and Techniques*, vol. 39, pp. 819-825, 1991.

[125] D. Langer, "An Integrated MMW Radar System for Outdoor Navigation," Ph.D thesis, Carnegie Mellon University, 1997.

[126] J. Leal, S. Scheding, and G. Dissanayake, "Probabalistic 2-D Mapping of Unstructured Environments," in Australian Conference on Robotics and Automation, Melbourne Australia, pp.19-24, 2000.

[127] J. Leonard and H. Durrant-Whyte, "Simultaneous Map Building and Localisation for an Autonomous Mobile Robot," in IEEE International Workshop on Intelligent Robots and Systems, pp.1442-1447, 1991.

[128] N. Levanon, "Stepped-Frequency Pulse-Train Radar Signal," *IEE Proceedings on Radar, Sonar & Navigation*, vol. 149, pp. 297-309, 2002.

[129] B. L. Lewis, F. F. Kretschmer, and W. W. Shelton, *Aspects of Radar Signal Processing*: Artech House, 1986.

[130] T. Liau, A. Carr, and L. Cuthbert, "Using Non-Fourier Techniques in Signal Processing for an FMCW Hidden-Object Detection Radar," *IEE Electronics Letters*, vol. 22, pp. 466-467, 1986.

[131] C. Liebe, "Accuracy Performance of Star Trackers - A Tutorial," *IEEE Transactions on Antennas and Electronic Systems*, vol. AES-38, pp. 587-599, 2002.

[132] L. P. Ligthart, "System Considerations on the FM-CW Delft Atmospheric Research Radar," in IEEE International Radar Conference, pp.38-43, 1980.

[133] M. Long, *Radar Reflectivity of Land and Sea*: Artech House, 1983.

[134] B. Lovell, *Echoes of War - The Story of H_2S Radar*: Adam Hilger, 1991.

[135] S. Maas, *Microwave Mixers*, 2nd ed: Artech House, 1993.

[136] D. Macfarlane and D. Robertson, "A 94GHz dual-mode active/passive imager for remote sensing," in SPIE Passive Millimetre-Wave and Terahertz Imaging and Technology, London, Vol. 5619, pp.1-12, 2004.

[137] S. Majumder, S. Scheding, and H. F. Durrant-Whyte, "Sensor Fusion and Map Building for Underwater Navigation," in Australian Conference on Robotics and Automation, Melbourne Australia, pp.25-30, 2000.

[138] M. Martin and H. Moravec, "Robot Evidence Grids," *CMU Robotics Institute Technical Report*, vol. CMU-RI-TR-96-06, 1996.

[139] R. McGee and J. Loomis, "Radar Tracking of an M-48 Tank at 94 and 140 GHz," in 6th DARPA TriService Millimeter Waves Conference, pp.123-127, 1977.

[140] H. Meinel, "Millimeterwaves for Automotive Applications," in 26th European Microwave Conference, Prague Czech Republic, pp.830-835, 1996.

[141] M. Montemerlo and S. Thrun, "A Multi-Resolution Pyramid for Outdoor Robot Terrain perception," in Proc. AAAI National Conference on Artificial Intelligence, 2004.

[142] L. Moon-Sik and K. Yong-Hoon, "An Efficient Multitarget Tracking Algorithm for Car Applications," *IEEE Transactions on Industrial Electronics*, vol. 50, pp. 397-399, 2003.

[143] R. Moore, "Trade-off Between Picture Element Dimensions and Non-Coherent Averaging in a Side-Looking Airborne Radar," *IEEE Transactions on Antennas and Electronic Systems*, vol. AES-15, pp. 697-708, 1979.

[144] P. Moutarlier and R. Chatila, "Stochastic Multisensory Data Fusion for Mobile Robot Location and Environmental Modelling," in 5th International Symposium of Robotics Research, pp.85-94, 1989.

[145] T. Musch, I. Rolfes, and B. Schiek, "A Highly Linear Frequency Ramp Generator Based on a Fractional Divider Phase-Locked-Loop," *IEEE Transactions on Instrumentation and Measurement*, vol. 48, pp. 634-637, 1999.

[146] K. Namuduri, R. Mehrotra, and N. Ranganathan, "Edge Detection Models Based on Gabor Filters," in Proc. 11th IAPR Conference on Pattern Recognition: Image, Speech and Signal Analysis, The Hague, Netherlands, pp.729-732, 1992.

[147] G. Neininger, "A FM/CW Radar with High Resolution in Range and Doppler Application for Anti-Collision Radar for Vehicles," in IEEE Radar 77, London, pp.526-530, 1977.

[148] S. Nelson, "Measurement and Calculation of Powdered Mixture Permittivities," *IEEE Transactions on Instrumentation and Measurement*, vol. 50, pp. 1066-1070, 2001.

[149] P. Newman, "On the Structure and Solution of the Simultaneous localisation and Map Building Problem," Ph.D thesis, University of Sydney, 1999.

[150] D. Nicholson, "Estimating Target Lengths Shorter than the Radar Pulse Width," *IEEE Transactions on Antennas and Electronic Systems*, vol. AES-11, pp. 534-538, 1975.

[151] M. Nikolova and A. H. III, "Segmentation of a Road from a Vehicle-Mounted Radar and Accuracy of the Estimation," in IEEE Intelligent Vehicles Symposium, Dearborn MI, USA, pp.284-289, 2000.

[152] L. Novak and F. Vote, "Millimeter Airborne Radar Target Detection and Selection Techniques," in IEEE-NAECON, pp.807-817, 1979.

[153] J. Ondria, "Novel Approaches to Wide Electronic Tuning Bandwidth in Solid State Millimeter Sources," in IEEE SPIE Symposium, Arlington, VA USA, pp.seminar 10, 1982.

[154] J. Ondria and A. G. Cardiasmenos, "Desensitisation of Spread Spectrum Radar Systems by Far Off the Carrier Noise Generation in Millimeter Sources," in 2nd Military Microwaves Conference, London, England, pp.292-299, 1980.

[155] J.-P. Philippe, "The APACHE: Forerunner of a Family of Air-to-Surface Missiles," in *Military Technology*, vol. MILTECH 5/92, 1992.

[156] A. Poole, "On the Use of Psuedorandom Codes for "Chirp" Radars," *IEEE Transactions on Antennas and Propagation*, vol. AP-27, pp. 480-485, 1979.

[157] J. Preissner, "The Influence of the Atmosphere on Passive Radiometric Measurements," in AGARD Conference Reprint No. 245: Millimeter and Submillimeter Wave Propagation and Circuits, 1978.

[158] L. Rabiner and B. Gold, *Theory and Application of Digital Signal processing*: Prentice Hall, 1975.

[159] C. Rader, "A Simple Method for Sampling In-Phase and Quadrature Components," *IEEE Transactions on Antennas and Electronic Systems*, vol. AES-20, pp. 821-824, 1984.

[160] U. C. Ray and A. K. Gupta, "Intrapulse Frequency Variation in a W-Band Pulsed IMPATT Diode," in *Microwave Journal*, vol. April, 1994, pp. 238-244.

[161] W. T. Read, "A Proposed High-Frequency Negative-Resistance Diode," *The Bell System Technical Journal*, pp. 401-446, 1958.

[162] L. Reindl, C. Ruppell, S. Berek, U. Knauer, M. Vossiek, P. Heide, and L. Oreans, "Design, Fabrication and Application of Precise SAW Delay Lines Used in an FMCW Radar System," *IEEE Transactions on Microwave Theory and Techniques*, vol. 49, pp. 787-794, 2001.

[163] D. Robertson and D. Macfarlane, "AVTIS: All-weather Volcano Topography Imaging Sensor," in 29th International Conference on Infrared and Millimetre Waves, Karlsruhe, Germany, pp. 813-814, 2004.

[164] H. Rohling, "A 77GHz Automotive Radar System for AICC Applications," in International Conference on Microwaves and Radar, Workshop, Krakow, Poland, 1998.

[165] H. Rohling and R. Mende, "OS CFAR Performance in a 77 GHz Radar Sensor for Car Application," in CIE International Conference on Radar, Beijing, China, pp.109-113, 1996.

[166] M. Russell, C. Drubin, A. Marinilli, W. Woodington, and M. Del Checcolo, "Commercial Radar Technology," in IEEE International Radar Conference, Alexandria, VA USA, pp.819-824, 2000.

[167] F. Sadjadi, M. Helgeson, J. Radke, and G. Steyn, "Radar Synthetic Vision System for Adverse Weather Aircraft landing," *IEEE Transactions on Aerospace and Electronic Systems*, vol. 35, pp. 2-14, 1999.

[168] S. Salous, "Weighted Sequences for HF FMCW Sounding," in IEE HF Radio Systems and Techniques, Nottingham, UK, pp.423-427, 1997.

[169] S. Scheding, G. Brooker, M. Bishop, R. Hennessy, and A. Maclean, "Terrain Imaging Millimetre Wave Radar," in 7th International Conference on Control, Automation, Robotics and Vision, Singapore, pp.13-18, 2002.

[170] H. Schimpf, A. Wahlen, and H. Essen, "High Range Resolution by means of Synthetic Bandwidth Generated by Frequency-Stepped Chirps," *IEE Electronics Letters*, vol. 39, pp. 1346-1348, 2003.

[171] L. Schmidt, R. Jester, and G. Kadisch, "FM-ICW Monopulse Radar Sensor," in Military Microwaves, London, pp.161-166, 1990.

[172] F. Sears, M. Zemansky, and H. Young, *College Physics*, 7th ed: Addison-Wesley, 1991.

[173] S. Sharief, "Backscatter Properties of Dusty Medium at X Band," in 6th International Conference on Antennas and Propagation, pp.424 - 427, 1989.

[174] M. Skolnik, *Radar Handbook*: McGraw Hill, 1970.

[175] M. Skolnik, *Introduction to Radar Systems*, 2nd ed: McGraw-Hill Kogakusha, 1980.

[176] M. Skolnik, *Radar Handbook*, 2nd ed: McGraw Hill, 1990.

[177] R. Smith, M. Self, and P. Cheesman, "A Stochastic Map for Uncertain Spatial Relationships," in Fourth International Symposium on Robotics Research, pp.467-474, 1987.

[178] J. Solms, "Seeker Image Processing: AMS Log Book," 1997.

[179] J. Suomela, J. Kuusela, and A. Halme, "Millimeter Wave Radar for Close Terrain Mapping of an Intelligent Autonomous Vehicle," in 2nd IFAC Conference on Intelligent Autonomous Vehicles, Helsinki Finland, 1995.

[180] H. L. V. Trees, *Estimation and Modulation Theory Part III*: John Wiley & Sons, 1971.

[181] T. Tsumura, "Survey of Automated Guided vehicle in Japanese Factory," in IEEE International Conference on Robotics and Automation, pp.1329-1334, 1986.

[182] S. Tsunoda, F. Pace, J. Stence, and M. Woodring, "Lynx: A High-Resolution Synthetic Aperture Radar," in SPIE Aerosense, Vol. 3704, pp.1-7, 1999.

[183] B. Tullsson, "Topics in FMCW Disturbance Suppression," in Radar-97, Edinburgh, UK, pp.1-5, 1997.

[184] F. Ulaby and M. Dobson, *Handbook of Radar Scattering Statistics for Terrain*: Artech House, 1989.

[185] J. Wilding and R. Zuljan, "Vengeance Weapons," http://www.onwar.com /articles/f0109.htm, accessed 07/12/04

[186] A. Wilkinson, J. Horrell, and M. Inggs, "SASAR VHF Interferometry: Early Results," in 3rd European Conference on Synthetic Aperture Radar, Munich Germany, pp.411-414, 2000.

[187] M. Williams, "Millimetre-Wave Radars: Affordable Sensors for Smart Weapons," in *Military Technology*, vol. MILTECH, 1989, pp. 31-38.

[188] S. Williams, "Efficient Solutions to Autonomous Mapping and Navigation Problems," Ph.D thesis, University of Sydney, Australian Centre for Field Robotics, 2001.

[189] P. M. Woodward, *Probability and Information Theory with Applications to Radar*: Artech House, 1980.

[190] S. Yiyang, Z. Ning, and L. Yongtan, "New Waveform with both High Range Resolution and Long Coherent Integration Time in a HF Radar," in CIE International Conference on Radar, Beijing, China, pp.285-288, 1996.

[191] R. Yoshitani and M. Beebe, "94 GHz Active Missile Seeker Captive Flight Test Results," in 6th DARPA Tri Service Millimeter Waves Conference, pp.129-139, 1977.

[192] J. Zelek and M. Levine, "Local-Global Concurrent Path Planning and Execution," *IEEE Transactions on Systems Man and Cybernetics - Part A: Systems and Humans*, vol. 30, pp. 865-870, 2000.